

PROCESSES OF EFFICIENT VISIBLE LIGHT EMISSION IN SILICON
NANOSTRUCTURES

by

MICHAEL JOHN ESTES

B.S., Electrical Engineering, Ohio State University, 1985

M.S., Electrical Engineering, Air Force Institute of Technology, 1990

A thesis submitted to the
Graduate School of the
University of Colorado in partial fulfillment
of the requirement for the degree of
Doctor of Philosophy
Department of Electrical and Computer Engineering
1995

DISTRIBUTION STATEMENT A

Approved for public release;
Distribution Unlimited

This dissertation for the Doctor of Philosophy degree by

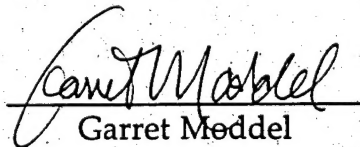
Michael J. Estes

has been approved for the

Department of

Electrical and Computer Engineering

by


Garret Møddel


Kenneth Douglas

Date November 30, 1995

GENERAL INSTRUCTIONS FOR COMPLETING SF 298

The Report Documentation Page (RDP) is used in announcing and cataloging reports. It is important that this information be consistent with the rest of the report, particularly the cover and title page. Instructions for filling in each block of the form follow. It is important to *stay within the lines* to meet *optical scanning requirements*.

Block 1. Agency Use Only (Leave blank).

Block 2. Report Date. Full publication date including day, month, and year, if available (e.g. 1 Jan 88). Must cite at least the year.

Block 3. Type of Report and Dates Covered. State whether report is interim, final, etc. If applicable, enter inclusive report dates (e.g. 10 Jun 87 - 30 Jun 88).

Block 4. Title and Subtitle. A title is taken from the part of the report that provides the most meaningful and complete information. When a report is prepared in more than one volume, repeat the primary title, add volume number, and include subtitle for the specific volume. On classified documents enter the title classification in parentheses.

Block 5. Funding Numbers. To include contract and grant numbers; may include program element number(s), project number(s), task number(s), and work unit number(s). Use the following labels:

C - Contract	PR - Project
G - Grant	TA - Task
PE - Program Element	WU - Work Unit Accession No.

Block 6. Author(s). Name(s) of person(s) responsible for writing the report, performing the research, or credited with the content of the report. If editor or compiler, this should follow the name(s).

Block 7. Performing Organization Name(s) and Address(es). Self-explanatory.

Block 8. Performing Organization Report Number. Enter the unique alphanumeric report number(s) assigned by the organization performing the report.

Block 9. Sponsoring/Monitoring Agency Name(s) and Address(es). Self-explanatory.

Block 10. Sponsoring/Monitoring Agency Report Number. (If known)

Block 11. Supplementary Notes. Enter information not included elsewhere such as: Prepared in cooperation with...; Trans. of...; To be published in.... When a report is revised, include a statement whether the new report supersedes or supplements the older report.

Block 12a. Distribution/Availability Statement. Denotes public availability or limitations. Cite any availability to the public. Enter additional limitations or special markings in all capitals (e.g. NOFORN, REL, ITAR).

DOD - See DoDD 5230.24, "Distribution Statements on Technical Documents."

DOE - See authorities.

NASA - See Handbook NHB 2200.2.

NTIS - Leave blank.

Block 12b. Distribution Code.

DOD - Leave blank.

DOE - Enter DOE distribution categories from the Standard Distribution for Unclassified Scientific and Technical Reports.

NASA - Leave blank.

NTIS - Leave blank.

Block 13. Abstract. Include a brief (*Maximum 200 words*) factual summary of the most significant information contained in the report.

Block 14. Subject Terms. Keywords or phrases identifying major subjects in the report.

Block 15. Number of Pages. Enter the total number of pages.

Block 16. Price Code. Enter appropriate price code (*NTIS only*).

Blocks 17. - 19. Security Classifications. Self-explanatory. Enter U.S. Security Classification in accordance with U.S. Security Regulations (i.e., UNCLASSIFIED). If form contains classified information, stamp classification on the top and bottom of the page.

Block 20. Limitation of Abstract. This block must be completed to assign a limitation to the abstract. Enter either UL (unlimited) or SAR (same as report). An entry in this block is necessary if the abstract is to be limited. If blank, the abstract is assumed to be unlimited.

PROCESSES OF EFFICIENT VISIBLE LIGHT EMISSION IN SILICON
NANOSTRUCTURES

by
MICHAEL JOHN ESTES

B.S., Electrical Engineering, Ohio State University, 1985

M.S., Electrical Engineering, Air Force Institute of Technology, 1990

A thesis submitted to the
Graduate School of the
University of Colorado in partial fulfillment
of the requirement for the degree of
Doctor of Philosophy
Department of Electrical and Computer Engineering
1995

This dissertation for the Doctor of Philosophy degree by

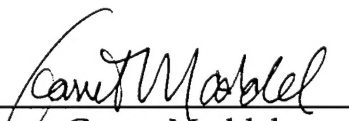
Michael J. Estes

has been approved for the

Department of

Electrical and Computer Engineering

by


Garret Meddel


Kenneth Douglas

Date November 30, 1995

Estes, Michael John (Ph.D., Electrical Engineering)

Processes of Efficient Visible Light Emission in Silicon Nanostructures

Thesis directed by Associate Professor Garret Model

Recent observations of efficient visible light emission from porous and nanostructured silicon are intriguing as they give us hope for the eventual realization of silicon-based electroluminescent devices. These results are also quite unexpected, as bulk silicon is a poor light-emitting material. Attempts to understand the mechanisms of this light emission have focused on quantum-confined silicon crystallites, luminescent surface molecular compounds, disordered silicon surfaces, and luminescent oxide-related defects. The purpose of this thesis is to further our understanding of the light emission processes in nanoscale silicon structures like porous silicon. I present the results of theoretical and experimental investigations and show that crystallinity is not required for efficient light emission from silicon, that quantum-confined states in silicon may be observable by electroabsorption spectroscopy, and that redeposition of luminescent surface compounds onto the surface of porous silicon may occur during etching.

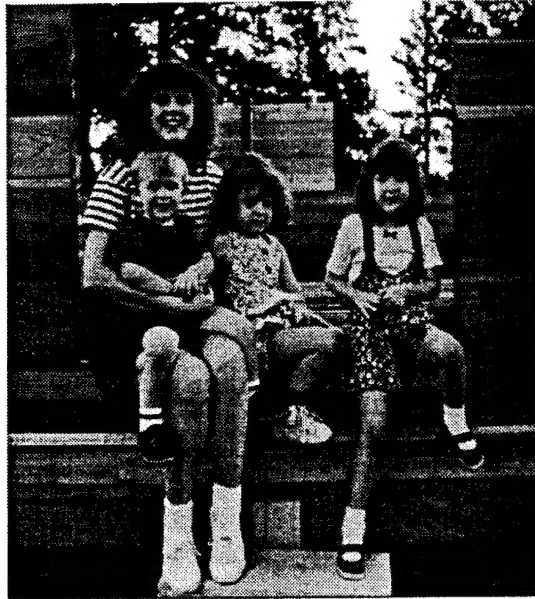
By using a simple model for luminescence in amorphous silicon, I show that size-dependent luminescence energy and efficiency are predicted for nanometer-size amorphous silicon structures. This model may explain visible light emission from anodically-etched porous amorphous silicon. Photoluminescence investigations of porous amorphous silicon, however, reveal no obvious dependence of luminescence energy on structure size. Instead, the photoluminescence

properties of this material are more consistent with light emission through discrete defect or impurity levels.

From electroabsorption measurements of free-standing porous silicon layers, I find possible evidence of quantum-confined silicon states. No clear correlation of the photoluminescence and electroabsorption energies are evident in these data. Further electroabsorption measurements would be very useful.

Finally, I show that luminescent silicon compounds may redeposit onto the porous silicon surface during porous layer formation. X-ray photoelectron spectroscopy reveals the presence of silicon bonding energies consistent with luminescent molecular compounds, such as siloxene, on the residue-covered surface of a porous silicon sample. In addition, soaking and anodizing porous silicon layers in H_2SiF_6 solution enhances the $\sim 1.6\text{-}1.5$ eV photoluminescence from these samples.

To



and



source of my inner strength.

ACKNOWLEDGMENTS

First, I must extend my utmost gratitude to the people of the F. J. Seiler Research Laboratory, particularly Dr. John Kester and Lt. Col. Barry Morgan, for getting me back to school for this PhD program. Without their support and encouragement, I would not be here. I am also indebted to Dr. Kester for graciously loaning me a much needed spectrometer and for use of Seiler Lab facilities, particularly the XPS system.

My tour here in the Thin Films Lab of Professor Garret Model has been my best Air Force assignment yet. I sincerely wish to thank Prof. Model for taking me on board, for giving me great freedom to explore and learn in the lab, and for teaching me critical evaluation of ideas and experiments. Of course, I could not have completed this program without the support and friendship of the other members of the Thin Films group. I especially want to thank Skip Wichart for making countless amorphous silicon samples and lab jigs for me, for fixing all the equipment I managed to break, and for helping me work out solutions to a number of tough problems. I am grateful to Steve Perlmutter for his quick wit and much needed moral support, to Paul Searcy for great rock climbing stories and Marathon "carnage" sessions, to Li Wang for his quiet confidence and engaging discussions, to Chris Walker for his amorphous silicon expertise, to Dave Doroski for allowing me to invade his lab space, and to Valeria Damiao for her refreshing optimism. To all the undergrads who have helped me out, Lee Hirsch, Melanie Fewings, Mark Larson, and Erji Mao, I give my utmost thanks for a job well done.

I gratefully acknowledge all those whom I have had the privilege of collaborating with, including Pawan Bhat and Russell Hollingsworth of

MRG, Inc. for introducing me to porous silicon, to Peter Saeta for many enlightening discussions on light emission processes, and to Jon Moore for many interesting discussions and for his AFM prowess.

Finally, I am grateful to Karen MacKenzie, my program managers at the Air Force Institute of Technology, and to the folks at AFROTC Detachment 105 for all their administrative support during my tenure here.

LIST OF TABLES

TABLE

4.1. a-Si:H deposition parameters.....	62
4.2. a-Si:C:H deposition parameters.....	75
5.1. Preparation conditions of free-standing porous films	99
5.2. Summary of measured electroabsorption effects.....	117
6.1. Surface atomic concentrations of porous silicon films.....	128

LIST OF FIGURES

FIGURE

1.1. Quantum confinement model.....	6
1.2. Amorphous silicon alloy model.....	9
1.3. Disordered surface states model.....	10
1.4. Oxide defect model.....	11
2.1. Diagram of anodic etching cell	16
2.2. Cross sectional diagram of porous a-Si:H sample	19
2.3. Diagram of porous silicon electroabsorption cell.....	22
2.4. Photoluminescence experimental setup	24
2.5. Electroabsorption experimental setup	30
3.1. Diagram of confined a-Si:H luminescence model.....	36
3.2. Relationship between capture sphere, capture volume, and surface capture area.....	37
3.3. Temperature dependence of the capture radius.....	40
3.4. Temperature dependence of the PL peak energy.....	41
3.5. 2-d, 1-d, and 0-d a-Si:H structures.....	45
3.6. Calculated radiative quantum efficiency vs. diameter.....	47
3.7. Calculated radiative quantum efficiency vs. temperature	48
3.8. Calculated radiative quantum efficiency vs. defect density	49
3.9. Calculated luminescence spectra of a-Si:H spheres.....	51
3.10. Calculated luminescence peak energy of 2-d, 1-d, and 0-d structures vs. diameter.....	52
3.11. Calculated luminescence spectra of distribution of a-Si:H sphere sizes.....	54

3.12. Size distributions used for Figure 3.11	55
3.13. Average PL decay time vs. peak PL energy	57
4.1. SEM cross sectional images of porous a-Si:H films.....	64
4.2. Room temperature PL spectrum of porous a-Si:H film.....	66
4.3. Room temperature PL spectra vs. doping.....	67
4.4. 83 K PL spectra vs. doping.....	68
4.5. Temperature-dependent PL spectra of porous a-Si:H.....	69
4.6. PL spectra vs. etchant HF concentration.....	71
4.7. PL spectra vs. etching current density	72
4.8. PL spectra vs. etchant HF concentration (ITO substrates).....	73
4.9. Absorbance vs. etchant HF concentration.....	74
4.10. Room temperature porous a-Si:C:H PL spectra vs. C concentration.....	76
4.11. 83 K porous a-Si:C:H PL spectra vs. C concentration	77
4.12. Aging effects on PL of porous a-Si:H.....	78
4.13. Annealing effect on PL of porous a-Si:H.....	79
4.14. PL spectra of a-Si:H on glass and on oxidized porous silicon substrates.....	81
5.1. Diagram of Franz-Keldysh effect.....	90
5.2. Published electraabsorption spectra of crystalline silicon.....	91
5.3. Measured electroabsorption of a-Si:H multilayer film	93
5.4. Simulated electroabsorption from sharp absorption feature	97
5.5. Simulated electroabsorption from distribution of absorbers	98
5.6. PL and transmission spectra of free-standing porous silicon samples.....	100

5.7. Measured electroabsorption of porous silicon sample #1307-10	103
5.8. Voltage dependence of $\Delta T/T$ of #1307-10.....	104
5.9. Diagram showing possible sources of interference fringes.....	105
5.10. Measured electroabsorption of porous silicon sample #1807-1 vs. polarity of applied voltage.....	106
5.11. Measured electroabsorption of porous silicon sample #1807-1 vs. magnitude of applied voltage.....	107
5.12. Voltage dependence of $\Delta T/T$ oscillation period of #1807-1	108
5.13. Voltage dependence of $\Delta T/T$ of sample #1807-1	109
5.14. Diagram showing possible electric field distribution	111
5.15. Measured electroabsorption of porous silicon sample #0802-1 vs. polarity of applied voltage.....	112
5.16. Measured electroabsorption of porous silicon sample #0802-1 vs. magnitude of applied voltage.....	113
5.17. Voltage dependence of $\Delta T/T$ of sample #0802-1	114
5.18. Measured electroabsorption of porous silicon sample #0802-1 vs. frequency of applied voltage	115
5.19. Measured electroabsorption of porous silicon sample #0802-2 vs. polarity of applied voltage.....	116
6.1. Diagram of proposed anodic etching mechanism of porous silicon.....	123
6.2. PL spectra of residue on n-type porous silicon.....	126
6.3. Si _{2p} XPS spectra of residue on n-type porous silicon.....	130
6.4. PL spectra of porous silicon subjected to anodization in H ₂ SiF ₆ and KNO ₃	132
6.5. PL spectra of highly porous silicon subjected to anodization in H ₂ SiF ₆	133

6.6.	PL spectra of chemically-etched porous silicon soaked in H_2SiF_6	135
6.7.	PL spectra from anodically-etched porous silicon soaked in H_2SiF_6	137
6.8.	Diagram of silicon etching through porous alumina mask	138
6.9.	PL spectra of porous alumina masks after etching.....	139
C.1.	Temperature dependence of porous microcrystalline silicon PL peak energy vs. doping.....	173
D.1.	Calculated electro-optic modulation in a-Si:H and c-Si resonant structures.....	175
D.2.	Magnitude of electroabsorption and electrorefraction in silicon.....	175
D.3.	Magnitude of free carrier absorption effects in silicon.....	176
D.4.	Measured electroabsorption of a-Si:H/a-Si:C:H multilayer.....	177
E.1.	Frequency-dependent PL spectra ac-etched porous silicon layers	180

CONTENTS

CHAPTER

I. INTRODUCTION.....	1
A. The Prospects of Silicon Optoelectronics.....	1
B. Background	2
1. Porous Silicon.....	3
2. Other Light-Emitting Silicon Nanostructures.....	4
3. The Search for a Mechanism of the Light Emission.....	5
a. Quantum Confinement in Silicon Nanocrystallites.....	5
b. Molecular Surface Species.....	7
c. Amorphous Silicon Alloys	7
d. Disordered Surface States.....	9
e. Oxide-Related Defect Centers	10
C. Overview of This Study	12
II. FABRICATION AND EXPERIMENTAL METHODS.....	14
A. Sample Fabrication.....	14
1. Porous Silicon.....	15
a. Anodic Etching Method	15
b. Chemical Stain Etching Method.....	17
2. Porous Amorphous Silicon.....	17
a. Amorphous Silicon Deposition	18
b. Porous Layer Formation.....	19
3. Free-Standing Porous Silicon Films for Electroabsorption	20
a. Anodic Etching and Lift-off	20

b. Sandwich Cell Fabrication	21
B. Experimental Characterization Methods.....	22
1. Photoluminescence	23
a. Introduction.....	23
b. Experimental Apparatus	23
2. Electroabsorption Spectroscopy.....	27
a. Introduction.....	27
b. Experimental Apparatus	29
III. A MODEL OF SIZE-DEPENDENT LUMINESCENCE IN AMORPHOUS SILICON NANOSTRUCTURES.....	32
A. Motivation for the Model.....	32
B. Model Description	35
1. Background	35
2. Quantum Efficiency.....	37
3. Capture Radius and Temperature Dependence.....	39
4. Luminescence Spectra.....	42
5. Summary of Model	43
6. Numerical Computations.....	44
C. Model Results.....	45
1. Geometry	45
2. Quantum Efficiency.....	46
3. Luminescence Spectra and Peak Energy	50
4. Effect of Size Distribution.....	52
D. Discussion.....	55
1. Spatial vs. Quantum Confinement	55

2. Mobility vs. Confinement.....	56
3. Time Dependence.....	56
E. Conclusions	58
IV. INVESTIGATION OF VISIBLE LIGHT-EMISSION FROM POROUS a-Si:H AND a-Si:C:H THIN FILMS.....	59
A. Introduction.....	59
B. Experimental Results.....	61
1. Doping Dependence	61
2. Temperature Dependence.....	68
3. Etching Dependence.....	70
4. a-Si:C:H Alloys.....	74
5. Post Treatments and Aging	77
6. a-Si:H Films Deposited onto Porous a-SiO ₂ Substrates.....	80
C. Discussion.....	82
D. Conclusions.....	86
V. ELECTROABSORPTION MEASUREMENTS OF POROUS SILICON.....	87
A. Introduction.....	87
B. Electro-optic Effects in Silicon.....	89
1. Franz-Keldysh Effect.....	89
2. DC Kerr Effect.....	92
3. Free Carrier Absorption.....	94
4. Electro-optic Effects in Quantum Size Structures.....	95
C. Measurements on Free-Standing Porous Silicon Films	99
C. Discussion.....	116

D. Conclusions.....	118
VI. INVESTIGATION OF POSSIBLE REDEPOSITION PROCESSES IN POROUS SILICON.....	120
A. Introduction.....	120
B. Silicon Etching Chemistry	122
1. Anodic Etching.....	122
2. Chemical Stain Etching.....	124
3. Redeposition.....	124
C. Redeposition Experiments.....	125
1. Analysis of the Luminescent Residue on n-type Porous Silicon.....	125
2. Anodizing and Soaking Porous Silicon Layers in H ₂ SiF ₆ Solution.....	130
a. Anodizing Porous Silicon Layers in H ₂ SiF ₆	131
b. Soaking Porous Silicon Layers in H ₂ SiF ₆	134
3. Etching Silicon Through a Porous Alumina Mask.....	137
D. Discussion.....	140
E. Conclusions	141
VII. CONCLUSIONS.....	142
A. Summary of Results.....	142
B. Suggestions for Future Research.....	144
1. Porous Amorphous Silicon.....	145
2. Electroabsorption Measurements of Porous Silicon.....	145
3. XPS Studies of Porous Silicon Surfaces.....	146
REFERENCES	147
BIBLIOGRAPHY.....	155

APPENDIX A. CONFINED AMORPHOUS SILICON MODEL: IDL PROGRAM LISTINGS.....	156
APPENDIX B. CAPTURE VOLUME AND SURFACE CAPTURE AREA EXPRESSIONS.....	168
A. 2-d Planar Slabs	168
B. 1-d Cylindrical Wires.....	169
C. 0-d Spherical Dots.....	170
APPENDIX C. ANOMALOUS TEMPERATURE DEPENDENCE OF THE PHOTOLUMINESCENCE FROM POROUS MICROCRYSTALLINE SILICON THIN FILMS.....	172
A. Sample Fabrication.....	172
B. Temperature-Dependent Photoluminescence.....	172
APPENDIX D. SURFACE NORMAL OPTICAL MODULATION IN THIN FILM SILICON: IS IT FEASIBLE?	174
APPENDIX E. FREQUENCY-DEPENDENT AC ETCHING OF POROUS SILICON.....	179

CHAPTER I

INTRODUCTION

A. The Prospects of Silicon Optoelectronics

Silicon is, and probably will be for some time to come, the most studied and well-characterized material known to mankind. In crystalline form, it is a tetrahedrally bonded, diamond structured semiconductor with an indirect bandgap of 1.12 eV at 300 K. It has high thermal conductivity, strong mechanical properties, and a chemically stable and electronically clean thermal oxide. Because of its indirect bandgap, however, crystalline silicon is a poor optical material. Electrons cannot make the optically excited indirect transition from valence band to conduction band (photon absorption) or the spontaneous indirect transition from conduction band to valence band (photon emission) without the added momentum of a third particle, such as a phonon. The net effect is that silicon has a relatively long radiative recombination time, which makes for inefficient light emission. In addition, because of its weak and shallow absorption edge, silicon has poor optical modulation properties. Thus, a

variety of group III-V direct bandgap semiconductors, such as gallium arsenide, have traditionally been the material of choice for optical modulation and light emission. Unfortunately, compound semiconductors bring with them a number of complications, not the least of which is how to integrate them with conventional silicon electronics.

Recent discoveries, however, seem to indicate that silicon itself may hold promise for optoelectronic applications, particularly light emission. The 1990 reports of Takagi *et al.* on visible light emission from ultrafine silicon particles (Takagi, 1990) and of Canham on efficient visible luminescence from anodically etched porous silicon (Canham, 1990) indicate that problems associated with bulk silicon may be circumvented simply by making structures smaller. Unfortunately, despite massive research efforts, there is still much we do not understand. In particular, it is still not clear how the material aspects of silicon change when it is isolated into very small ($\sim 1\text{-}10$ nm) structures. Questions remain about what effects crystallinity and external surfaces have on the luminescence properties in such small clusters. We seek answers to these questions not only for the physical curiosity but also that we may engineer better, more useful materials and devices.

B. Background

In this thesis I explore possible mechanisms of the light emission process in porous crystalline and porous amorphous silicon. A number of fundamental theories have been proposed and are outlined below. Before discussing theories, though, I briefly review some general properties of light emitting porous and nanostructured silicon.

1. Porous Silicon

Good reviews of porous silicon and of luminescent silicon materials in general may be found in Brus (Brus, 1994) and Canham (Canham, 1992; Canham, 1993). In addition, the proceedings of the 1994 Fall Materials Research Society meeting (1994), the November 1993 issue of the Journal of Luminescence (1993), and the January 15th, 1995 issue of Thin Solid Films (1995) all contain an enormous number of papers on porous silicon. Because of the vast amount of literature available, this review will be limited to discussion of the general properties and theories of visible light emission from porous and nanoscale silicon.

Light-emitting porous silicon may be produced by anodization in HF-containing electrolytes (Canham, 1990), by chemical stain etching in HF/oxidizer solutions (Fathauer, 1992), and by spark erosion (Rüter, 1994). Visible luminescence has been observed in both n-type (Takemoto, 1994) and p-type (Canham, 1990) porous single crystalline silicon as well as in porous polycrystalline (Guyader, 1994; Kalkhoran, 1993), microcrystalline (Bustarret, 1992a), and amorphous silicon (Bustarret, 1992a; Estes, 1995). In addition, light emission has also been observed in other anodized group IV semiconductors, such as 6H-SiC (Matsumoto, 1994) and crystalline Ge (Miyazaki, 1995). Two distinct photoluminescence (PL) bands have been observed in porous silicon. The slowly decaying red-orange band, which has stretched-exponential decay times of 10 μ sec - 1 msec, yields peak energies in the range of approximately 1.4-2.2 eV and has full width at half maxima of 0.3-0.8 eV. PL energy, intensity, and spectral width are functions of etch conditions, etchant chemistry, and wafer type and resistivity. In addition, a fast blue band has been reported that has average

decay times on the order of several nanoseconds and peak energies between 2.5-3.1 eV. The PL excitation spectrum of the red-orange band peaks in the near ultraviolet between approximately 3.5-4.0 eV, and the external quantum efficiency of this band has been reported as high as 5-10%. A number of groups have also reported observation of electroluminescence in porous silicon. Problems associated with making useful electroluminescent devices include material instability, low quantum efficiency, difficulty making electrical contact for carrier injection, and long radiative lifetimes for the red-orange luminescence.

2. Other Light-Emitting Silicon Nanostructures

Porous silicon has been notoriously difficult to characterize and understand because the material is a heterogenous mix of crystalline and amorphous materials (Tsang, 1992) with a range of structure sizes and stoichiometries. For this reason, a number of researchers have created 2-d, 1-d, and 0-d silicon nanostructures by other, more controlled methods in hopes of eliminating some of the unknowns of porous silicon. Many of these silicon nanostructures also exhibit the red-orange or blue luminescence similar to that of porous silicon. In particular, Saeta and Gallagher (Saeta, 1994b) observed weak PL peaking at ~1.7 eV in thermally oxidized 2-d silicon wedges. The PL energy remained constant with layer thickness but reached a maximum in intensity for layer thicknesses of 2-3 nm. Zaidi *et al.* (Zaidi, 1994) reported room temperature ~2.1 eV photoluminescence in oxidized 2-d silicon walls formed by anisotropic wet etching of (110)-oriented Si. Visible PL has also been observed in 1-d "quantum wires" fabricated by photoresist silylation and subsequent dry etching (Miyazaki, 1995) and by electron beam lithography and subsequent

dry etching (Nassiopoulos, 1995). In both cases, thermal oxidation was necessary to produce light emission. As for 0-d "quantum dots," Kanemitsu *et al.* (Kanemitsu, 1993a) reported ~1.65 eV PL from oxidized silicon spheres produced by gas phase nucleation of silane gas, which was cracked by laser irradiation. Luminescence energy was unaffected by particle size, which could be controlled to some degree by varying formation conditions. Kohno *et al.* (Kohno, 1994) obtained size-dependent visible PL from silicon nanocrystals in SiO₂ thin films produced by sputtering and post annealing, while Risbud *et al.* (Risbud, 1993) observed similar results from silicon remnant crystallites formed by mixing silicon powder with molten silica glass. Finally, Littau *et al.* (Littau, 1993) reported size-dependent PL from oxidized silicon nanoparticles produced by thermal cracking of disilane gas.

3. The Search for a Mechanism of the Light Emission

A wide variety of theories have been put forth to explain this rather unexpected visible light emission from porous and nanostructured silicon. Each theory tends to fall into one of five basic categories, which are briefly discussed below.

a. Quantum Confinement in Silicon Nanocrystallites

Canham originally proposed that quantum confinement of electrons and holes in narrow crystalline silicon wires with well passivated surfaces produced a widened bandgap from which radiative recombination took place (Canham, 1990). The quantum confinement concept may be understood through the simple particle-in-a-box treatment for electrons in the conduction band and holes in the valence band,

though an accurate quantitative treatment requires more sophisticated analysis (Delerue, 1993). As shown in Figure 1.1, the high energy radiative transition is predicted to arise from the band-to-band or excitonic transition due to extended states within the silicon crystallite. The broad PL spectrum is, then, the result of a distribution of wire sizes. Surfaces, in this theory, play a passive role as they provide only sources of non-radiative recombination. Experimental evidence for the quantum confinement model comes indirectly from observations of increasing luminescence energy with increasing porosity (Canham, 1990; Seo, 1994) and decreasing structure size (Wilson, 1993) and most directly from the discovery of phonon satellites in the resonantly excited PL spectrum of porous silicon at very low temperature (Calcott, 1993).

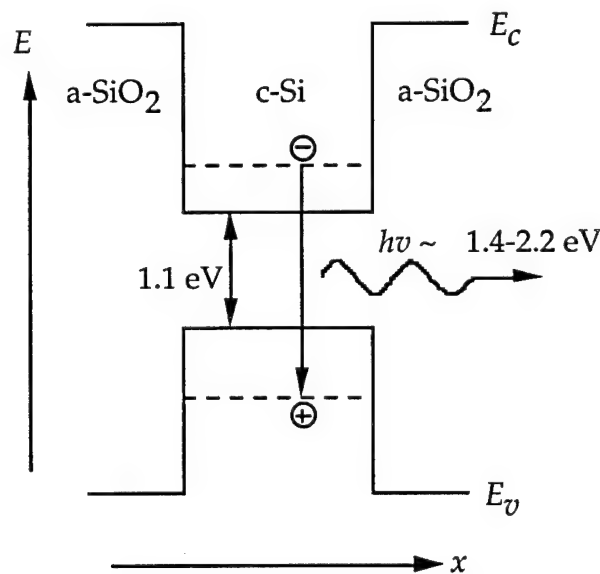


Figure 1.1. Band diagram showing the quantum confinement model of porous silicon. Confinement of small silicon nanocrystals by wide bandgap SiO_2 causes the silicon bandgap to increase. Radiative recombination is thought to occur via band-to-band transitions in the crystallites.

b. Molecular Surface Species

In 1992, Brandt *et al.* (Brandt, 1992) proposed that the red-orange luminescence from porous silicon did not arise from quantum confinement effects but rather from silicon-based surface molecular species such as siloxene. Siloxene ($\text{Si}_6\text{O}_3\text{H}_6$) is a planar silicon backbone polymer, which exhibits strong visible photoluminescence. The PL is tunable by annealing in air or by chemical substitutions. Strain effects and chemical substitutions are expected to broaden the PL spectra. Other silicon polymers, such as polysilanes $(\text{SiH}_2)_n$, have also been proposed as the luminescent agents in porous silicon (Dahn, 1994; Tsai, 1992). Takeda and Shiraishi (Takeda, 1989) calculated the bandgaps for optical transitions in 1-d chain polysilane and 2-d planar polysilane. They found that the 1-d material has a direct bandgap of ~ 4 eV while the 2-d material has nearly degenerate indirect and direct bandgaps at 2.48 eV and 2.68 eV, respectively. In porous silicon, these luminescent molecular agents would likely line the large internal surface area of the porous network. Experimental data supporting the molecular agent theory of porous silicon consists of correlations between the PL spectra, infrared absorbance spectra, Raman scattering spectra, optically detected magnetic resonance spectra, and the luminescence fatigue of annealed siloxene and porous silicon (Brandt, 1992; Brandt, 1995).

c. Amorphous Silicon Alloys

Early investigations of porous silicon indicated that a correlation exists between the luminescent upper region of the porous layer and the presence of amorphous silicon (or lack of crystalline silicon) (Noguchi,

1992; Ookubo, 1993; Perez, 1992; Prokes, 1992; Vasquez, 1992). Because of the short coherence length of electrons and holes in amorphous semiconductors, momentum is not a valid quantum number. Because phonons are not needed for the process, the luminescence efficiency in amorphous silicon is theoretically very high. Radiative recombination is thought to occur by tunneling of carriers trapped in localized conduction and valence band tail states (Street, 1981). In Figure 1.2, I show a schematic density of states diagram of the recombination in amorphous silicon. Defects inherent to the amorphous network, though, act as non-radiative recombination sites and effectively quench the room temperature photoluminescence. While the room temperature photoluminescence from hydrogenated amorphous silicon (a-Si:H) is extremely weak and at a relatively low (~ 1.1 eV) energy (Street, 1984), alloying with oxygen increases the PL energy (Carius, 1981) and has even been shown to produce efficient room-temperature PL (Augustine, 1995b). Because of the large internal surface area of porous silicon, we should expect a great deal of oxygen incorporation into the network, which may result in some alloying to form a-SiO_x. In Chapter III I present a model for luminescence in confined amorphous silicon showing that oxygen is not required for the higher energy emission. The origin of amorphous silicon compounds in porous silicon may be by amorphization of remaining crystalline silicon nanostructures below some threshold size (Vasquez, 1992), by stresses induced on the crystalline structures by oxidation (Tsang, 1992), or by redeposition of silicon during the etching process, as will be discussed in Chapter VI.

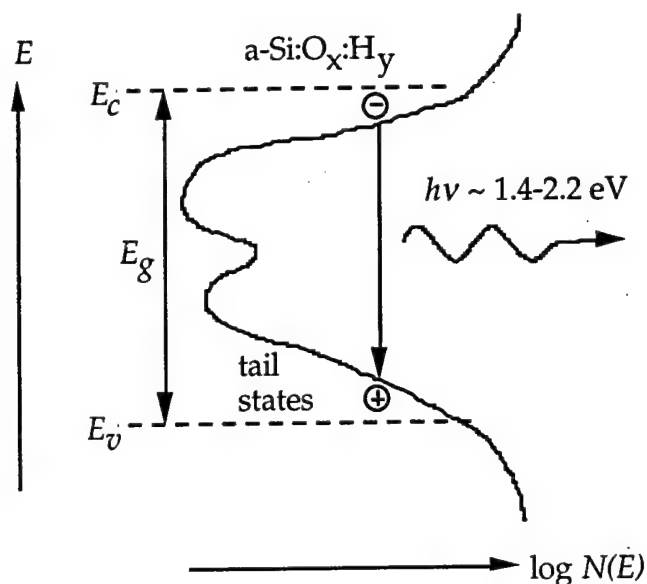


Figure 1.2. Density of states diagram showing the expected radiative transition in amorphous silicon alloys. Tail states within the bandgap, E_g , are localized while the states outside the bandgap are not. Adding O or H atoms to the network increases E_g . Because momentum is not a valid quantum number, the transition is quasi-direct.

d. Disordered Surface States

The disordered surface states model proposed by Koch *et al.* (Koch, 1993) is a mix between the quantum confinement and the amorphous silicon theories. In this theory, quantum confined silicon nanocrystals absorb the incident excitation photon creating an electron-hole pair in the extended states of the crystal. Oxidation of the nanocrystallite surface results in a transition region between the amorphous SiO_2 shell and the crystalline Si core. In this transition region, disorder-induced band tail states are expected, which may extend into the bandgap of the crystallite and therefore act as surface traps for electrons and/or holes. As shown in Figure 1.3, the radiative recombination would then be a tunneling transition between localized tail states on the surface of the crystallite. If

we look closely enough, the difference between this model and amorphous silicon theory are quite subtle. Both models propose radiative recombination between localized band tail states, which may have similar origins. The primary differences appear to be where the incident excitation light is absorbed and whether or not quantum confined nanocrystallites are necessary for the visible emission.

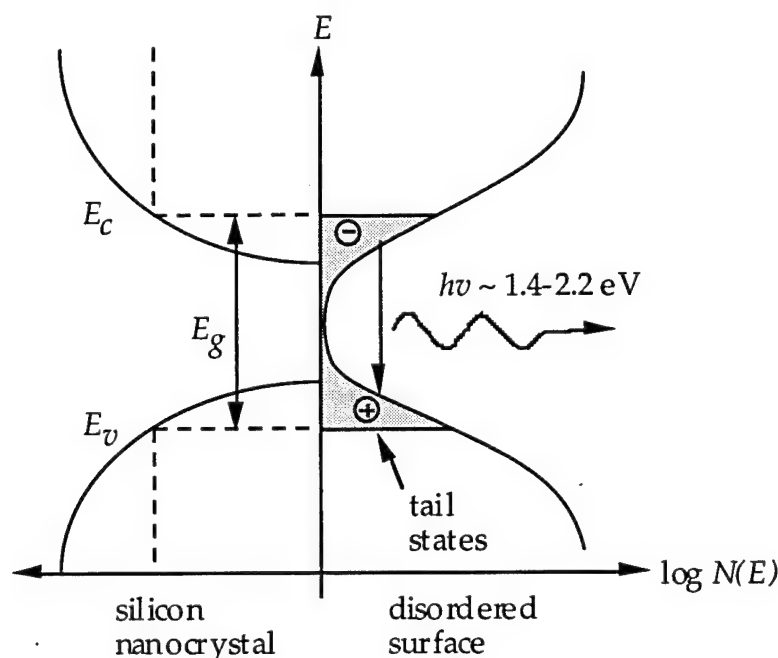


Figure 1.3. Density of states diagram showing the concepts of the disordered surface states model. Quantum confinement in silicon nanocrystallites exposes localized states on the surface that arise from bond disorder. The radiative transition is thought to occur via these localized states.

e. Oxide-Related Defect Centers

A final class of theories suggests that the visible light emission from porous silicon is due to oxide-related defect centers. According to this general theory, electron-hole pairs are optically excited in the silicon crystallite but become trapped at defect sites at the Si/SiO₂ interface. The high energy needed for carrier trapping at the surface may come from

either quantum confinement or hot carriers. The red-orange light emission is thought to be due to electronic transitions between defect centers in the oxide layer, as shown in Figure 1.4. Prokes *et al.* (Prokes, 1994) used electron spin resonance (ESR) to correlate the density of shallow donor states, which are thought to be silicon vacancies between four oxygen atoms, with the intensity of the red PL. The shallow donor states lie in the silicon bandgap and capture photoexcited electrons. In their model, the authors link shallow donor states with the presence of adjacent nonbridging oxygen hole centers (NBOHC), which have been shown to luminescence at $\sim 1.8\text{-}1.9$ eV. Stress, as well as incorporation of hydrogen or hydroxides, shifts this energy. In a similar work, Carlos and Prokes (Carlos, 1995) also correlated the ESR spin density of the EX center,

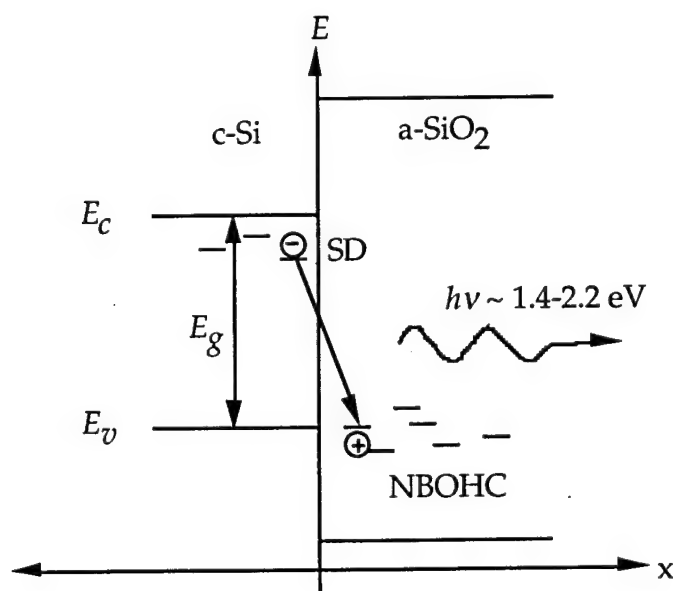


Figure 1.4. Band diagram illustrating the expected radiative transition between oxide-related defect states. The shallow donor states, SD, capture electrons generated within the silicon crystallite. Non-bridging oxygen hole centers, NBOHC, in the oxide shell trap holes.

which is similar to the shallow donor except in the oxide, with the PL intensity of porous silicon anodized for short times. Lin *et al.* (Lin, 1994) provided further experimental evidence of defect-related PL by doping luminescent porous silicon layers with samarium. After activation by gamma-ray irradiation, sharp peaks appeared in PL spectrum of the Sm-doped porous silicon that corresponded very nearly with peaks observed in Sm-doped SiO₂ glass. This result provides some indication that recombination occurs in the oxide layers of porous silicon.

C. Overview of This Study

Taken alone, each of the general theories above seem quite plausible; however, they cannot all be correct all the time for all materials. In an effort to sort out some of the controversies and gain a better understanding of the microphysical processes involved in the light emission process, I explored several aspects of porous silicon luminescence, which I have compiled in the chapters that follow. Although the chapters are not necessarily linked to one another, they do all address the overriding question: how do porous and nanostructured silicon emit visible light? I outline these chapters below.

In Chapter II, I review the fabrication and experimental procedures used in these investigations. In Chapter III, I present a model of size-dependent luminescence from *amorphous* silicon nanostructures and show that this model may explain the light emission observed in porous a-Si:H and possibly even in some porous crystalline silicon. The results of photoluminescence experiments on anodized porous a-Si:H and a-Si:C:H showing visible PL are discussed in Chapter IV in terms of testing the

validity of this model. In porous crystalline silicon, a major question that remains to be answered is: is there a correlation between the PL energy and the bandgap energies of the silicon nanocrystals? In an attempt to answer that question, we undertook an electroabsorption study of free-standing porous silicon films. I discuss the results of that study in Chapter V. Finally, to better understand the source of the amorphous material in porous silicon, we investigated the possibility that luminescent silicon compounds are redeposited during etching. I present the outcomes of that study in Chapter VI.

"I don't know how clouds form, but the clouds know how to do it, and that is all that's important."

- Anonymous Elementary School Science Student

CHAPTER II

FABRICATION AND EXPERIMENTAL METHODS

In this chapter, I describe the sample fabrication procedures and characterization methods used for most of the experiments in this study. In the first section, I describe fabrication of porous silicon samples, including porous amorphous silicon and free-standing porous silicon films for electroabsorption measurements. In the second section, I describe the two primary characterization techniques used in this study: photoluminescence and electroabsorption. Together, these measurements yield information about the band structure and luminescence centers in light emitting silicon.

A. Sample Fabrication

Discussion of sample fabrication begins with a brief overview of porous silicon formation techniques followed by a description of porous a-Si:H and free-standing porous structures.

1. Porous Silicon

One of the big attractions of porous silicon is the ease with which it may be fabricated. This inherent simplicity has helped fuel the massive worldwide research effort to understand the material. Porous silicon is typically produced by one of two methods, electrochemical (anodic) etching or chemical (stain) etching, each of which is briefly described below.

a. Anodic Etching Method

In the anodic etching method, a porous silicon layer is produced by passing a constant current through a positively biased silicon sample immersed in an electrolyte containing hydrofluoric acid (HF). Porous silicon samples for this study were etched in a teflon cell shown in Figure 2.1. The cell was based on a design by Michael Heben of the National Renewable Energy Laboratory. In our cell, a 0.5"x0.5" square silicon sample is sealed to the bottom of reservoir containing the HF electrolyte solution. A viton o-ring seals the reservoir and gives an active etching area of 0.84 cm². A copper plate on the back of the silicon wafer provides electrical contact for the anode. The cathode consists of a thin platinum strip submerged into the electrolyte.

To provide good electrical contact to the back of the silicon sample, an ~3000-4000 Å thick aluminum film was evaporated onto the backside of the silicon wafer. Good electrical contact and best adhesion were obtained by the following pre-cleaning/evaporation/post-annealing method. First, the wafer surface was degreased by cleaning with 40 sec each of trichloroethylene, acetone, and isopropyl alcohol at low speed (~400 rpm)

on the spinner followed by a spin dry for 30 sec at 3000 rpm. The native silicon oxide layer was then removed by a 10 sec dip in 10:1 HF, followed by a deionized water rinse and 30 sec spin dry. Once dry, the wafer was immediately transferred to the vacuum evaporator for metallization. After pumping down the evaporator to below 10^{-5} Torr, aluminum was evaporated at ~ 20 Å/sec. Upon removal from the vacuum system, the aluminum film was annealed at 475 °C for 1 hr in a forming gas (4% H₂ in N₂) atmosphere. For later samples, this post annealing step was omitted without any apparent detrimental effects. The silicon wafer could then be cleaved into small pieces for anodization.

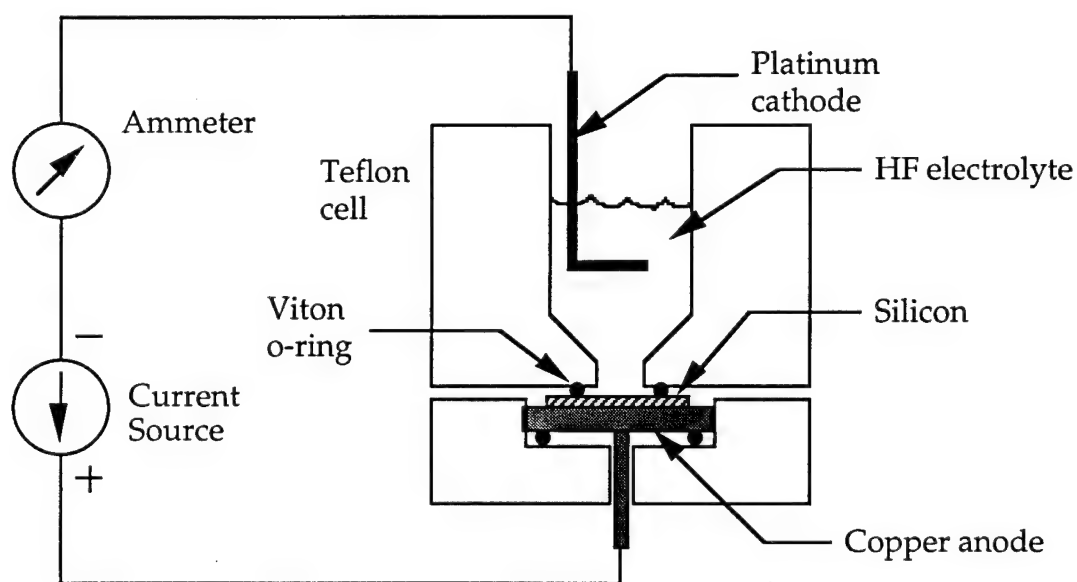


Figure 2.1 Diagram of teflon etching cell used for anodization of porous silicon layers.

Constant etching current in our setup was provided by a Keithley model 220 Programmable Current Source (0-100 mA, 0-105 V). This current source allowed good etch reproducibility as the etch time was programmable to milliseconds and the etch current to nanoamps. To monitor etching current, a Keithley ammeter was connected in series with

the cathode at ground potential. No special surface cleaning of the silicon was performed before etching, but the samples were kept free of dust and fingerprints and handled only with clean tweezers.

For the majority of the anodic etches, we used an HF:H₂O:ethanol electrolyte. A typical 25% HF solution consisted of one part 48% HF in H₂O with one part ethanol (1:1:2 HF:H₂O:EtOH).

Light-induced free carriers in the silicon during etching may strongly affect the resulting porous layer. All etches for this study were produced under ambient room light in a fume hood.

b. Chemical Stain Etching Method

Porous silicon layers may also be produced chemically, without applied current. Such chemical etches generally consist of HF plus an oxidizer. In this method, the silicon wafer is simply submerged in the etch solution for anywhere from a few seconds to several minutes. Two different chemical etches were used for this study: HF:HNO₃:H₂O (typically 1:3:5) (Fathauer, 1992; Shih, 1992) and HF:H₂SO₄:NaNO₂:H₂O, as described in Kelly *et al.* (Kelly, 1994).

2. Porous Amorphous Silicon

Porous amorphous silicon films similar to those of Bustarret *et al.* (Bustarret, 1993a; Bustarret, 1992b; Bustarret, 1995; Bustarret, 1993b) were produced in order to test the confined amorphous silicon luminescence model of the next chapter. The results of this study are discussed in chapter IV. The general sample fabrication procedures are given here.

a. Amorphous Silicon Deposition

Hydrogenated amorphous silicon (a-Si:H) films were deposited by plasma enhanced chemical vapor deposition (PECVD). The deposition system has been described elsewhere (Walker, 1992). For studies of porous a-Si:H, films of nominally 1-2 μm thickness were deposited onto 7059 glass, indium-tin oxide (ITO) coated glass, and crystalline silicon substrates. Before loading into the deposition chamber, the substrates were cleaned using an alkaline soap (Micro from International Products Corp.) and deionized (DI) water. After rinsing in DI water, the substrates were rinsed with isopropyl alcohol and spun dry at ~ 3000 rpm. The silicon substrates were subsequently dipped in 10:1 buffered oxide etch for several seconds to remove the native oxide, rinsed, and spun dry. After cleaning, the substrates were immediately transferred to the vacuum deposition chamber.

The chamber was pumped down to the 10^{-8} Torr pressure range before introduction of the deposition gases. The a-Si:H films resulted from the rf plasma decomposition of silane (SiH_4) gas. Typical deposition pressures ranged from 200-500 mT with SiH_4 gas flow rates between 5-40 sccm. Substrate temperature was approximately 210°C . Doped a-Si:H films were produced by adding dopant gases: trimethylboron ($\text{B}(\text{CH}_3)_3$) for p-doped layers, phosphine (PH_3) for n-doped layers, and methane (CH_4) for a-Si:C:H layers. Radio frequency power was generally 2 W ($15.7 \text{ mW}/\text{cm}^2$) at a frequency of 13.56 MHz. These deposition conditions yielded a-Si:H deposition rates of approximately $1\text{-}3 \text{ \AA}/\text{sec}$. At the end of the deposition, the substrate heater was turned off, the chamber flushed

with nitrogen gas, and the substrates allowed to cool to below 70 °C (approximately 2 hrs) before removal from the vacuum system.

b. Porous Layer Formation

Porous a-Si:H films were produced using the anodic etching method described in section 2.A.1.a above. a-Si:H samples on ITO/glass were etched by contacting the top ITO layer with silver paint and wrapping this contact around the back side of the glass. Etching currents from 0.1-30 mA/cm² were used with ethanoic HF solutions of 5-25 % concentration. The a-Si:H was etched until the porous layer thickness was approximately 10-50 % of the initial a-Si:H thickness, yielding the structure shown in Figure 2.2. P⁺ doped a-Si:H layers of conductivity greater than 10⁻³ Ω⁻¹cm⁻¹ gave the best porous layers in terms of surface roughness and luminescence intensity. These porous layers exhibited smooth, uniform interference colors upon anodization. Intrinsic a-Si:H films (<10⁻⁶ Ω⁻¹cm⁻¹) and n⁺ doped films (~10⁻² Ω⁻¹cm⁻¹) had to be etched under

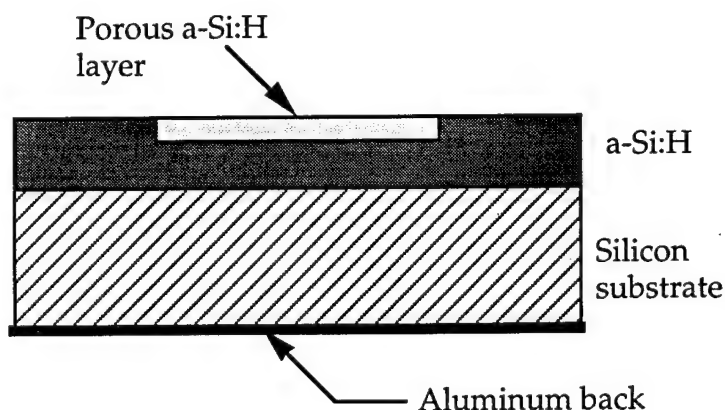


Figure 2.2 Structure of anodized porous a-Si:H sample on crystalline silicon substrate. The a-Si:H layer is nominally 1-2 μm thick and the porous layer is typically only 10-50 % of that thickness.

strong light illumination to produce porous layers, presumably due to the lack of free holes in the dark. Without light, all the electrochemistry in the i and n⁺ films took place inside pinholes in the a-Si:H and caused the a-Si:H films to lift off. After etching, the films were rinsed in ethanol and allowed to air dry.

3. Free-Standing Porous Silicon Films for Electroabsorption

Free-standing porous silicon films for use in electroabsorption measurements were fabricated using the electropolishing lift-off method (Kanemitsu, 1993b; Sagnes, 1992; von Behren, 1995; Xie, 1994). Results of the electroabsorption measurements will be discussed in chapter V. The idea here was to fabricate optically transmissive porous silicon layers across which an electric field could be applied.

a. Anodic Etching and Lift-off

Porous layers were anodically etched as described above onto p-type silicon wafers. The anodizations were typically done in 16-25 % HF at current densities of 5-20 mA/cm² for times less than 15 min. Lift-off of the porous film was accomplished by abruptly increasing the etching current into the electropolishing regime. In this etching regime, the diameter of the etched pores is significantly larger than the pore spacing resulting in a smooth, uniformly etched surface (no porous layer). Since etching occurs mainly at the bottom of the pores, the electropolish step thus "cuts" off the top porous layer from the substrate. As described in von Behren *et al.* (von Behren, 1995), simultaneously decreasing the HF concentration during the lift-off lowers the current density required for electropolishing. Current densities of 100-700 mA/cm² for up to 100 sec

were typically required for successful lift-off. Simultaneous dilution of the HF electrolyte with ethanol to ~5 % appeared to help as dilution lowered the current density required for electropolishing. Generally, the free-floating porous film remained attached at the edges at this time.

b. Sandwich Cell Fabrication

After carefully rinsing the film in ethanol, the sample was pressed film side down, while still wet, against an ITO-coated glass substrate. Pressure was applied for 1-2 min before the silicon and ITO/glass pieces were separated. Upon separation, the porous film usually stuck to the ITO and thus pulled off of the silicon substrate. It was found that spin coating the ITO with ~3000 Å of polymethyl methacrylate (PMMA) just prior to lift-off resulted in larger porous films sticking to the ITO. Also, cutting the edges of the porous layer prior to transfer to the ITO helped ensure that the film pulled completely free of the silicon substrate.

To provide a transparent top electrical contact, another ITO/glass piece was pressed down onto the porous layer to form a sandwich structure as shown in Figure 2.3. The cell was assembled between optical flats in a holder designed for liquid crystal cells. Tiny UV-curing epoxy dots between the ITO and glass plates at the periphery held the cell together. Pressure was applied by tightening the screws on the holder until the epoxy cured under a UV lamp. Shorting of the cells by ITO at the edges of the glass was a problem, so later cells were made with ITO that had been patterned and etched as in Figure 2.3.

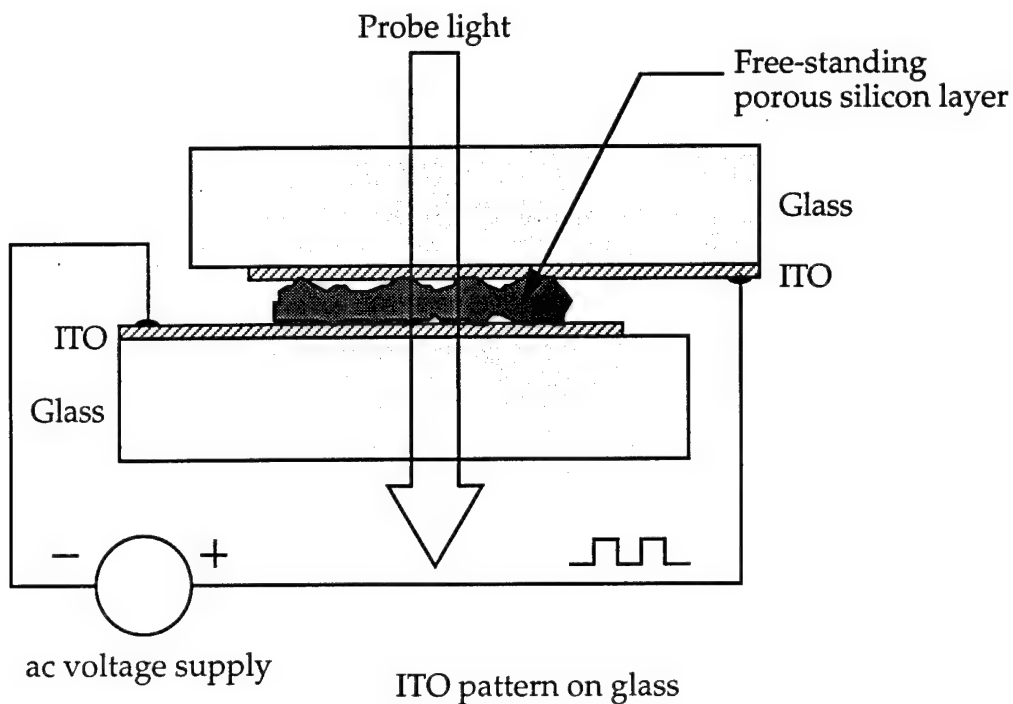


Figure 2.3 Structure of free-standing porous silicon sandwich cell for electroabsorption measurements. At the bottom of the diagram is a picture showing the ITO pattern used to avoid shorting the cell at the edges.

B. Experimental Characterization Methods

Photoluminescence and electroabsorption spectroscopies formed the core of the sample characterization used in this study. A key question in porous silicon is whether the visible luminescence originates from extended band states or from localized surface or defect states. The combination of photoluminescence and electroabsorption are designed to help elucidate the answer to this question.

1. Photoluminescence

a. Introduction

Photoluminescence (PL) is a method of studying the radiative properties of materials. The concept is fairly straightforward: illuminate a sample of the material with light of sufficient photon energy to excite electrons into a higher electronic state and detect the optical emission that results as the electrons radiatively relax back to the ground state. Understanding what the PL results mean is generally much more difficult and usually ambiguous, and so photoluminescence measurements are typically done in conjunction with other measurements on the material.

b. Experimental Apparatus

For this experiment, I used a simple photoluminescence spectroscopy setup to measure the optical intensity spectra of the light emission from porous silicon samples. A diagram of the experimental setup I used is illustrated in Figure 2.4. A light-tight black box enclosed the experiment to eliminate extraneous room light. The excitation source was a 200 W Hg arc lamp salvaged from an extinct mask aligner. This broadband light was focused through a 365 nm bandpass interference filter (Oriel #56430) into a SPEX 0.22 m monochromator with a 600 line/mm grating blazed at 500 nm to extract the intense 365 nm Hg line of the source. Entrance and exit slit widths of 2 mm were used yielding a spectral bandwidth of 13.4 nm at 365 nm center wavelength. The combination of the bandpass filter and the monochromator was necessary to filter out the strong Hg lines at 404.7, 435.8, 546.1, and 577.0 nm. The output of the monochromator was then passed through an optical chopper rotating at

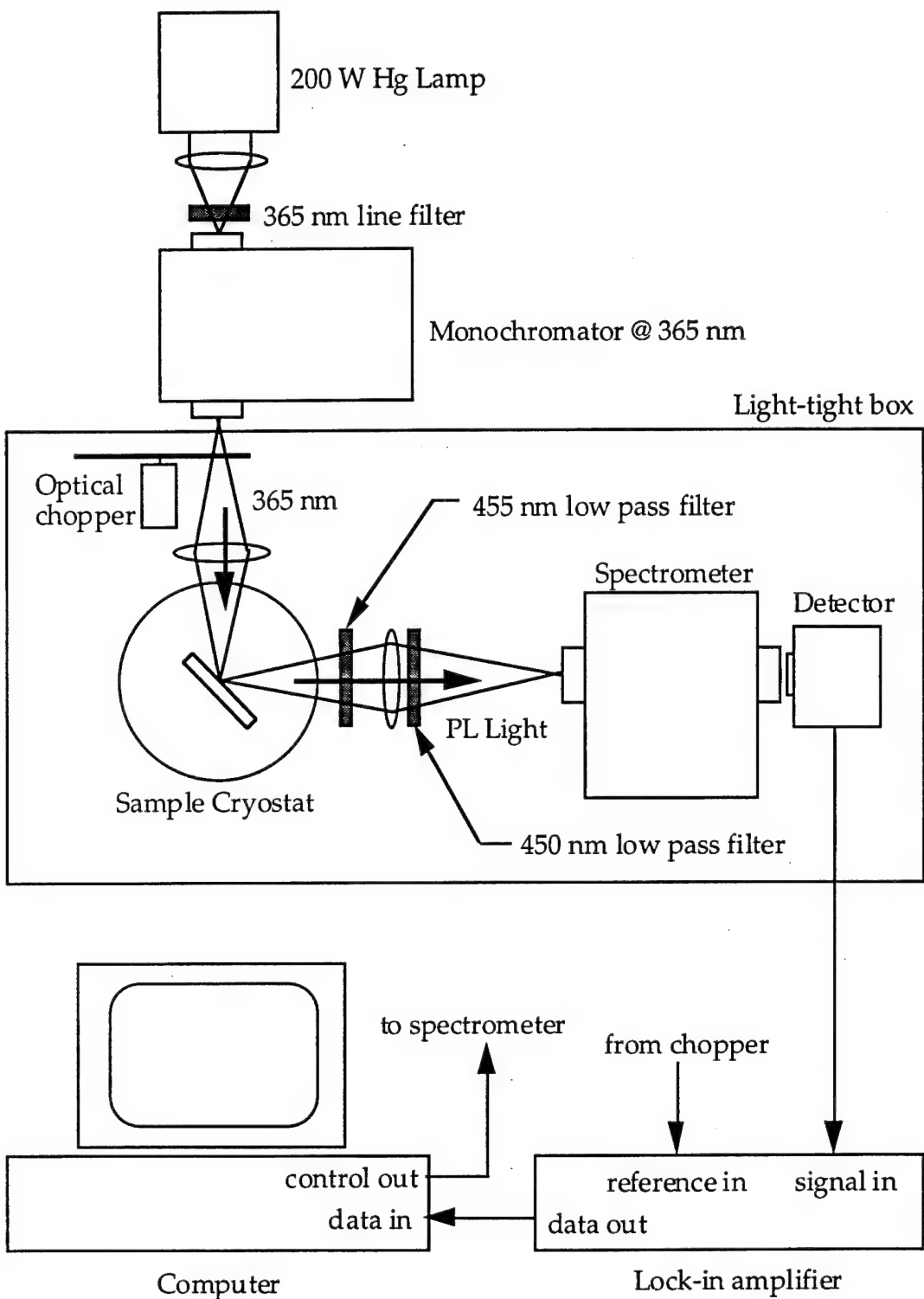


Figure 2.4 Diagram of photoluminescence experimental setup.

nominally 98 Hz and then focused down onto the sample with an f/1 fused silica plano-convex lens. The optical power illuminating the sample was approximately 0.1 mW over an area of roughly 1 mm by 3 mm (~ 3 mW/cm²).

The samples were mounted onto the cold finger of an Oxford Instruments, Ltd. model DN1754 liquid nitrogen cryostat. The cryostat vacuum was maintained via a 4" diameter oil diffusion pump with liquid nitrogen trap backed by a mechanical rotary vane pump. For low temperature measurements, the cryostat was pumped down to the mid- 10^{-6} Torr pressure range before filling with liquid nitrogen. It typically took about 15 minutes to attain this pressure range. Sample temperature (between ~ 80 K and 315 K) was controlled using a CAL Controls, Inc. CAL9000 temperature controller hooked up to the internal resistive heater and platinum thermistor inside the cryostat. Careful tuning of the feedback control and sample temperature versus thermistor reading allowed accurate control to within $\pm 5^\circ$ C.

The luminescence light was detected by imaging the illuminated sample spot through a 455 nm long pass interference filter (Oriel #57348) and a 450 nm long pass colored glass filter (Oriel #59484) onto the entrance slit of an Oriel 1/8 m spectrometer with a 600 l/mm grating blazed at 750 nm. The long pass filters eliminated the 365 nm ultraviolet source light. The 455 nm interference filter cut the 365 nm reflection by a factor of approximately 10^4 and did not fluoresce. The colored glass filter cut the remaining UV light by greater than a factor of 10^7 . Spectrometer entrance and exit slits were set at 1.24 mm by 12 mm resulting in a spectral bandwidth of 16 nm at 500 nm center wavelength. A photodetector set up

against the exit slit and connected to a Stanford Research lock-in amplifier monitored the output light. Photodetectors used included a Hamamatsu R928 photomultiplier biased at 1 kV, a United Detector Technologies UDT-PIN-10D silicon p-i-n photodiode (unbiased), and an EG&G J16-8SP-R05M germanium photodiode (unbiased). The spectrometer and lock-in amplifier were controlled by an IBM-PC compatible "286" computer running a program written in Borland Turbo-C. Data could thus be read, averaged, and stored automatically.

Photoluminescence data was normalized for spectral response of the detection system using a tungsten-quartz-halogen lamp. The tungsten lamp filament was assumed to be a Lambertian blackbody modified by the emissivity of tungsten, which was taken from the literature. Lamp temperature versus input electrical power was calibrated using an optical pyrometer. The calibration data was corrected for detection geometry yielding estimates of absolute spectral luminescent power from the sample surface. Without an external calibration standard, it was impossible to determine how accurate these estimates of absolute spectral power were. The baseline sensitivity of the setup after normalization of the data to sample spectral luminescent power was $\sim 10^{-16}$ Watts/nm for the photomultiplier detector, $\sim 10^{-13}$ Watts/nm for the silicon photodiode, and 10^{-11} - 10^{-12} Watts/nm for the germanium photodiode at the detector peak response wavelength.

2. Electroabsorption Spectroscopy

a. Introduction

Electroabsorption and electrorefraction are useful characterization techniques to measure the bandgap energy of semiconductors. The experiment may also give information about the energy of excitonic states and of the localized or extended nature of states near the band edge. As such, electroabsorption spectroscopy may be an ideal way to characterize the range of crystallite bandgaps in porous silicon. Comparison of the bandgap energies with those of the photoluminescence may then elucidate whether the luminescence is truly band-to-band recombination or something else. Direct measurements of the bandgaps in porous silicon have not to date been published.

In the electroabsorption experiment, one applies a strong electric field across the semiconductor material and measures the change in optical transmission through the sample. Scanning the wavelength of the optical probe beam allows one to measure the change in absorption across the spectrum. Generally, the strongest electroabsorption signal comes from the part of the spectrum where the absorption is changing the fastest with wavelength, such as the semiconductor band edge. If the sample has thickness, l , and is sufficiently absorptive such that interference effects are negligible, then the transmission through the sample is given by

$$T = k \cdot \exp(-\alpha l), \quad (2.1)$$

where T is transmission, k is a constant that includes reflection and scattering losses, and α is the absorption coefficient. The change in transmission with respect to absorption coefficient is given by

$$\frac{dT}{d\alpha} = -kl \exp(-\alpha l). \quad (2.2)$$

Assuming the change in transmission, ΔT , with applied field is small compared to T , then the change in absorption coefficient may be extracted from the measurement as

$$\Delta\alpha \approx -\frac{1}{l} \frac{\Delta T}{T} \quad (2.3)$$

Similarly, in a reflection geometry, the change in reflection due to the applied field may be related to the change in index of refraction of the sample surface (electrorefraction). Again neglecting interference effects and back surface reflections, the sample reflectivity is given by

$$R = \left(\frac{n-1}{n+1} \right)^2 \quad (2.4)$$

Taking the derivative with respect to refractive index yields the change in index as

$$\Delta n \approx \left(\frac{n^2-1}{4} \right) \frac{\Delta R}{R}. \quad (2.5)$$

b. Experimental Apparatus

The basic electroabsorption/electrorefraction experimental setup we* used is illustrated in Figure 2.5. For most measurements, the source light was a tungsten lamp imaged onto the entrance slit of the SPEX 0.22 m monochromator. The monochromator had adjustable slit widths and a 600 line/mm grating blazed at 500 nm. For sensitive measurements in the ultraviolet (300-400 nm), a 200 W mercury arc lamp was imaged onto the monochromator. The output of the monochromator was focused down onto the sample. Light from the sample (either reflection or transmission) was focused onto a detector, typically a United Detector Technologies UDT-PIN-10D silicon photodiode, which provided the necessary dynamic range for the measurement. Photomultiplier tubes, while very sensitive for detecting weak optical signals, are not well suited for this application as they cannot handle the strong, continuous bias light on top of which rides the small a.c.-modulated electroabsorption signal.

The key to a sensitive electroabsorption setup is elimination of as many noise and a.c. coupling sources as possible. As such, the metal optical table was grounded, care was taken to eliminate ground loops, and all signal lines were shielded as much as possible. In addition, I found that the detector had to be located some distance away from the sample to minimize inductive coupling of the a.c. sample voltage into the photodetector. The front surface of the detector was further shielded with

* Melanie Fewings, an undergraduate research assistant, was instrumental in helping me with many of the electroabsorption studies in this thesis.

a grounded metal iris, which was stopped down to the diameter of the image light. The sample holder consisted of a grounded metal plate with a small ($\sim 1/8''$) hole for optical transmission, two spring-loaded copper probe tips, and a BNC coaxial connector. The probe wires were also shielded by ground. Finally, the entire experiment was enclosed in a black, light-tight box.

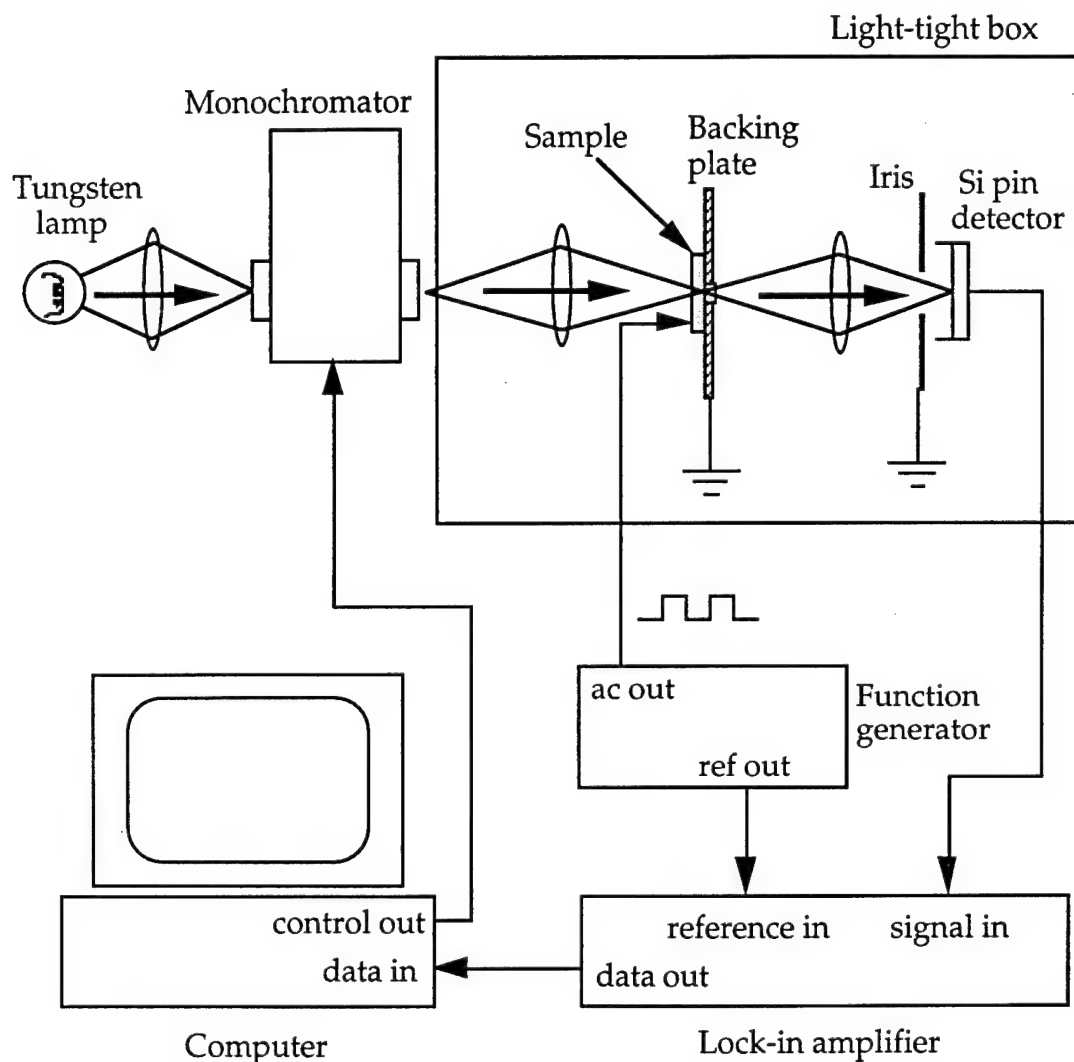


Figure 2.5 Diagram of electroabsorption measurement setup.

A Wavetek model 166 function generator provided a square wave voltage across the sample under test. In most cases, this voltage signal

alternated between zero volts and some variable voltage level with a frequency between 10 Hz and 10 kHz. Output of the optical detector was connected to a Stanford Research model SR530 lock-in amplifier, which was phase locked to the frequency of the voltage source. An IBM-PC compatible computer controlled the SPEX monochromator and monitored the output of the lock-in amplifier.

The measured electroabsorption signal required normalization after recording the data to obtain ΔT (ΔR) or $\Delta T/T$ ($\Delta R/R$). Normalization involved measuring the transmission (reflection) of the sample by chopping the incident beam with a chopper wheel. The normalized signals were thus obtained as

$$\Delta T(\lambda) = \frac{\Delta V_T(\lambda)}{V_{source}(\lambda)} \quad (2.6)$$

$$\frac{\Delta T}{T}(\lambda) = \frac{\Delta V_T(\lambda)}{V_T(\lambda)} \quad (2.7)$$

$$T(\lambda) = \frac{V_T(\lambda)}{V_{source}(\lambda)} \quad (2.8)$$

where ΔV_T is the measured lock-in voltage from the electroabsorption experiment, V_{source} is the lock-in voltage obtained from measuring the source light intensity, and V_T is the lock-in voltage obtained from measuring the source light transmitted (reflected) by the sample. Since V_{source} , ΔV_T , and V_T were measured all measured at different times, we had to assume that the tungsten source lamp was stable over the entire measurement period. While no quantitative stability measurements were ever made, good reproducibility of electroabsorption results from a given sample attest qualitatively to acceptable lamp stability.

CHAPTER III

A MODEL OF SIZE-DEPENDENT LUMINESCENCE IN AMORPHOUS SILICON NANOSTRUCTURES

A. Motivation for the Model

A significant number of observations point to a localized origin of the red-orange luminescence band in porous silicon. Specifically, Noguchi *et al.* observed strong photoluminescence (PL) from the topmost 1 μm of anodized porous silicon, a region that was determined to be primarily amorphous via transmission electron microscopy (TEM) (Noguchi, 1992). Perez *et al.* reported the observation of a strong Raman line at 480 cm^{-1} , which was attributed to amorphous silicon, in luminescing regions of anodized porous silicon (Perez, 1992). Prokes *et al.* also observed the strongest luminescence in the uppermost layers of anodized porous silicon and further correlated the redshift of the PL and intensity drop with thermal annealing with that of a-Si:H (Prokes, 1992). Hollingsworth *et al.* successfully fit the temperature dependence of the PL intensity from plasma deposited and stain etched porous silicon films with the exponential form observed in a-Si:H band tail luminescence

(Hollingsworth, 1994). In addition, a number of researchers (Bustarret, 1993b; Kanemitsu, 1994; Ookubo, 1993; Saeta, 1994a) have reported a stretched exponential time decay of the PL from porous and nanoscale silicon. Such PL, which incorporates a wide distribution of decay times, is inherent in disordered semiconductors like hydrogenated amorphous silicon (a-Si:H).

Because of its low room temperature luminescence quantum efficiency ($\sim 10^{-4}$) and < 1.1 eV emission peak energy (Street, 1984), a-Si:H seems an unlikely candidate as the active luminescent material in porous silicon. In addition, several reports appear to correlate porous silicon luminescence energy with structure size (Canham, 1990; Seo, 1994). While there has been considerable research effort into possible quantum confinement effects in amorphous semiconductors, the overall effect appears to be quite small due to the generally localized nature of the carrier wavefunctions. Neglecting quantum size effects, conventional wisdom holds that there is no size dependence to the luminescence in disordered semiconductors. Higher emission energies, such as the 1.4-2.2 eV luminescence found in porous silicon, could be obtained by alloying amorphous silicon with oxygen, nitrogen, or hydrogen (Carius, 1981). Alloying could even give a size dependence of sorts, since upon exposure to air, smaller silicon structures in the porous layer would have a greater fraction of oxide than larger structures. However, at least for plasma deposited a-Si:O:N:H films, high temperature annealing is required to obtain efficient room temperature photoluminescence (Augustine, 1995b). Thus we are faced with an apparent contradiction: evidence for

localized transitions versus evidence for a size dependence, which implies delocalized transitions.

By applying a standard model of radiative recombination in a-Si:H to spatially confined a-Si:H nanostructures, however, we may resolve some of the apparent contradictions of porous silicon luminescence. In particular, we show that the luminescence may occur from localized states and still be size-dependent. Using this model, I show that highly confined amorphous structures exhibit a blueshift and an increase in quantum efficiency of the radiative emission. While these effects are similar to the predictions of *quantum confinement* in a crystalline semiconductor, they are actually due to the statistics of *spatial confinement* in an amorphous semiconductor.

Predictions of a size dependence of the luminescence from disordered semiconductors may give insights into the mechanism of light emission from porous and nanostructured silicon. Indeed, efforts to understand this light emission in terms of a pure quantum confinement model have been complicated by observations of similar luminescence from nanostructured amorphous silicon. In particular, Bustarret *et al.* reported red-orange light emission from anodically etched and oxidized a-Si:B:H films very similar to that observed in identically anodized porous silicon wafers (Bustarret, 1992b; Bustarret, 1993b). Lazarouk *et al.* found similar results in anodically oxidized a-Si:B:H pillar structures plasma deposited into porous alumina substrates (Lazarouk, 1994). In addition, we also obtained weak visible light emission from anodized a-Si:H films. I discuss our experimental results in the next chapter. Because of the lack of crystallinity in these samples, quantum confinement effects would

probably be negligible. Thus, another mechanism must be at work in this material.

In this chapter, I present a model for photoluminescence in confined amorphous silicon nanostructures and discuss its predictions. I consider here solid, isolated a-Si:H 2-d slabs, 1-d wires, and 0-d spheres. This model, which is described in the next section, is a static (time averaged) model that predicts photoluminescence quantum efficiency and emission spectra as functions of structure size and temperature. In the last section of this chapter, I will discuss in more qualitative terms the effects of confinement on carrier mobility and recombination dynamics.

B. Model Description

1. Background

Over the past two decades, researchers have extensively explored the luminescence properties of "bulk" a-Si:H (Street, 1984). Although the exact microphysical processes involved in the luminescence are still a matter of debate (Kemp, 1995), existing models of radiative recombination describe reasonably well the luminescence efficiency (Street, 1984) and the spectral characteristics (Dunstan, 1984) of the 1.4 eV luminescence band. On the other hand, the luminescence properties of spatially confined amorphous silicon has only been briefly examined. The approach taken in this chapter is similar to that of Tiedje *et al.*, who successfully fit the observed layer thickness dependence of low temperature PL in a-Ge:H/a-Si:H multilayer films (Tiedje, 1985b) and a-Si:H/a-Si:N:H multilayers (Tiedje, 1985a). Here I consider the 2-d slab case as well as the more highly confined 1-d and 0-d cases.

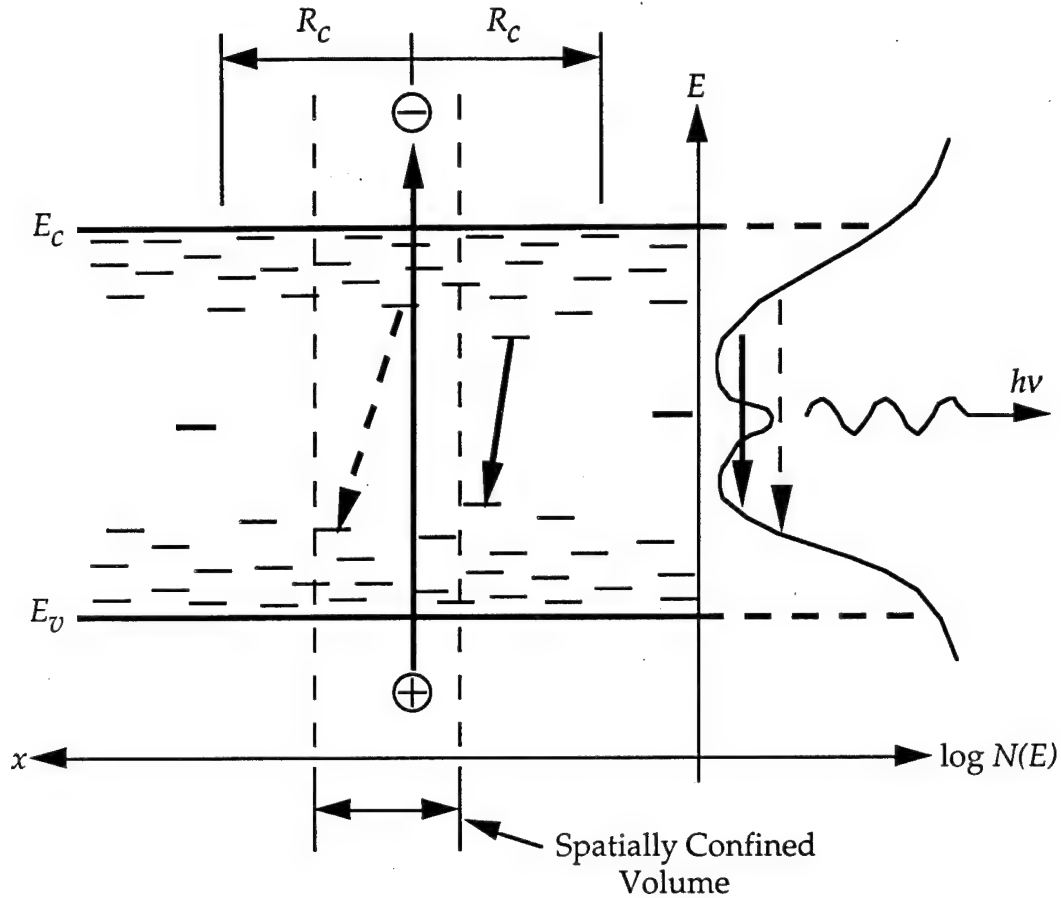


Figure 3.1 Energy band diagram of confined a-Si:H photoluminescence model. Photoexcited electrons and holes recombine via tunneling between localized tail states. By spatially limiting the recombination volume, the average luminescence energy and efficiency both increase.

In this model, photogenerated carriers quickly thermalize to the lowest energy states within some capture radius, R_c , before recombining. Radiative recombination then takes place via tunneling between deepest energy accessible conduction and valence band states *without a Stokes shift*, as illustrated in Figure 3.1. Thus, we will assume a rigid band model. In contrast to Dunstan and Boulitrop (Dunstan, 1984), let us consider the entire density of states, including both exponential band-tail and quadratic band states as potential luminescing sites. Let us also assume that the

density of states function is independent of size. For clusters of 10 Å diameter and larger this assumption should be reasonable as the density of states in amorphous semiconductors is determined primarily by nearest neighbor interactions (Adler, 1985). Radiative transitions to or from defect levels near midgap, such as the 0.9 eV low temperature luminescence band in a-Si:H (Street, 1984), will not be considered here.

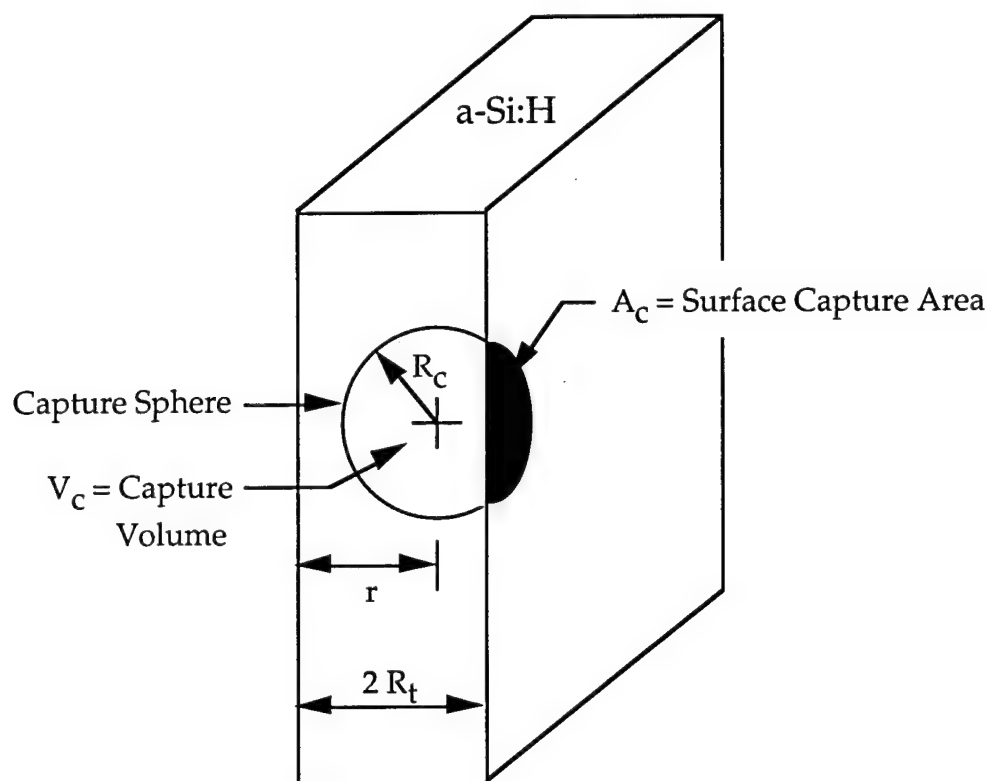


Figure 3.2 Relationship between capture sphere, capture volume, and surface capture area as truncated by a 2-d a-Si:H slab.

2. Quantum Efficiency

Non-radiative recombination occurs via tunneling to a non-radiative defect center when such a center is within the capture volume, V_c , defined by R_c , or on the surface capture area, A_c , truncating the

capture sphere. Figure 3.2 shows the relationship between the capture radius, capture volume, and surface capture area. Thus, if N_{nr} is the volume non-radiative center density (cm^{-3}) and N_{snr} is the surface non-radiate center density (cm^{-2}) then the radiative quantum efficiency for a given electron-hole pair is given by (Street, 1981)

$$\eta_i = \exp(-V_c N_{nr}) \exp(-A_c N_{snr}). \quad (3.1)$$

This expression simply gives the probability of *not* finding a non-radiative recombination center within the capture volume and on the surface capture area. For an ensemble of electron-hole pairs, the net radiative efficiency is the spatial average of η_i over the volume of the amorphous silicon structure (Tiedje, 1985b). In this case, V_c and A_c are functions of position within the structure. For the 2-d slabs, 1-d wires, and 0-d spheres, the average efficiencies are

$$\eta_{2d} = \frac{1}{R_t} \int_0^{R_t} \exp(-V_c(r) N_{nr}) \exp(-A_c(r) N_{snr}) dr, \quad (3.2.a)$$

$$\eta_{1d} = \frac{2}{R_t^2} \int_0^{R_t} r \cdot \exp(-V_c(r) N_{nr}) \exp(-A_c(r) N_{snr}) dr, \quad (3.2.b)$$

$$\eta_{0d} = \frac{3}{R_t^3} \int_0^{R_t} r^2 \cdot \exp(-V_c(r) N_{nr}) \exp(-A_c(r) N_{snr}) dr \quad (3.2.c)$$

where R_t is the radius of the 0-d sphere and 1-d wire, and half the thickness of the 2-d slab. The integration variable, r , is radius or thickness of the structure.

3. Capture Radius and Temperature Dependence

The strong temperature dependence of the a-Si:H PL may be modeled by equating the expression for the *volume* quantum efficiency (equation 2.1 with $A_c = 0$) with an expression for the experimentally observed intensity temperature dependence in a-Si:H (Collins, 1980),

$$\eta = \frac{1}{\left(\frac{1}{\eta_0} - 1\right) \exp(T/T_0) + 1}. \quad (3.3)$$

Here T_0 is an experimentally determined constant, η_0 is the low temperature maximum quantum efficiency limit, and $V_c = \frac{4}{3} \pi R_c^3$. The effective capture radius as a function of temperature is then found to be

$$R_c(T) = \left[\frac{3}{4\pi N_{nr}} \ln \left(\left(\frac{1}{\eta_0} - 1 \right) \exp(T/T_0) + 1 \right) \right]^{\frac{1}{3}}. \quad (3.4)$$

Figure 3.3 shows a plot of $R_c(T)$ plotted using nominal values for bulk a-Si:H (Collins, 1980) of $\eta_0 \sim 0.998$ and $T_0 \sim 23$ K along with $N_{nr} \sim 1 \times 10^{16} \text{ cm}^{-3}$. At low temperatures, the capture radius is determined by the maximum probable tunneling distance, which is close to 70 Å at 40 K. At higher temperatures, though, carriers have enough thermal energy to diffuse a considerable distance before being trapped and recombining. From equation 2.4, we find the room temperature capture radius in a-Si:H to be approximately 550 Å. When free carriers can move around and access a larger volume of amorphous silicon, they stand a greater chance of finding non-radiative recombination centers or very deep tail states. Thus, we should expect that at low temperatures or in highly confined amorphous silicon having well passivated surfaces, the

radiative quantum efficiency and the luminescence energy should be higher than in the bulk material at room temperature. This idea is the basis of the model.

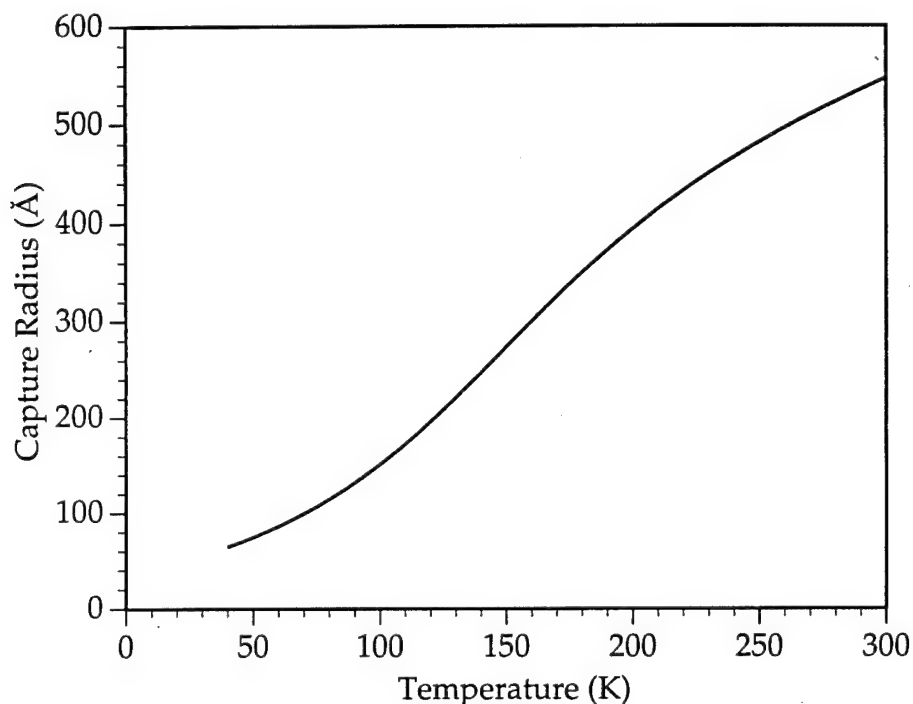


Figure 3.3 Temperature dependence of the carrier capture radius computed from equation 3.4 and the values given in the text.

I should note that this model oversimplifies the recombination process in a-Si:H, particularly at high temperatures. We have assumed that photoexcited electrons and holes diffuse independently. Thus, at high temperatures the pair may be separated well beyond practical tunneling distances for recombination. In reality, electrons and holes probably do not diffuse independently, and there probably is some correlation between deep states in the conduction and valence band tails. By its derivation, the model automatically accounts for the luminescence intensity temperature dependence. As Figure 3.4 indicates, it also accounts for the

experimentally observed decrease in luminescence energy with increasing temperature of a-Si:H (Street, 1984), although a discrepancy exists in the shapes of the modeled and experimental data. This poor correlation probably originates from oversimplification of the diffusion and tunneling processes. I have not taken into account the shift of a-Si:H bandgap with temperature; however, this shift amounts to only ~ 0.08 eV from 40 K up to 300 K (Street, 1981). For small capture volumes at low temperatures or in highly confined structures, this model should be reasonably accurate.

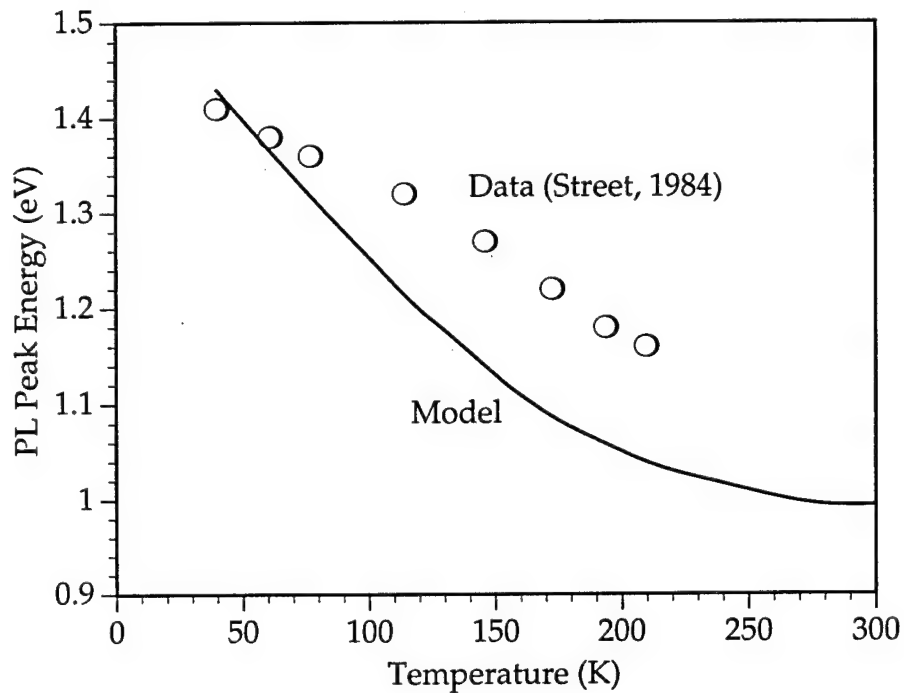


Figure 3.4 Comparison of experimental and model PL peak shift with temperature. Note qualitative agreement of redshift at higher temperatures but disagreement in shape of curve.

4. Luminescence Spectra

In this model, we will use the method of Dunstan and Boulitrop (Dunstan, 1984) to compute the luminescence spectra. The amorphous silicon density of states function ($\text{cm}^{-3}\text{eV}^{-1}$) for the conduction band is given by

$$N_c(E_1) = \begin{cases} N_{co} \exp(E_1/E_{co}), & E_1 \leq E_c \equiv 0 \\ N_{co} \sqrt{\frac{2}{E_{co}}} (E_1 - E'_c)^{\frac{1}{2}}, & E_1 > E_c \end{cases} \quad (3.5)$$

where $E_c \equiv 0$ is the conduction band mobility edge energy (eV), N_{co} is the effective density of states (cm^{-3}) at the mobility edge, E_1 is energy relative to the mobility edge, E_{co} describes the slope of the band tail, and $E'_c = E_c - \frac{1}{2}E_{co}$. E'_c is determined by equating the density of states of the exponential band tail and the quadratic band at the mobility edge energy, E_c . The valence band has a similar form for $N_v(E_2)$, where E_2 is valence band energy relative to the valence band mobility edge, E_v .

The total number of accessible conduction band states for an electron injected an energy ΔE_c above the mobility edge within the capture volume V_c is given by

$$n_c = V_c \int_{-\infty}^{\Delta E_c} N_c(E_1) dE_1. \quad (3.6)$$

The probability density, $p_c(E_1)$, gives the probability that the lowest energy conduction band state within the capture volume, V_c , lies between E_1 and $E_1 + dE_1$. It is then the probability that $n_c - 1$ states lie above the energy E_1 times the probability that the n_c^{th} state is between E_1 and $E_1 + dE_1$. Assuming that these n states are independent, $p_c(E_1)$ is thus

$$p_c(E_1) = V_c N_c(E_1) \left[\frac{\int_{E_1}^{\Delta E_c} N_c(E'_1) dE'_1}{\int_{-\infty}^{\Delta E_c} N_c(E'_1) dE'_1} \right]^{V_c \int_{-\infty}^{\Delta E_c} N_c(E'_1) dE'_1 - 1} \quad (3.7)$$

A similar expression applies for $p_v(E_2)$. The convolution of $p_c(E_1)$ and $p_v(E_2)$ yields the normalized photon flux luminescence spectrum, $P(E)$, for a given electron-hole pair:

$$\begin{aligned} P(E) &= p_c(E_1) * p_v(E_2) \\ &= \int_{E - \Delta E_v - E_g}^{\Delta E_c} p_c(E_1) p_v(E - E_g - E_1) dE_1. \end{aligned} \quad (3.8)$$

Here E_g is the mobility bandgap energy of the a-Si:H and E is the emitted photon energy. Since the luminescence spectrum is a function of capture volume, which in turn is a function of position within the amorphous structure, we must spatially average and multiply by photon energy to obtain the net intensity spectra for the three solid a-Si:H structures:

$$I_{2d}(E) = \frac{E}{R_t} \int_0^{R_t} \eta_i(r) P(E, r) dr, \quad (3.9.a)$$

$$I_{1d}(E) = \frac{2E}{R_t^2} \int_0^{R_t} r \cdot \eta_i(r) P(E, r) dr, \quad (3.9.b)$$

$$I_{0d}(E) = \frac{3E}{R_t^3} \int_0^{R_t} r^2 \cdot \eta_i(r) P(E, r) dr. \quad (3.9.c)$$

5. Summary of Model

As a way of summarizing the basic concepts of this model, let us do a thought experiment. Imagine that we have a large block of a-Si:H such that the block exhibits bulk absorption and luminescence characteristics. Now, let us cut up the block into many smaller, isolated pieces. We

assume that all surface states that would give rise to absorption or radiation are passivated. Neglecting optical scattering, the excitation spectrum for the sum total of all the small blocks will be essentially the same as for the single large block since we assume the density of states does not change with structure size. Luminescence, on the other hand, involves motion of carriers seeking out the lowest energy recombination path within some distance, R_c , of the starting location. Therefore, while in the large block all the photoexcited carriers may recombine through only a few low energy tail or defect states, in the smaller blocks carriers will find the lowest energy paths within those smaller volumes. The average energy of this radiative recombination will be higher than for the single large block. Thus by cutting up the block we will see emission blueshift and absorption remain effectively unchanged.

6. Numerical Computations

Model results were computed numerically using Interactive Data Language (IDL) from Research Systems, Inc. running on an Apple Power Macintosh computer. Equations that could be solved analytically were solved analytically before being coded into IDL. I found that using double precision mode helped eliminate occasional data errors in the computed emission spectra. I also found that using IDL's adaptive iteration routines gave better numerical results in shorter time for most numerical integrations, particularly since many of the integrands were highly nonlinear functions. IDL program listings are given in Appendix A.

C. Model Results

1. Geometry

In this section, I present calculations of luminescence the three solid a-Si:H structures shown in Figure 3.5. The results show the effects of structure size between 10 \AA and $1 \mu\text{m}$ diameter and temperature between 40 K and 300 K on the predicted photoluminescence quantum efficiency and intensity spectra. I chose these three geometries because they show the effects of confinement in a straightforward way; however, the 1-d wire and 0-d sphere structures may represent the anodically etched porous amorphous silicon structures described previously. Expressions for the capture volume and surface capture area as functions of position for these three nanostructures are given in Appendix B.

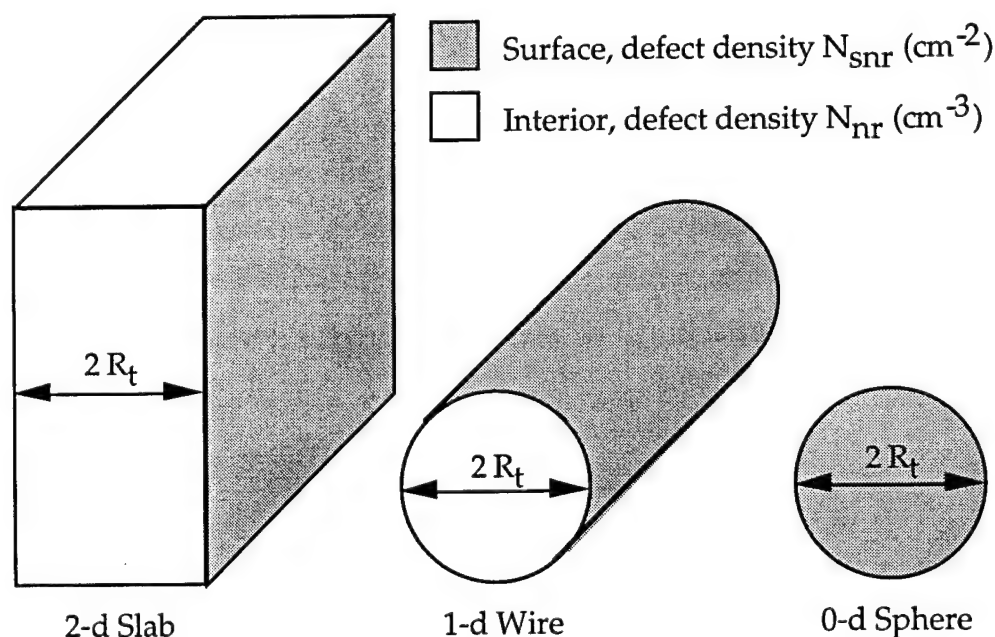


Figure 3.5 Solid a-Si:H structures used in model calculations.

2. Quantum Efficiency

Figure 3.6 illustrates the effect of structure size on room temperature quantum efficiency for the three a-Si:H structures with nominal values of the volume and surface non-radiative recombination center densities of $1 \times 10^{16} \text{ cm}^{-3}$ and $1 \times 10^{11} \text{ cm}^{-2}$, respectively. The dip in efficiency between approximately 400 and 1000 Å diameter is due to the combination of relatively large surface area *and* relatively large volume of these structures so that carriers are exposed to a maximal number of non-radiative sites. The near unity quantum efficiency of the small 1-d and 0-d structures results simply from there being very few states, and hence a small probability of a non-radiative recombination center, within these volumes. The 2-d structure, on the other hand, still has significant accessible surface area even for very thin layers and hence a much lower quantum efficiency. The predicted quantum efficiency is probably a bit too low, however, since carrier mobility will be reduced by confinement, as will be discussed in section E.2 of this chapter.

At lower temperatures, the shorter capture radius results in higher quantum efficiency for bulk structures, and so the difference in efficiency between large and small structures will be lessened. In Figure 3.7, the effect of temperature on quantum efficiency of various sizes of a-Si:H spheres is revealed. Greater spatial confinement results in reduced temperature dependence of the luminescence intensity.

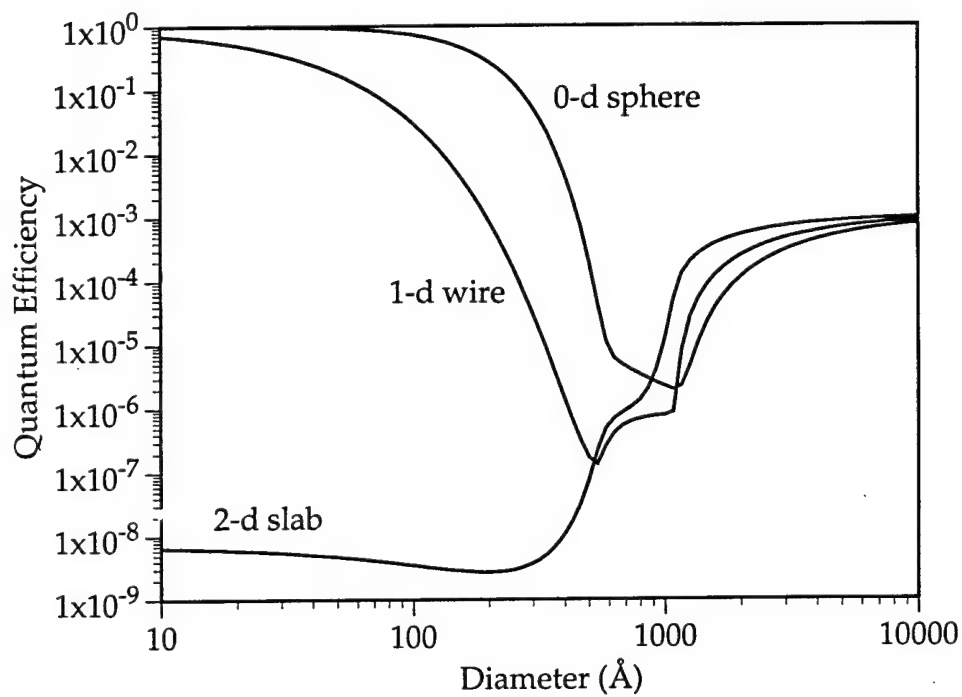


Figure 3.6 Size dependence of the room temperature internal radiative quantum efficiencies of the 2-d, 1-d, and 0-d structures. Data computed using volume and surface non-radiative recombination center densities of $1 \times 10^{16} \text{ cm}^{-3}$ and $1 \times 10^{11} \text{ cm}^{-2}$, respectively.

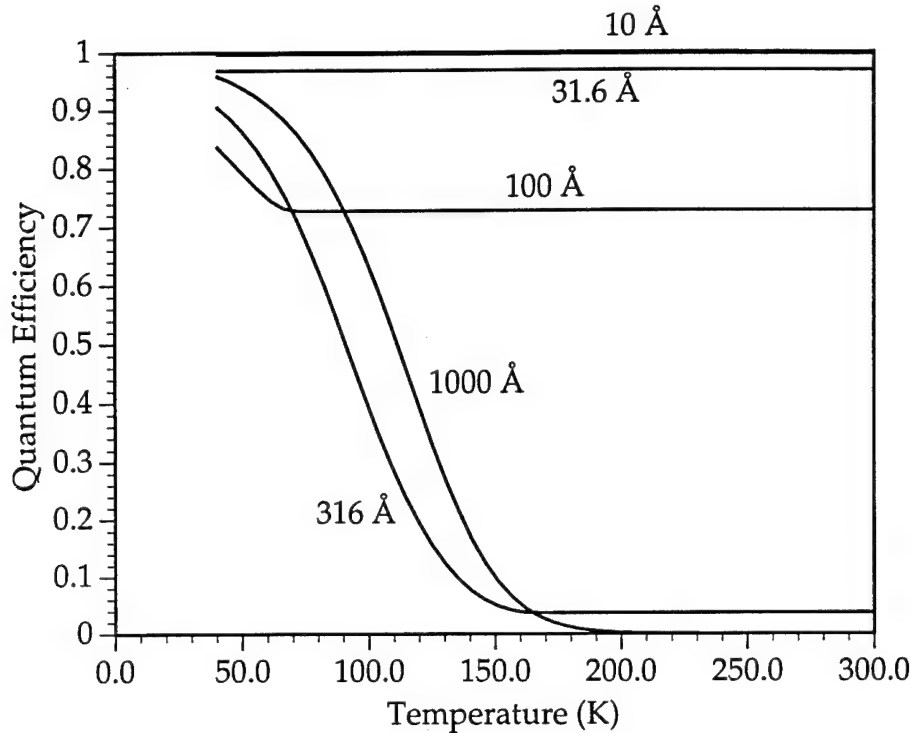


Figure 3.7 Temperature dependence of the quantum efficiencies of a-Si:H spheres of diameters from 10-1000 Å.

Note that these data represent *internal* quantum efficiency only and do not reflect losses associated with light escaping the structure. In the case of porous media composed of small 1-d and 0-d a-Si:H structures, the effective medium treatment applies for optical transmission and reflection. Thus, for highly porous material, the effective index of refraction will be considerably lower than that for bulk a-Si:H and hence a greater fraction of the luminescent light may escape as the angle for total internal reflection will be larger than for the bulk case. In conventional anodic porous silicon, for instance, von Behren *et al.* (von Behren, 1995) measured an effective index of refraction of 2.0 from a 40% porosity layer and an index of only 1.3 from a 70% porosity layer. The nominal index of refraction of bulk crystalline silicon at 632 nm is 3.85. The net effect is that

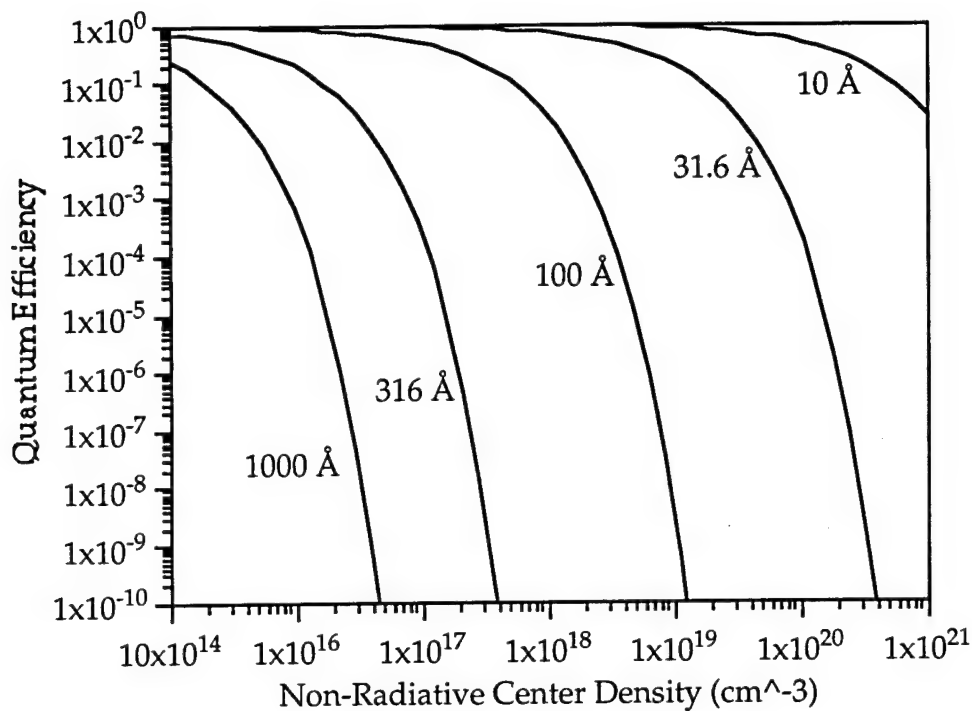


Figure 3.8 Effect of non-radiative recombination center density on radiative quantum efficiencies of a-Si:H spheres with diameters of 10-1000 Å. Surface non-radiative center density varies as the 2/3 power of the volume density on the x-axis.

in highly porous material the external quantum efficiency approaches the internal quantum efficiency.

Both surface and bulk non-radiative recombination center densities affect the predicted quantum efficiency. The values used in Figure 3.7, $1 \times 10^{16} \text{ cm}^{-3}$ and $1 \times 10^{11} \text{ cm}^{-2}$, are fairly small and indicative of very good a-Si:H. In highly defective, unhydrogenated amorphous silicon, on the other hand, the volume defect density approaches 10^{19} cm^{-3} , while the surface defect density may be as high as 10^{12} - 10^{13} cm^{-2} . Quantum efficiency versus volume defect density for spheres of several sizes are shown in Figure 3.8. In the figure, surface defect density is assumed to be volume defect density to the two thirds power. Because of lower carrier mobility in

the unhydrogenated material, the room temperature capture radius is smaller than for good a-Si:H. For simplicity, and as a worst case, I used the value of 550 Å for the capture radius in Figure 3.8, independent of defect density. The plot clearly shows that while high defect density effectively extinguishes bulk luminescence, highly confined 0-d a-Si clusters still have a substantial quantum efficiency.

3. Luminescence Spectra and Peak Energy

Predicted room temperature luminescence intensity spectra for several a-Si:H spheres with diameters ranging from 10-1000 Å are shown in Figure 3.9. These data were calculated using a mobility gap of $E_g=1.7$ eV, conduction and valence band-tail slope energies of 0.026 eV and 0.043 eV, respectively, and conduction and valence band effective densities of states of $1 \times 10^{21} \text{ cm}^{-3}$. Respective volume and surface non-radiative center densities are $1 \times 10^{16} \text{ cm}^{-3}$ and $1 \times 10^{11} \text{ cm}^{-2}$. As the sphere diameter decreases, luminescence energy and intensity increase. Larger spheres exhibit the asymmetric luminescence spectrum of bulk a-Si:H (long low energy tail) while the smaller diameter spheres show a more symmetric spectrum. These spectra are wide and symmetric because the lowest energy levels these small structures are parabolic band states. The spectra exhibit a linewidth of approximately 0.13 -0.14 eV, which increases to more than 0.25 eV in spheres smaller than 20 Å diameter. By comparison, porous silicon linewidths are typically 0.3-0.4 eV. The broad, homogeneous linewidth predicted by this model results from the statistical distribution of states in a-Si:H. A distribution of structure sizes, which one might expect to find in porous silicon, would further broaden the peak.

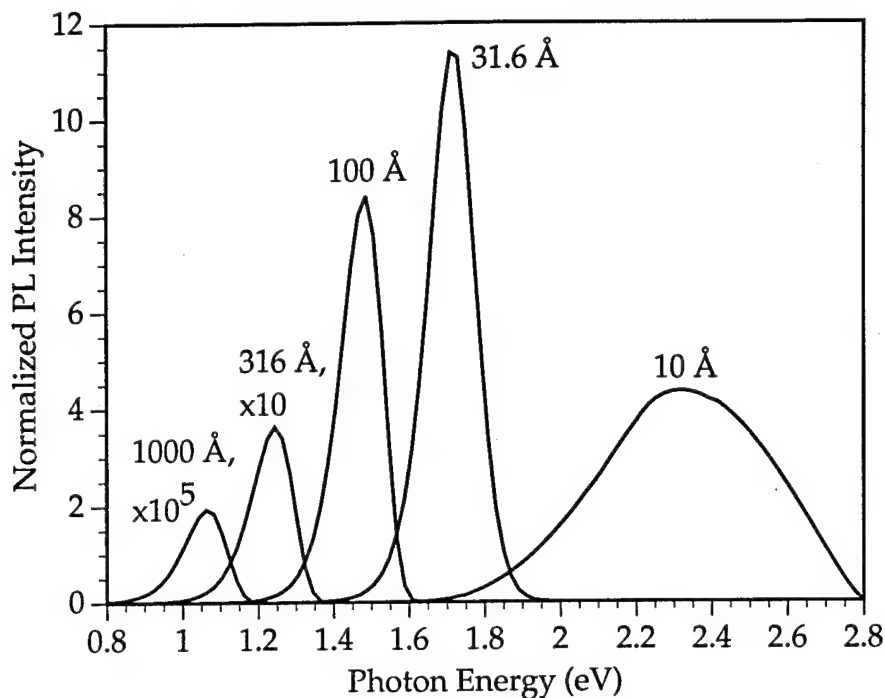


Figure 3.9 Room temperature luminescence spectra of several sizes of a-Si:H spheres. Spectra are computed using values given in the text.

In Figure 3.10 I plot the peak energy of the luminescence intensity versus size for the three a-Si:H structures using the the same parameters as for the previous graph. To obtain the nominally 1.6-2.0 eV room temperature luminescence observed in porous silicon, we would need a-Si:H spheres of approximately 10-50 Å diameter. Considering the observed structure sizes in luminescent porous silicon, this size range is reasonable. Bear in mind that the predicted room temperature peak energy for the larger sized structures may be somewhat inaccurate due to oversimplification by the model; however, since we are interested only in the most highly confined structures, this inaccuracy should not lead to significant errors.

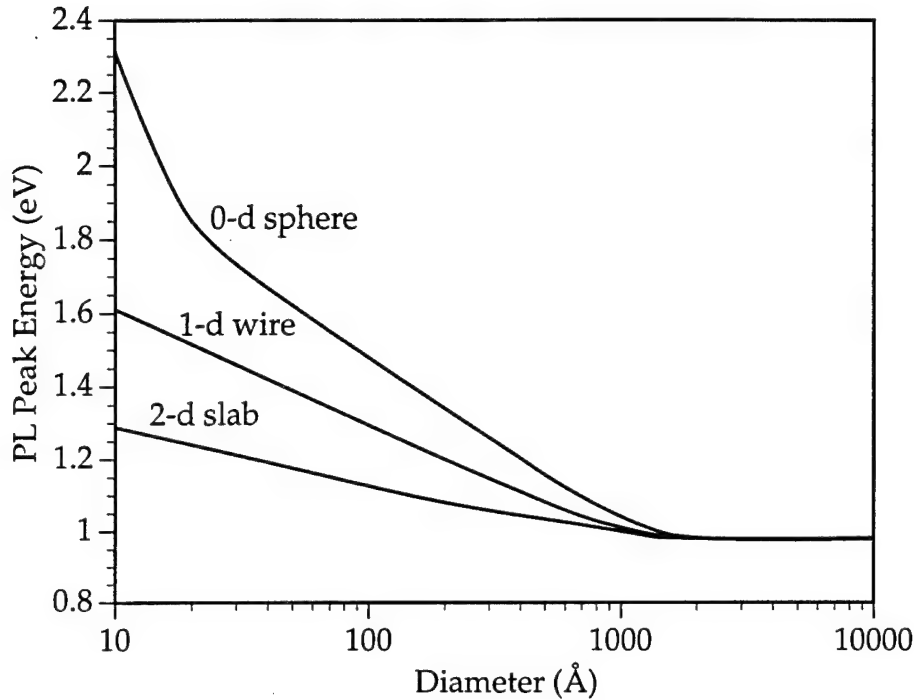


Figure 3.10 Size dependence of the room temperature photoluminescence peak energy for the three a-Si:H structures.

4. Effect of Size Distribution

In the pure quantum confinement model, we would expect the optical emission spectra from a single crystallite to be very narrow. The broad emission from porous silicon would then be explained as being due to a distribution of crystallite sizes and shapes, all with different bandgaps. In the confined amorphous silicon model, though, we saw that a broad luminescence band (about half the width of a typical porous silicon peak) results from a single size and shape structure. Additional broadening and symmetry transformation takes place if we have a distribution of particle sizes. Figure 3.11 shows the temperature dependence of predicted luminescence spectra from three different size distributions of a-Si:H spheres. The "noise" in these spectra is due to small numerical errors in

the calculation. The top graph in Figure 3.11 shows the spectra from a uniform distribution of spheres with diameters ranging from 10 Å to 1 μm. The visible peak at ~1.65 eV is due to the very smallest spheres and is essentially independent of temperature. At low temperatures, the bulk-like 1.4 eV a-Si:H peak appears along with the higher energy peak. In the lower two graphs of Figure 3.11, I show the spectra calculated from log-normal size distributions, which have been found to describe the distribution of particle sizes in semiconductor-dispersed glasses, (Kohno, 1994) of the form

$$P(u) = \frac{1}{\sqrt{2\pi}\sigma^2} \exp\left(-\frac{\ln(u)^2}{2\sigma^2}\right), \quad (3.10)$$

where u is the sphere diameter normalized by the average diameter, d ($u = \text{diameter} / d$), and σ is a normalized (dimensionless) standard deviation. I show these size distributions in Figure 3.12. In the middle graph of Figure 3.11, $d=100$ Å and $\sigma=1$, and in the bottom graph, $d=60$ Å and $\sigma=1$. These graphs clearly show an increased spectral width over the spectra in Figure 3.9 with full width at half maximum values of >0.4 eV. In addition, the effect of the sharp dip in efficiency for sizes between 500-1000 Å (Figure 3.6) is reflected in the spectra of Figure 3.11 where two peaks are evident at low temperature.

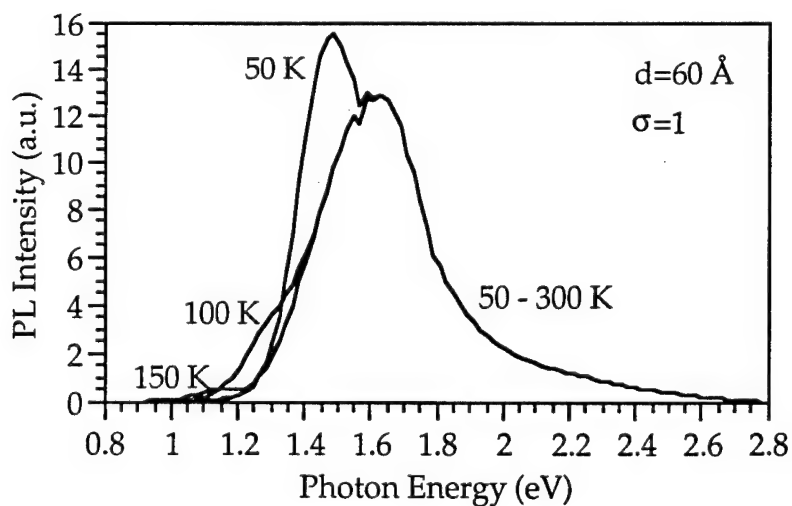
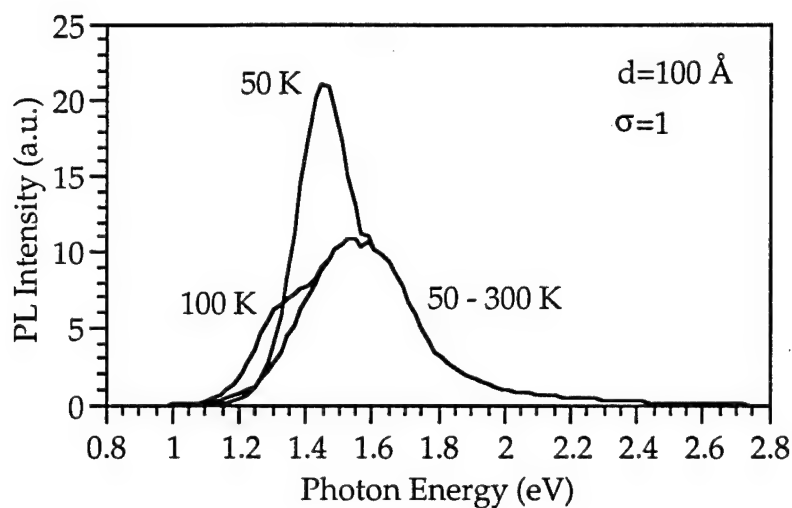
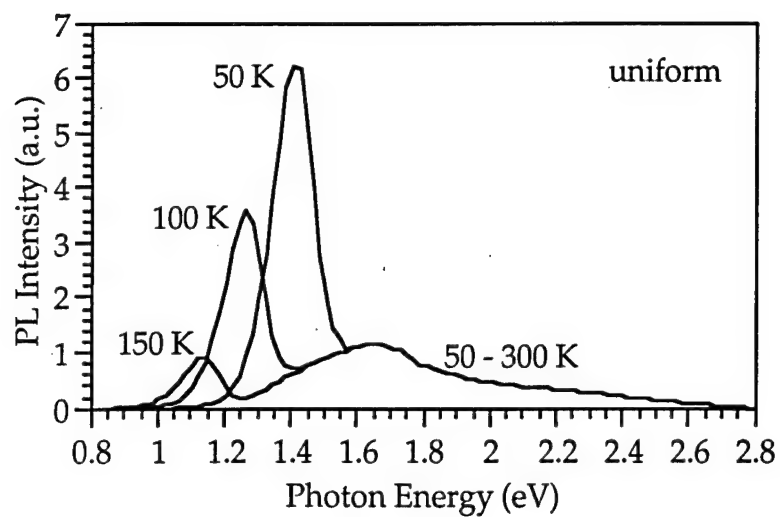


Figure 3.11 Calculated spectra for three size distributions of a-Si:H spheres at temperatures from 300 K down to 50 K.

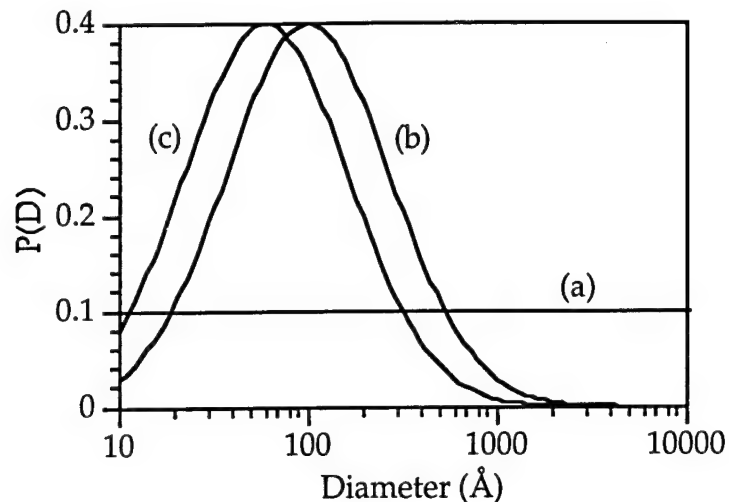


Figure 3.12. Size distributions from Equation 3.10 used for luminescence spectra of Figure 3.12: a) uniform, b) $d=100$ Å, $\sigma=1$, and c) $d=60$ Å, $\sigma=1$.

D. Discussion

1. Spatial vs. Quantum Confinement

While the effect of size-dependent luminescence from amorphous semiconductor nanostructures is similar to the effects of quantum confinement, it is instead due to the statistics of spatial confinement. In contrast to quantum confinement in a crystalline semiconductor, no coherent carrier wavefunction interactions are assumed to take place in the amorphous semiconductor. Thus, the density of states remains unchanged by the confinement. Carriers are localized into band tail states, whose density increases monotonically from mid-gap up into the band. It is the statistics of lowest energy states within a volume that causes luminescence energy to increase as volume decreases. Unlike quantum confined structures where the density of states is modified by confinement, the absorption spectrum of confined amorphous silicon should remain relatively unchanged from the bulk case.

2. Mobility vs. Confinement

Spatial confinement also has a more subtle effect on carrier motion. In a-Si:H, carrier motion is thought to occur via tunneling between adjacent states that are at nearly the same energy. Using this concept, the mobility edge may then be derived as the energy at which the density of states is high enough that the tunneling probability to an adjacent state approaches one. In the 3-d case, that density is around 10^{21} cm^{-3} . In very thin 2-d sheets or 1-d wires, however, a higher density of states is required for the tunneling probability to approach one since carriers can only tunnel in two or one dimensions, respectively. By reducing the dimensions available for tunneling motion of a carrier at some fixed energy, we have reduced the probability of that carrier finding a percolation path along which to propagate through the amorphous silicon network. The net effect is a reduction of carrier mobility and a widening of the mobility gap. Our model does not take this effect into account. Reduced carrier mobility in confined a-Si:H structures should further blueshift the luminescence beyond that predicted by this model. Assuming that the confining surfaces are well passivated, an increase in quantum efficiency should also be realized.

3. Time Dependence

In this luminescence model we have assumed that carriers recombine by tunneling between spatially separated conduction and valence states. The average tunneling time for an electron and hole separated by a distance R is given by (Street, 1984)

$$\tau = \tau_0 \exp(2R/R_0), \quad (3.11)$$

where ω_0 is the tunneling attempt rate ($\sim 10^8 \text{ sec}^{-1}$ for the radiative transition) and R_0 is the effective Bohr radius. According to Street, this expression is valid for $R > R_0$, where $R_0 \sim 10 \text{ \AA}$. A distribution of tunneling distances results in a distribution of decay times and, hence, the stretched-exponential luminescence decay observed in both amorphous and porous silicon.

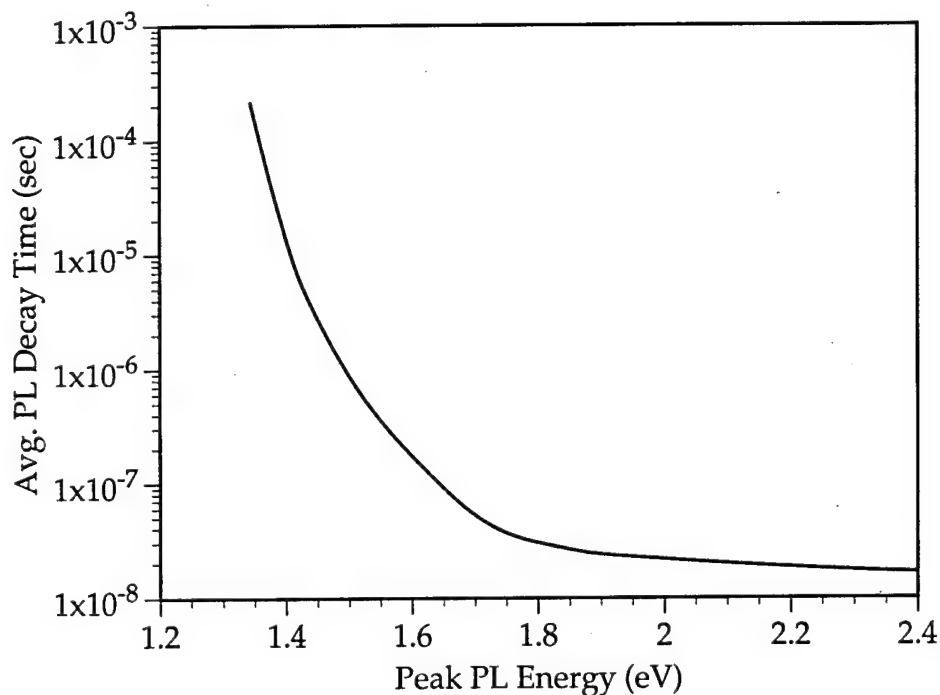


Figure 3.13 Average photoluminescence decay time of a-Si:H spheres versus peak emission energy. Plot obtained by combining Equation 3.10 with data from Figure 3.10.

By restricting R through spatial confinement, the average luminescence decay time becomes shorter. If we estimate the average tunneling distance in an a-Si:H sphere to be roughly the sphere radius, we can plot the average decay time versus peak energy, as in Figure 3.13 where I have combined Equation 3.10 with the peak energies versus sphere radius from Figure 3.10. In this graph, I want to show that as

sphere size decreases, PL energy increases, tunneling distance decreases, and recombination time decreases. Note that for the nominally 1.4-2.2 eV porous silicon peak energies, average decay times would range from about 10^{-5} - 10^{-8} sec. Here the model differs somewhat from observations in porous silicon, where average luminescence decay times range from about 10^{-4} - 10^{-6} sec.

E. Conclusions

I have shown that under the assumptions of the a-Si:H luminescence model of Dunstan and Boulitrop, size-dependent luminescence is predicted for spatially confined a-Si:H nanostructures. In addition, emission efficiency also generally increases for structures less than ~ 100 Å in size due to the decreased probability of finding a non-radiative recombination center. Highly confined 0-d spheres can tolerate large volume defect densities $>10^{20}$ cm $^{-3}$ without considerable loss in quantum efficiency. Luminescence peak energies in excess of 2 eV are possible in a-Si:H spheres with diameters <20 Å. The luminescence spectra exhibit homogeneous linewidths of ~ 0.14 eV in large structures to >0.25 eV in spheres <20 Å diameter. The effect of a distribution of structure sizes is an increase in the spectral width. Other, more subtle effects may be predicted for highly confined a-Si:H structures, such as a decrease in the luminescence decay time and an effective widening of the a-Si:H mobility gap.

CHAPTER IV

INVESTIGATION OF VISIBLE LIGHT-EMISSION FROM POROUS a-Si:H AND a-Si:C:H THIN FILMS

A. Introduction

In Chapter III, I presented a theory for size-dependent luminescence in confined amorphous silicon nanostructures. To test this model, we* produced a series of porous a-Si:H and a-Si:C:H films and ran a series of experiments on these samples designed to: 1) look for evidence of size dependent luminescence, and 2) check if a-Si:H band states are involved in the radiative process. Since these films contain no crystalline silicon, we may neglect quantum confinement effects. If our experiments show that the luminescence involves a-Si:H band states, then we can rule out oxygen-related defect centers (Carlos, 1995; Prokes, 1994) and surface

* The help of Skip Wichart, who deposited the a-Si:H and a-Si:C:H films, and Lee Hirsch, who made and tested many of the porous layers, was vital to the success of these experiments.

molecular agents (Brandt, 1992; Kanemitsu, 1995) as the source of the light emission. If, in addition, our experiments indicate that the luminescence energy is size dependent, then we have partially verified the validity of the confined amorphous silicon model. Unfortunately, we cannot easily separate size effects due to alloying of the porous a-Si:H network with oxygen (Augustine, 1995b) from the effects of passivating the porous a-Si:H surfaces with SiO₂ as per our model. We will have to accept that this ambiguity exists.

Using the fabrication techniques described in Chapter II, we produced a series of porous a-Si:H layers that yielded weak red-orange photoluminescence under UV excitation. Several groups have reported the formation of porous amorphous silicon, albeit without light emission, by anodic etching (Bao, 1993; Yakimov, 1995) and chemical stain etching (Bao, 1993; Bustarret, 1995; Higa, 1994; Jung, 1992; Yakimov, 1995), but only two groups have previously reported visible light emission from porous amorphous silicon. Bustarret *et al.* (Bustarret, 1993a; Bustarret, 1992b; Bustarret, 1995) observed visible luminescence in porous a-Si:B:H films anodized in 25% ethanoic HF at 10 mA/cm². The authors further reported that the emission efficiency could be enhanced by electro-oxidation of the porous layers in 0.1 M KNO₃. Lazarouk *et al.* (Lazarouk, 1994) measured red light emission from phosphorous-doped n-type a-Si:H pillar structures anodized in 1% aqueous HF at 2 mA/cm². It is not clear whether the anodization of the pillar structures resulted in formation of a porous layer or in size reduction and passivation of the a-Si:H pillars. These results strongly suggest that crystallinity is not a prerequisite for visible light emission from silicon nanostructures.

In this chapter I present the results of experiments designed to test the confined amorphous silicon model. As I discuss in the first section, doping type and concentration strongly affect how the films etch and whether they exhibit visible light emission. In the second section, I present the results of temperature-dependent PL, which indicate that discrete levels may be involved in the luminescence. By varying anodic etching conditions, we were able to produce porous layers with a range of porosities; however, as I discuss in the third section, we found that layer porosity does not affect PL emission energy. We varied bandgap by adding carbon to the a-Si:H films during growth to produce a series of a-Si:C:H films. The ability to control bandgap is unique to the amorphous case; one cannot adjust the bandgap of the starting crystalline silicon material. In the fourth section, I show that PL energy correlates well with the bandgap of the starting a-Si:C:H layer. In section five I show the effects of oxidation and high temperature annealing on the PL of the porous layers. Finally, in section six I give evidence of size-dependent PL from a-Si:H deposited onto passive porous substrates.

B. Experimental Results

1. Doping Dependence

We prepared a series of five a-Si:H films to investigate the effects of doping on the etching and luminescence properties of our a-Si:H. These samples included p^{++} , p^+ , p^- , i , and n^+ -doped films. The deposition parameters and resulting bandgaps (Pankove, 1987) and conductivities are given in Table 4.1. Film #95-44 in Table 4.1 was an effort to approximately reproduce the film stoichiometry of Bustarret *et al.*, whose films appear to

Table 1: Deposition parameters, bandgaps, and conductivities of the series of doped a-Si:H films used in this study. The columns under flows are for the atomic flow rates of the active atoms in the deposition gases used: silane (Si), 1% trimethylboron in helium (B), phosphine (P), and hydrogen (H₂).

Film	Type	Flows (sccm)				Pressure (mT)	RF Power Density (W/cm ²)	Tauc Bandgap (eV)	Conductivity ($\Omega^{-1}\text{cm}^{-1}$)
		Si	B	P	H ₂				
95-44	p ⁺⁺	5	0.2	0	45	300	0.079	1.62	1.6×10^{-6}
95-30	p ⁺	30	0.3	0	0	500	0.016	1.75	2.1×10^{-5}
95-35	p ⁻	40	0.4	0	0	300	0.016	1.75	1.0×10^{-6}
95-36	i	40	0.04	0	0	500	0.016	1.76	8.0×10^{-10}
95-37	n ⁺	40	0	0.4	0	300	0.016	1.69	7.9×10^{-3}

have a very high boron concentration. Under the deposition conditions used for the remainder of the films, we expect the film structure to be completely amorphous.

Boron-doped a-Si:H films etched readily in 25% ethanoic HF. The resulting porous layer in highly doped p⁺ films was smooth and specular, showing uniform interference colors. More lightly doped p-type films also showed interference colors, but the surfaces were rough and optically diffuse. We could obtain a porous layer from the highly boron-doped #95-44 film only by anodic etching in 50% aqueous HF at 1 mA/cm². Lower HF concentrations or higher etching currents resulted in electropolishing (uniform, non-porous etching, not necessarily shiny and smooth). We found that while the p⁺ and p⁻ samples yielded porous layers over a wide range of HF concentrations and etching currents, n-type and intrinsic films required strong white-light illumination in excess of

AM1 ($\sim 100 \text{ mW/cm}^2$) intensity to produce porous layers with 25% HF solution and 1 mA/cm^2 etching current. Even so, the resulting porous films from the i and n^+ samples were black and very diffuse indicating strong light scattering and absorption, presumably due to larger feature sizes than for the p-type films.

While we consistently obtained weak blue light emission from stain-etched p^+ a-Si:H films, we found no trace of red PL in these spectra. These findings, coupled with our previous efforts with microcrystalline silicon films, lead us to conclude that crystallinity is a prerequisite for the red-orange light emission from stain etched films (Hollingsworth, 1994). It may be that either the morphologies of the stain etched and anodized films are significantly different or that the two etching processes lead to different radiative processes.

Figures 4.1.a and 4.1.b show scanning electron microscope images of cross sections of porous layers on (111) Si. In Figure 4.1.a, the uniformly etched porous layer of a p^+ sample, etched at 1 mA/cm^2 in 25% HF, is evident as the white top layer of thickness $\sim 0.08 \mu\text{m}$ while the remaining a-Si:H film of thickness $\sim 0.58 \mu\text{m}$ and the crystalline silicon substrate below show up as grey. The initial a-Si:H film was $\sim 2.15 \mu\text{m}$; we believe that the remaining top portion of the film disintegrated during the ethanol rinse as the film color changed during rinsing. In Figure 4.1.b, we see the much rougher porous layer produced on a p^- sample at 30 mA/cm^2 in 25% HF. The p^- samples did not seem to have the film disintegration problems of the p^+ layers. As the figure also shows, this particular sample had a large number of pinholes that etched through to the (111) Si substrate below. These etch pits do not appear to affect the

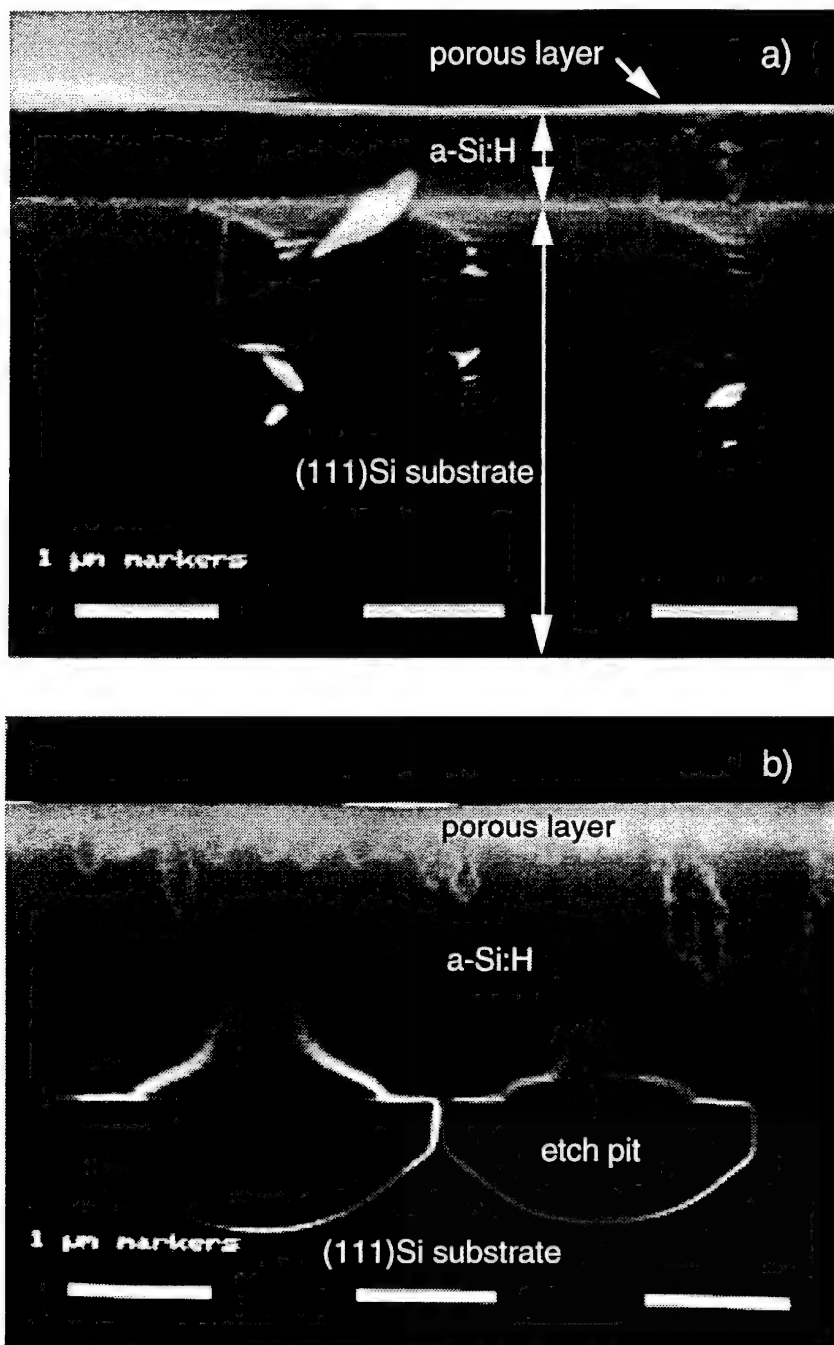


Figure 4.1. Scanning electron micrographs of the cross sectional views of a) porous p⁺ a-Si:H and b) porous p⁻ a-Si:H. The images clearly show the top porous layers, which appear white, and the remaining unetched a-Si:H films. The p⁺ porous layer in (a) etched smoothly and uniformly but only a thin ~800 Å porous layer remained after rinsing. The p⁻ porous layer appears very rough and non-uniform and is thicker than the p⁺ layer.

luminescence of the sample as the 365 nm light is completely absorbed by the remaining a-Si:H layer before reaching the substrate. Porous a-Si:H layers formed on ITO/glass substrates exhibited nearly identical PL to that from layers on crystalline silicon substrates, clearly demonstrating that the light emission does not come from etch pits in crystalline silicon substrates. Amorphous silicon films on polished silicon substrates seemed to have fewer pinholes than the films on ITO/glass and hence etched better in general.

Figure 4.2 shows the room temperature PL spectrum of a p^+ porous a-Si:H sample (#95-30) etched at 1 mA/cm^2 for 15 min in 25% HF. The data have been normalized to the instrument response. The two traces in Figure 4.2 represent PL taken at the same spot with a PMT detector (thick line) and a silicon photodiode (noisy signal). The spectrum resembles previously reported PL of porous a-Si:B:H (Bustarret, 1992b) with a room temperature peak energy near 1.6 eV and full width at half maximum (FWHM) of about 0.6-0.7 eV. In contrast to the 2-5% external quantum efficiencies reported by Bustarret *et al.* (Bustarret, 1995), however, our room temperature efficiencies were closer to 0.01-0.1%. In fact, the dim orange colored PL from these samples was just barely visible to the eye in a darkened room. For this reason, it was very difficult to obtain room temperature PL spectra using the silicon photodiode detector, which lacked the sensitivity of the PMT.

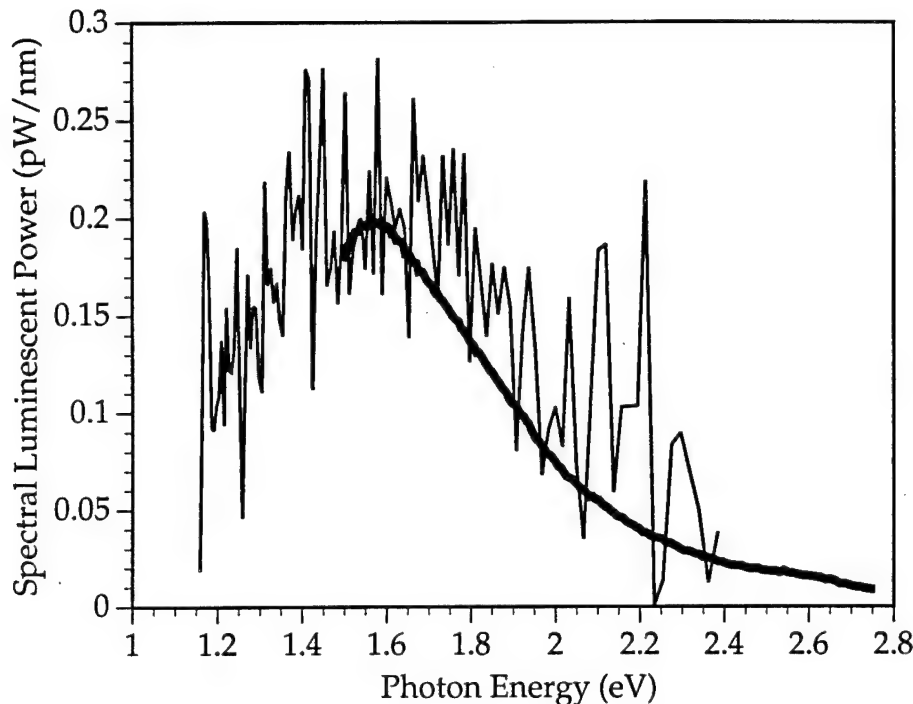


Figure 4.2. Room temperature photoluminescence spectrum of a p^+ porous a-Si:H sample on (111)Si. The thick line corresponds to PMT detector data, while the thin noisy line corresponds to Si photodiode detector data. Spectrometer slits were set at 3.16 mm, which gave a bandpass of 40 nm at 500 nm wavelength.

The room temperature PL spectra of the p^{++} (95-44), p^+ (95-30), p^- (95-35), i (95-36), and n^+ (95-37) doped layers are shown in Figure 4.3. Only the boron-doped films yielded detectable red-orange luminescence. The blue components to the PL spectra from these films seem to be real (from the porous silicon), though we cannot rule out the possible presence of organic contaminants from the etching that could be the source of this light. Also evident in these spectra are weak peaks at ~ 1.9 eV and ~ 2.2 eV that seem to increase in intensity with boron concentration. The ~ 1.6 eV peak, however, does not appear to have a strong correlation with boron concentration. The 83 K PL spectra of the p^{++} , p^+ , p^- , and i layers in Figure 4.4 illustrate that the intrinsic porous a-Si:H film does indeed have

a very weak red-orange component at low temperature as the non-zero background level from this sample is due to PL from the sample. This film probably has some residual boron contamination from the previous p-type deposition run. We note that the luminescence peak energy shifts to higher energies as the boron concentration increases. The n-type sample had no significant photoluminescence at 83 K. We also attempted to etch the n-type sample in 1% aqueous HF as did Lazarouk *et al.*; however, the resulting surface showed no signs of visible PL.

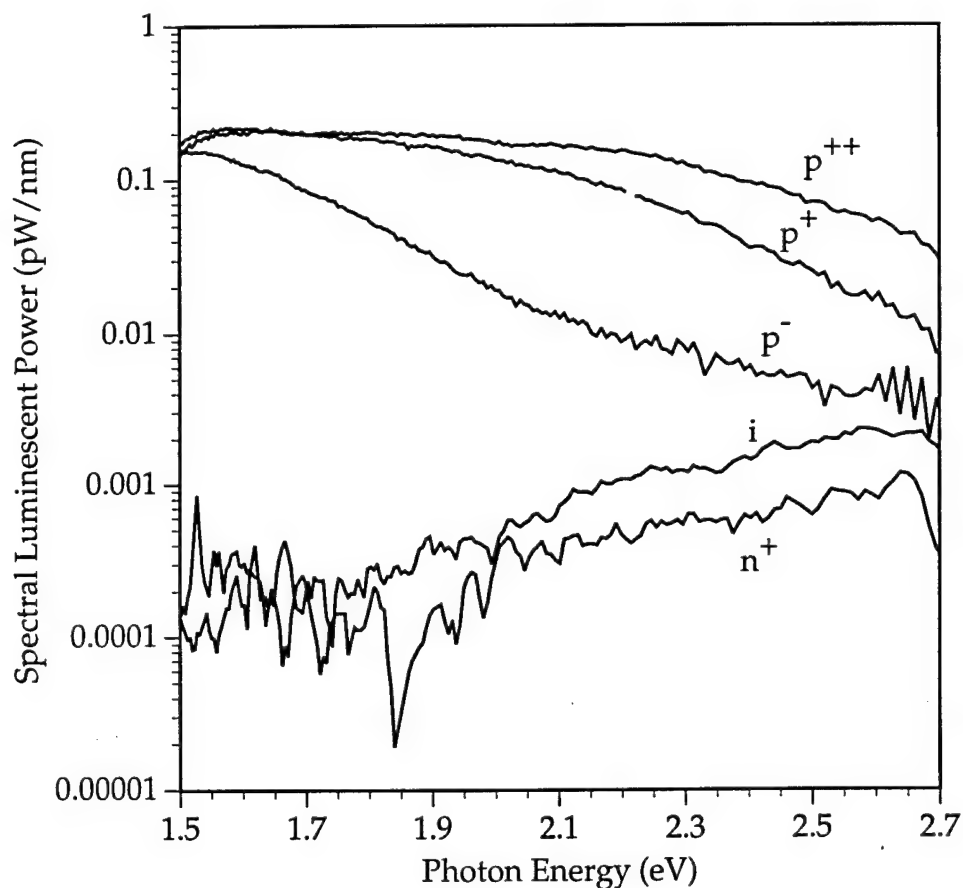


Figure 4.3. Room temperature porous a-Si:H PL versus doping.

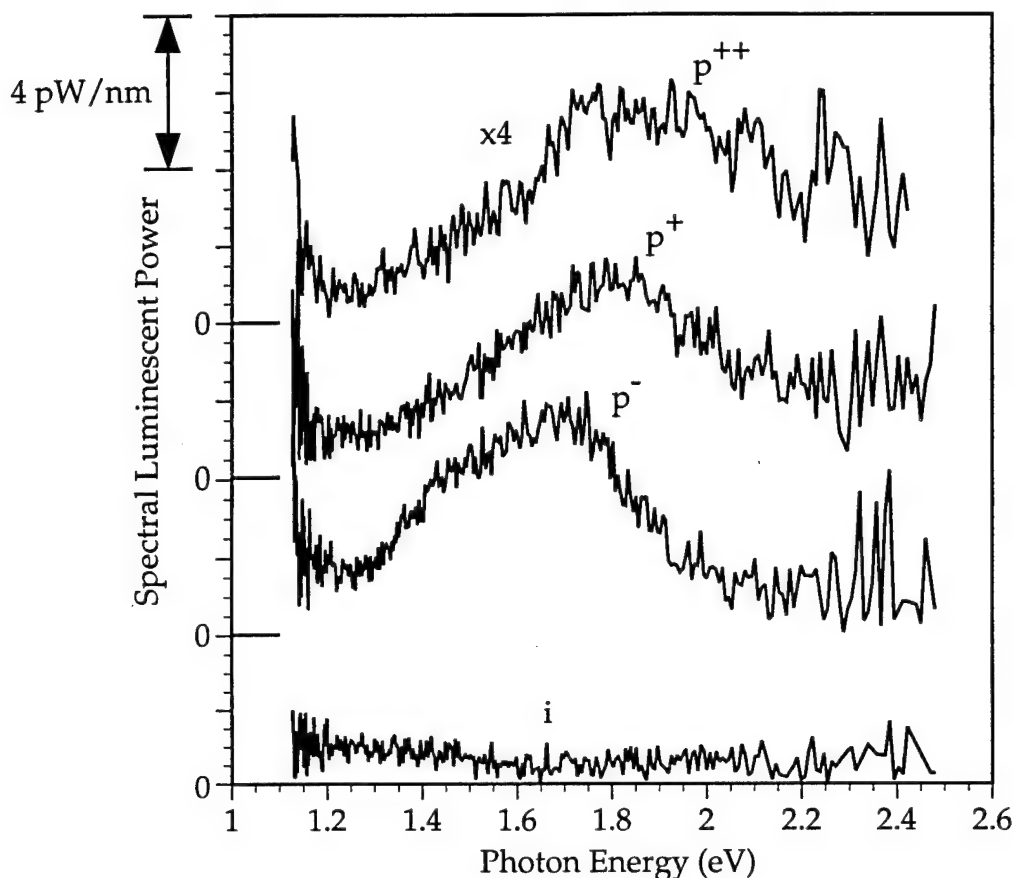


Figure 4.4. 83 K PL spectra of doped porous a-Si:H layers showing the effect of boron concentration. The n^+ sample did not exhibit any detectable PL at low temperature. The curves have been displaced along the y-axis for clarity.

2. Temperature Dependence

The temperature dependent photoluminescence of a p^+ sample etched at 1 mA/cm^2 in 25% HF, shown in Figure 4.5, reveals some remarkable structure that appears in the intermediate temperature range between 100-175 K. These are not interference fringes, as they change dramatically with temperature, but rather seem to indicate the presence of multiple radiative processes with strong temperature dependencies. Assuming that quantum confinement effects are not present in the amorphous nanostructures, this data would seem to be the strongest

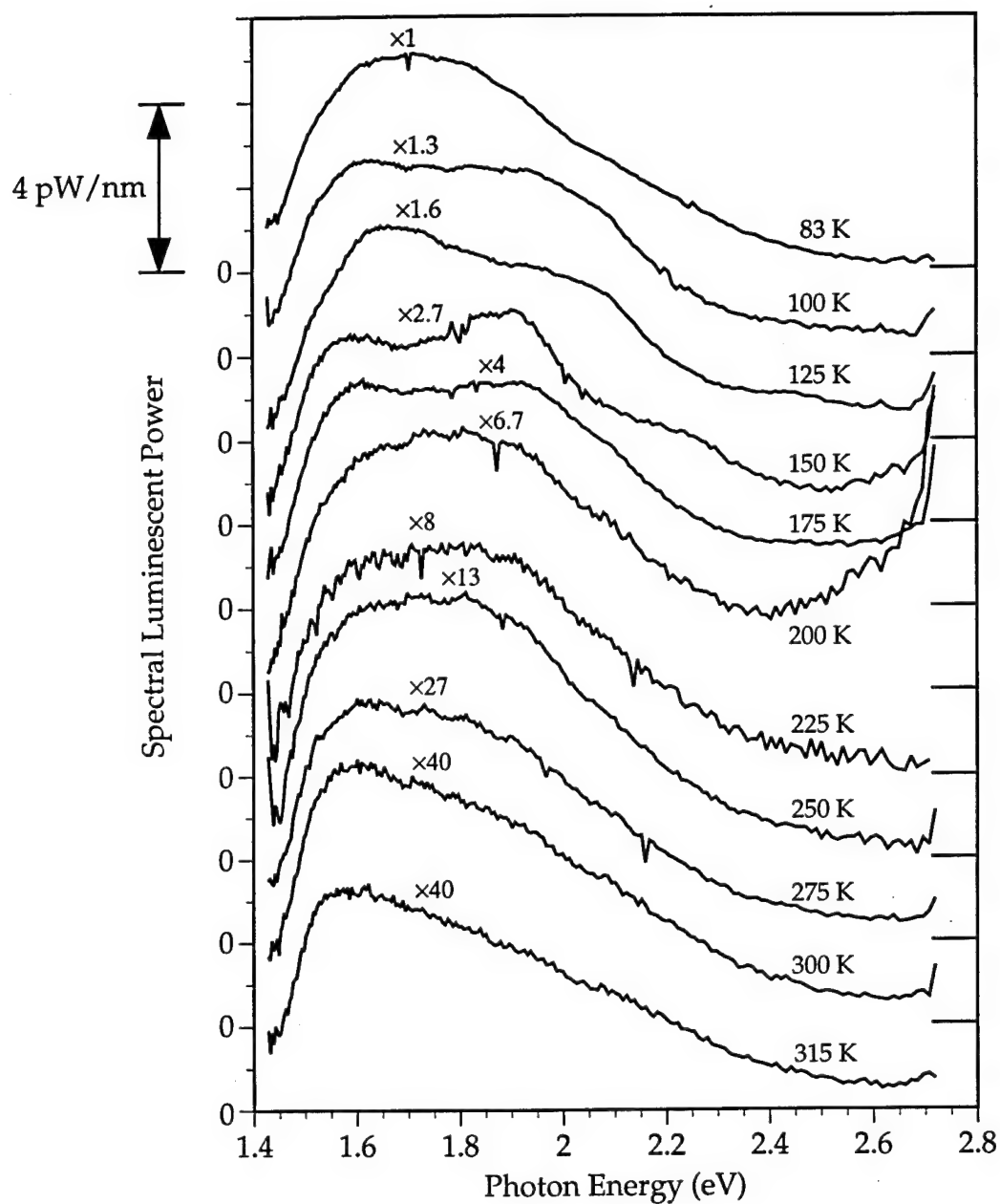


Figure 4.5. Temperature dependent PL of a p^+ porous a-Si:H etched at 1 mA/cm^2 for 15 min in 25% HF. The curves have been displaced as indicated for clarity. The structure in the 100-175 K PL spectra may be indicative of defect or impurity level transitions.

indication of defect or impurity related radiative transitions. The blue emission between 150-200 K also appears to be real, though it seems odd that it would disappear so dramatically between 200-225 K. The rapid falloff in PL between 1.4-1.5 eV in these spectra is not real; it is due to poor normalization of the PMT detector signal at the edge of the detector response.

As Figure 4.5 indicates, the PL intensity drops by roughly a factor of 40 between 83 K and room temperature. The 1.3-1.4 eV luminescence in undoped a-Si:H, on the other hand, decreases by more than 1000 times in the same temperature range (Collins, 1980). Although the structure in the PL complicates the issue, the overall trend appears to be a redshift with increasing temperature.

3. Etching Dependence

In porous crystalline silicon, the trend of increasing luminescence energy with increasing porosity is fairly well established. Higher porosity films may be produced by increasing etching current density and by decreasing etchant HF concentration. This correlation suggests, at least indirectly, a size dependence of the PL. In porous a-Si:H, we see no such trend in the PL.

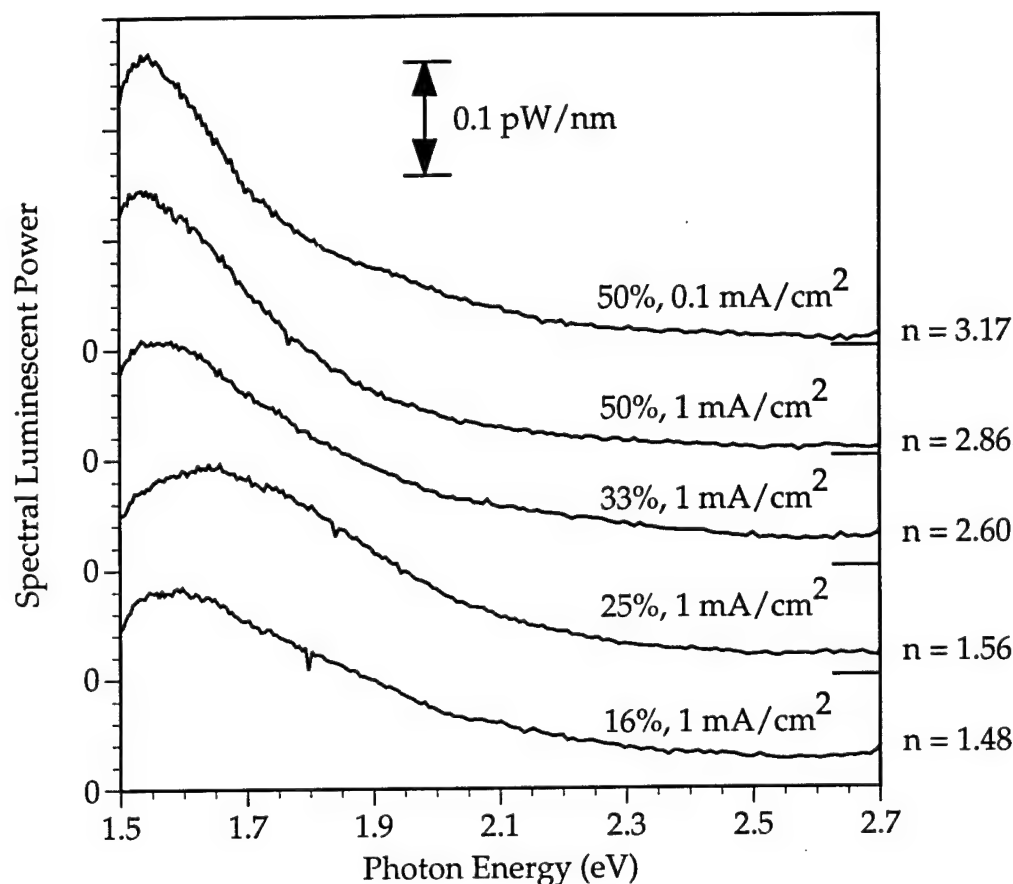


Figure 4.6. Room temperature PL spectra showing the effect of etchant HF concentration on porosity and PL. In contrast to porous c-Si, no correlation appears to exist between PL energy and porosity. The numbers on the right hand side of the graph indicate the measured refractive index of the porous layer. These data are from p^+ porous a-Si:H samples etched as indicated above each curve.

Figure 4.6 shows the room temperature PL spectra of five p^+ porous layers as a function of HF concentration. The effective indices of refraction for the top porous layers were measured with an ellipsometer at 632 nm wavelength and are given next to each curve. The effective index of refraction is an indication of layer porosity through the effective medium treatment (von Behren, 1995). Thus, while decreasing HF concentration does indeed produce layers of increasing porosity in a-Si:H, this effect does not bring about a shift in peak luminescence energy. The high energy PL

tail, however, does appear to increase very slightly with porosity. Why the peak energy of the sample etched in 25% HF is at a higher energy (~ 1.65 eV) than in all the other spectra is still a mystery. In Figure 4.7, the spectra of three samples etched at current densities ranging from $0.316 - 31.6 \text{ mA/cm}^2$ clearly shows that current density has little effect on porosity and no effect on PL.

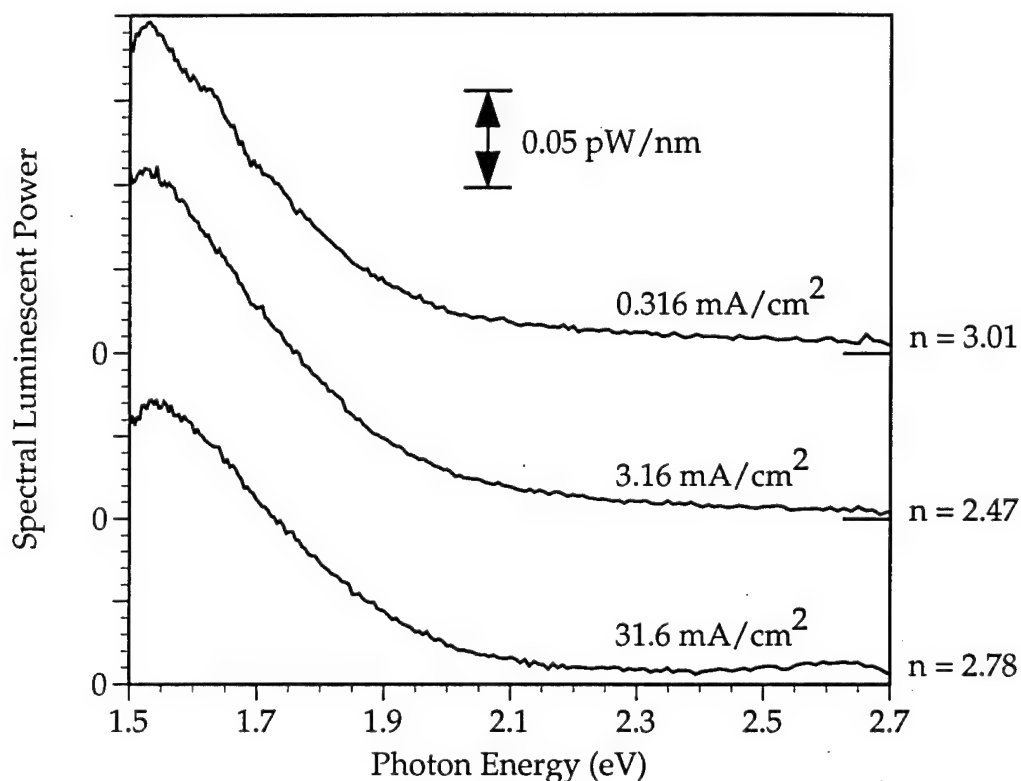


Figure 4.7. Room temperature PL spectra showing the effect of etching current density on layer porosity and PL. The graph shows that etching current, over two orders of magnitude, does not affect PL. The numbers on the right hand side are the effective indices of refraction for the porous layers, which were formed on p^- samples in 25% HF.

For comparison, Figure 4.8 illustrates the identical effect to that in Figure 4.6 for porous a-Si:H films on ITO substrates etched at 1 mA/cm^2 for 15 min in the etchants indicated. The measured absorbance of these

four samples is compared with that for the unetched film in Figure 4.9. An unusual absorbance bump at ~ 1.6 eV can be seen in the 50% and 33% HF curves. We suspect that this absorption is due to boron related defects, but why it appears enhanced in the etched films is a mystery.

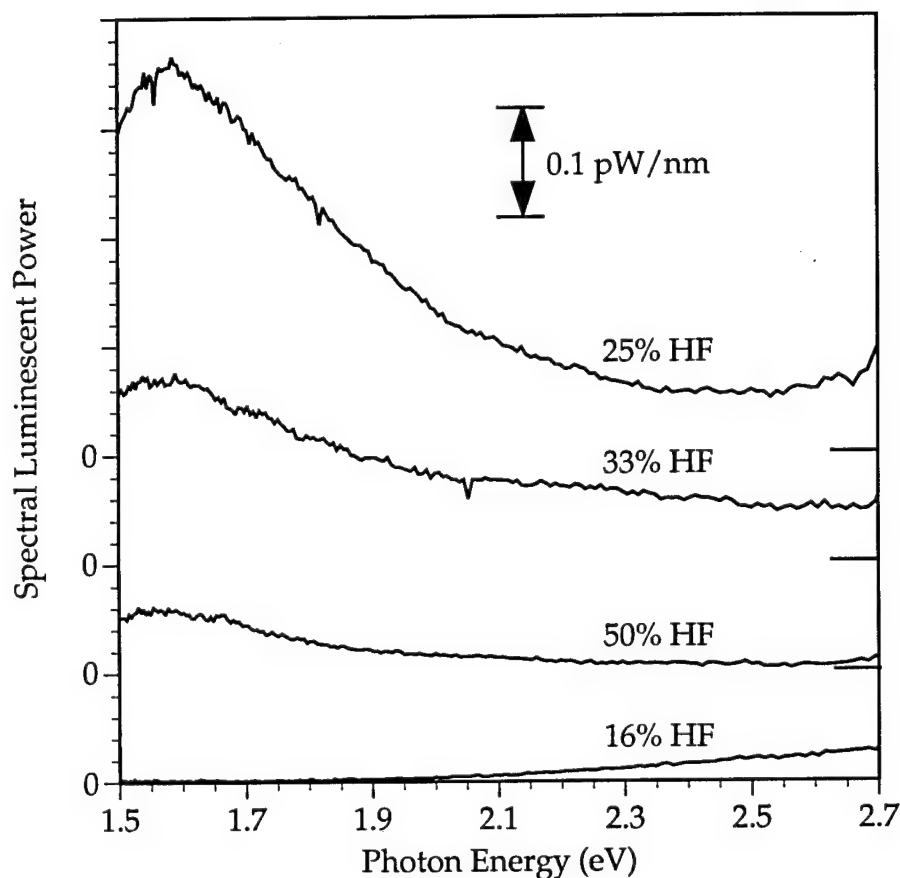


Figure 4.8. Room temperature PL spectra of p^+ porous a-Si:H layers on ITO/glass substrates. The data is similar to that in Figure 4.6 except for substrate type. These curves clearly show that the PL emanates from the porous a-Si:H.

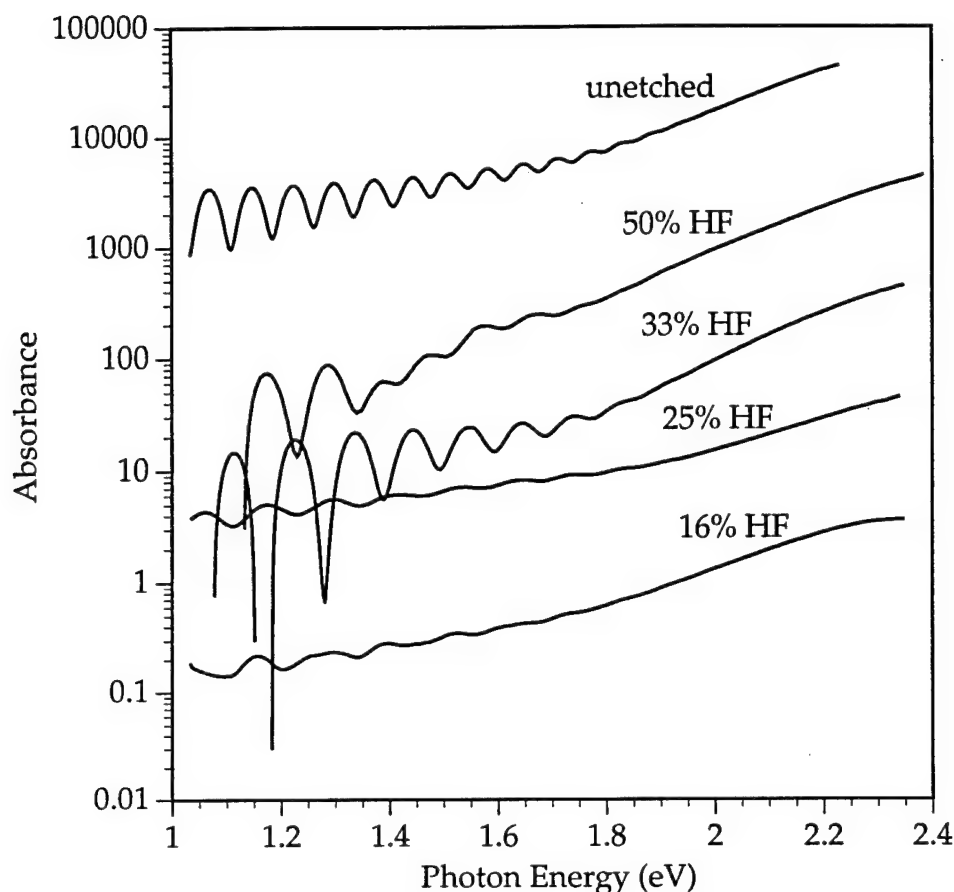


Figure 4.9. Comparison of the absorbance of the porous a-Si:H layers of Figure 4.8 with that of the unetched p^+ a-Si:H. The curves have been displaced along the log-y axis by multiplying successive traces by factors of 10.

4. a-Si:C:H Alloys

As discussed in the introduction, we produced a series of p^+ a-Si:C:H films with bandgaps ranging from 1.75-2.25 eV. Table 4.2 lists the deposition parameters, Tauc bandgaps, and conductivities of films in this series. An unfortunate side effect of increased carbon content was a rapid decrease in conductivity due to defect pinning of the a-Si:C:H Fermi level near midgap. Thus, the wider bandgap a-Si:C:H films were more difficult to anodize than the lower carbon content films as etching became very sensitive to pinholes in the high resistivity films.

Table 2: Deposition parameters, bandgaps, and conductivities of the series of doped a-Si:C:H films used in this study. The columns under gas flows are for the atomic flows of the active atoms in the deposition gases used: silane (Si), methane (C), and 1% trimethylboron in helium (B).

Film	Type	Flows (sccm)			Pressure (mT)	RF Power Density (W/cm ²)	Tauc Bandgap (eV)	Conductivity ($\Omega^{-1}\text{cm}^{-1}$)
		Si	C	B				
95-30	p ⁺	30	0	0.3	500	0.016	1.75	2.1×10^{-5}
95-43	p ⁺	8	12	16	300	0.016	1.90	1.3×10^{-6}
95-42	p ⁺	8	24	16	300	0.016	2.00	6.5×10^{-8}
95-41	p ⁺	8	40	16	300	0.016	2.13	2.9×10^{-9}
95-40	p ⁺	5	40	5	300	0.024	2.25	3.5×10^{-10}

Figure 4.10 shows room temperature PL spectra of a series of porous a-Si:C:H layers etched at 1 mA/cm² in 50% aqueous HF. This etchant gave the best porous layers for the wider bandgap films. The structure in the films may be due in part to interference fringes, but given the results of the temperature dependent measurements of Figure 4.5 and the coincidence of some peak energies in different samples we suspect that it may again indicate the presence of discrete energy levels in the radiative process. While this structure makes quantitative comparison of peak PL energies difficult to compare, it is apparent from the graph that the average PL energy increases with bandgap of the starting material. The width of the PL spectra also appears to increase with increasing carbon content, perhaps indication of greater disorder within the wide bandgap a-Si:C:H. Quantitative comparison of PL shift with bandgap is easier to see with low temperature PL spectra, shown in Figure 4.11. Here, the 83 K spectra of three films etched at 1 mA/cm² in 25% ethanoic HF clearly show PL peaks at approximately 1.7, 1.9, and 2.1 eV. The corresponding Tauc bandgaps of

these films are 1.75, 1.90, and 2.0 eV. Thus, we see a fairly clear correlation between bandgap and luminescence energy.

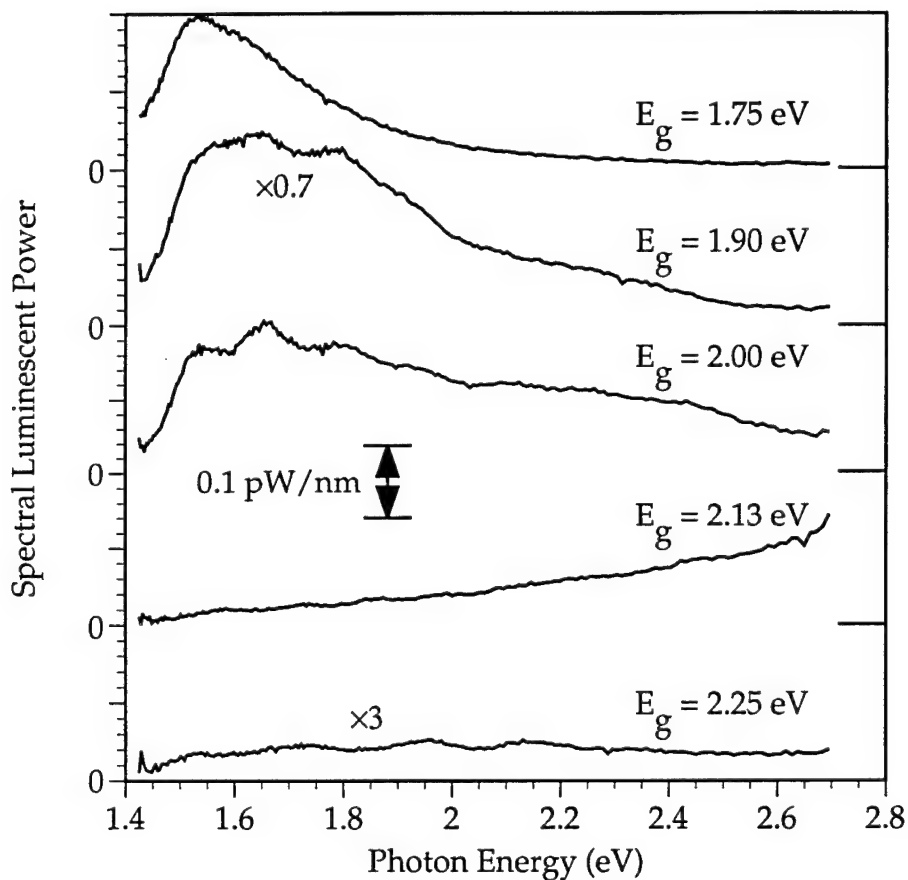


Figure 4.10. Room temperature PL spectra of porous a-Si:C:H layers as a function of C concentration. The samples were etched at 1 mA/cm² in 50% aqueous HF. The Tauc bandgaps are listed above each curve. The data indicate a trend of increasing PL energy with increasing bandgap energy.

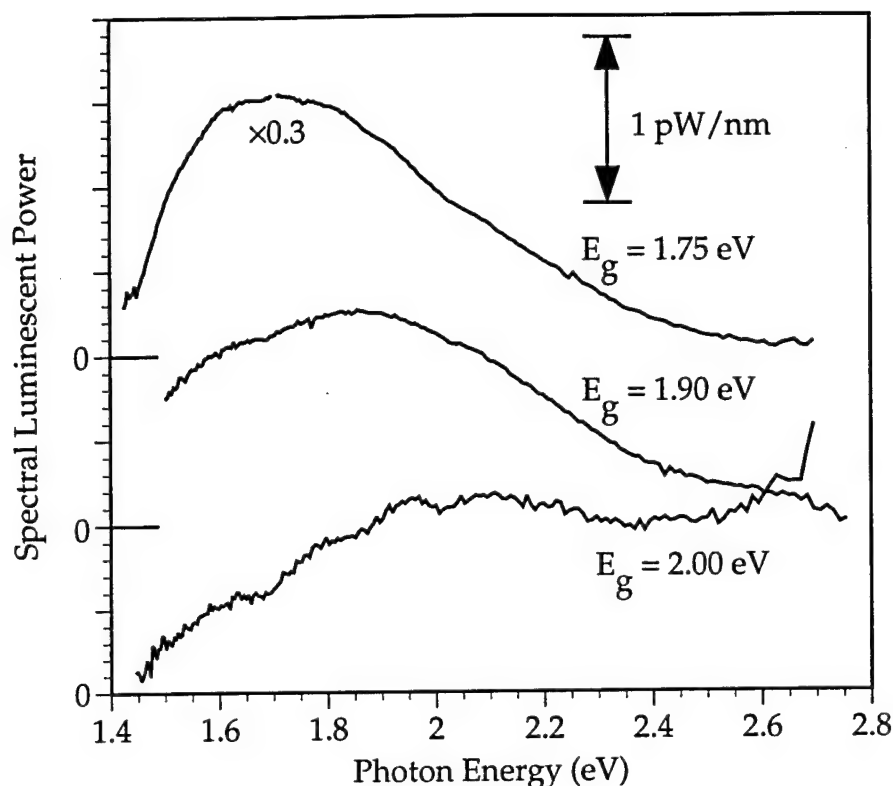


Figure 4.11. 83 K PL spectra of porous a-Si:C:H films etched at 1 mA/cm² in 25% HF. The Tauc bandgaps are given by each spectrum. The graphs shows a very definite correlation between bandgap and PL peak energy.

5. Post Treatments and Aging

In the cases of porous crystalline silicon (Vial, 1992) and porous amorphous silicon (Bustarret, 1992b) previously reported, post electro-oxidation of the porous layer resulted in a significant increase of the PL intensity. For our porous a-Si:H films, however, anodic oxidation in 0.1 M KNO₃ at 1 mA/cm² caused a decrease in intensity and a blueshift of PL energy, as shown in Figure 4.12 for the #95-44 p⁺ sample. Oxidation for too long a time resulted in crazing and lift-off of the porous layer. Figure 4.12 also illustrates the effects of exposure to ambient atmosphere for the electro-oxidized and unoxidized samples, where the PL for the freshly

etched and 1 day old samples are shown. Air exposure did not seem to degrade and broaden the PL of the more lightly boron-doped films (#95-30 and #95-35) nearly as much as it did for #95-44 in Figure 4.12.

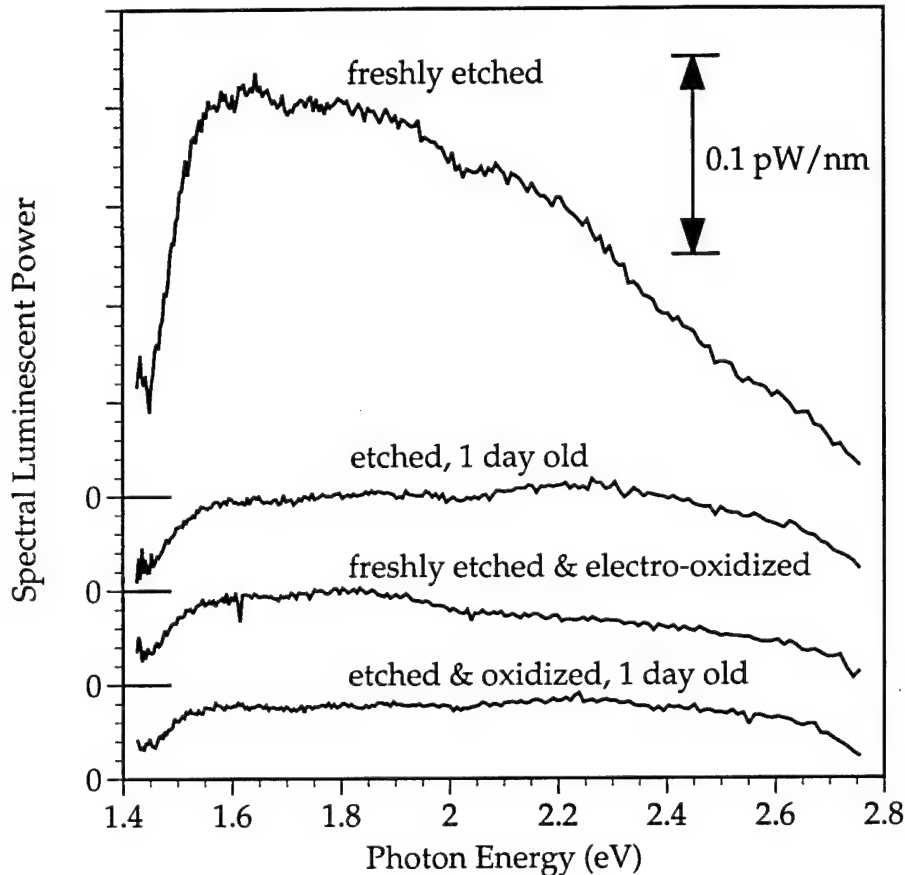


Figure 4.12. Room temperature PL showing aging effects on anodized p^{++} porous layers. The films were etched at 1 mA/cm^2 in 50% HF for 15 min. The electro-oxidized film was subsequently anodized in 0.1 M KNO_3 for 60 sec. The sample type and age of the sample at the time the PL was taken are indicated on the graph.

To test the effects of thermal annealing on luminescent porous a-Si:H films, we annealed a p^+ porous sample (1 mA/cm^2 , 25% HF, 15 min) at 800°C for 1 hour in forming gas (4% H_2 in N_2). Figure 4.13 compares the resulting PL from the annealed and unannealed samples. Surprisingly, there is still some weak red light from the annealed sample,

which is 0.05 eV or more red-shifted and 20 times weaker than the freshly etched sample. Although 800°C for 1 hour is certainly enough time/temperature to crystallize the unetched a-Si:H film, it is not clear if this would cause crystallization of the nanometer-sized structures in the porous layer. Previous studies indicate that higher temperatures and longer annealing times are required to crystallize very thin a-Si:H films. We suspect that nearly all the hydrogen is driven out of the film by the anneal, although some residual hydrogen may remain due to the forming gas environment. The continued presence of visible luminescence after this anneal suggests that hydrogen is not necessary for visible PL -- neither as a passivating agent nor as a component in a luminescent surface compound.

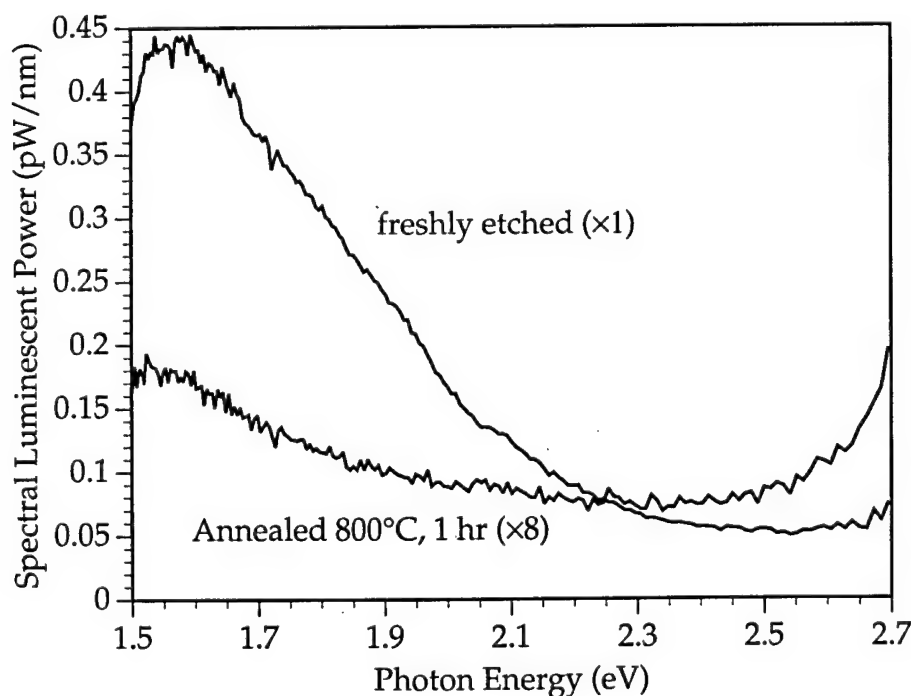


Figure 4.13. Effect of 800°C anneal for 1 hour in forming gas on the room temperature PL from p^+ porous a-Si:H anodized at 1 mA/cm² for 15 min in 25% ethanoic HF. Some visible PL still remains after the anneal indicating that hydrogen probably is not necessary for light emission.

6. a-Si:H Films Deposited onto Porous a-SiO₂ Substrates

One difficulty in interpreting the results of experiments on etched porous silicon layers is the uncertainty in the effects of the etch. For instance, one might easily imagine that the internal surfaces of the porous silicon change chemically to form luminescent species or that, as discussed in Chapter VI, luminescent silicon compounds are redeposited out of a saturated etchant solution. As a final experiment to test for a size dependence of porous silicon luminescence, we deposited a thin layer of undoped a-Si:H onto a completely oxidized porous silicon substrate. Since the chemical vapor deposition tends to coat all surfaces regardless of orientation, we expect that the a-Si:H deposited to a shallow depth into the non-luminescent porous silicon dioxide matrix resulting in a sort of inverted porous a-Si:H layer with quasi-one-dimensional a-Si:H structures on the bottom side of the deposited film. We assume that the feature size of the oxidized porous silicon substrate surface is comparable to, or smaller than, the thickness of the a-Si:H layer.

The porous silicon was produced on very lightly doped, unpolished, n-type silicon wafer using a chemical stain etch of HF:H₂SO₄:NaNO₂:H₂O. (Kelly, 1994) This porous layer was then completely oxidized at 1100°C until the photoluminescence disappeared. A thickness of 100 Å of a-Si:H was then plasma deposited onto the oxidized porous layer as well as 7059 glass at a substrate temperature of 210°C, an RF power density of 16 mW/cm², a chamber pressure of 500 mT, and a SiH₄ gas flow rate of 40 sccm.

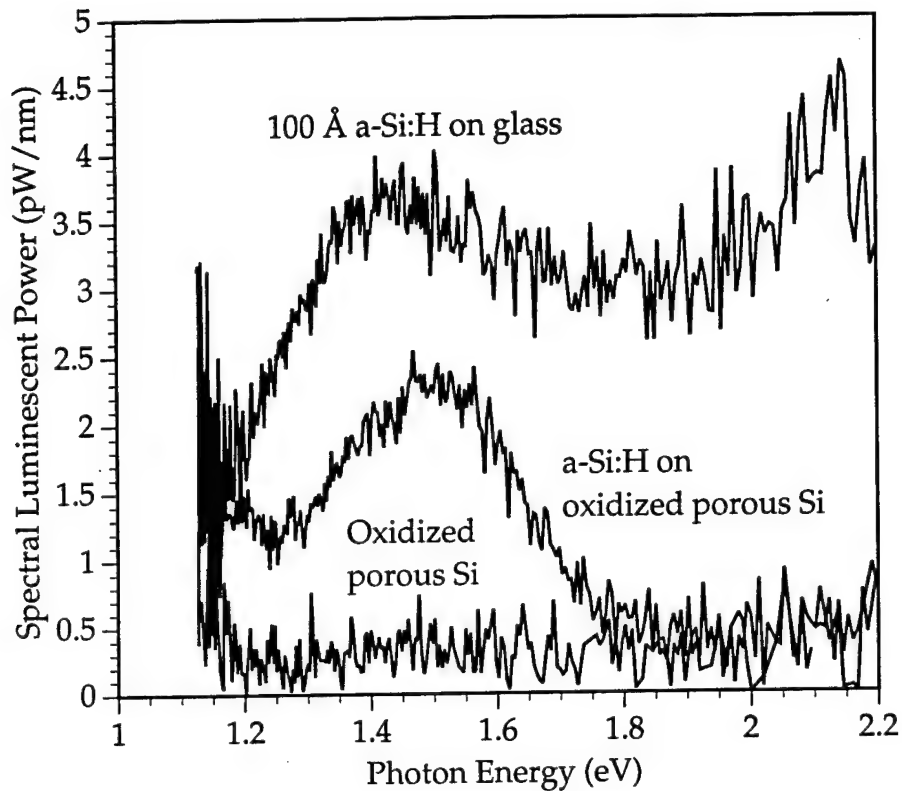


Figure 4.14. 83 K PL of a 100 Å thick undoped a-Si:H layer on glass and oxidized porous silicon substrates. The slight blueshift in the PL peak of the sample on oxidized porous silicon gives some indication of a size dependence of the a-Si:H luminescence. For comparison, the bottom trace shows the PL from the oxidized porous silicon without the a-Si:H layer.

The room temperature PL was very weak and difficult to detect, so in Figure 4.14 we compare the 83 K PL spectra of the a-Si:H on porous SiO₂, the a-Si:H on 7059 glass (smooth film), and the back side of the porous SiO₂ substrate without a-Si:H. Photoluminescence was excited by the 488 nm light from an Ar⁺ laser. The blue PL from the sample on glass originates from the 7059 glass (observed without a-Si:H), as only ~90% of the incident 488 nm light is absorbed in the a-Si:H layer. Although small, there does appear to be a slight blueshift from ~1.45 eV to ~1.50 eV between the 100 Å thick film on glass and the film on porous SiO₂. We

also note a slight ~ 1.15 eV or lower energy peak in the a-Si:H on porous SiO₂ sample, which could be related to oxygen defects in a-Si:H.(Street, 1981)

C. Discussion

From our the results, we see mixed evidence for a size-dependent luminescence from porous a-Si:H. While we were able to produce porous layers of differing porosities by varying etch conditions, the photoluminescence spectra of the resulting samples remained nearly constant, with a room temperature PL peak energy of ~ 1.6 eV. These data are not conclusive, however, as no connection has been established between porosity and nanostructure size in porous a-Si:H. One might easily imagine a situation in which the size of the remaining amorphous silicon skeleton is self-limited and therefore independent of etching conditions. The 83 K PL spectra of p⁺ vs. p⁻ vs. i type porous layers of Figure 4.4 show a significant peak shift as a function of boron concentration, which may be an indication of different feature sizes due to etching differences. Bustarret *et al.* have suggested that feature size in porous a-Si:H may be determined by available percolation paths in the a-Si:H (Bustarret, 1992b). If so, it may be conceivable that a higher boron concentration results in a higher density of percolation paths and consequently smaller nanostructures in porous a-Si:H. More effort is required to clarify this issue further. The very slight ~ 0.05 eV blue shift in the low temperature PL from the a-Si:H on porous SiO₂ sample (Figure 4.14) may give evidence of a size dependence, but more data is needed to confirm this trend as well.

The observation of efficient room temperature PL in annealed amorphous silicon oxynitride films (Augustine, 1995a; Augustine, 1995b) coupled with observations of the strongest PL in the primarily amorphous top $\sim 1\text{-}2\text{ }\mu\text{m}$ layer of porous c-Si (Noguchi, 1992; Prokes, 1992) may suggest that visible light emission is due to an alloying effect of amorphous silicon with oxygen, nitrogen, and/or hydrogen. This effect may be difficult to discern from size-dependent luminescence in spatially confined a-Si:H. As the freshly etched porous a-Si:H oxidizes upon exposure to air, the resulting a-Si/a-SiO₂ interfaces are probably not atomically smooth. We should expect at least some transition layer of a-SiO_x between the two (Himpsel, 1988) as well as some diffusion of stray O atoms into the a-Si interior. Thus, for small enough a-Si nanostructures, the resulting oxidized material may be more of a porous network of homogeneous a-Si:O alloy than a porous network composed of confined a-Si cores with passivating a-SiO₂ surfaces.

Comparison of the PL spectra of the porous a-Si:H films with those predicted by the confined amorphous silicon model of Chapter III shows some similar features as well as some differences. The predicted PL from a distribution of a-Si:H structure sizes (see Figure 3.11) shows a broad peak centered at $\sim 1.55\text{-}1.65\text{ eV}$ with a long high energy tail. Indeed, the room temperature spectra from porous a-Si:H also exhibit these basic features. The appearance of highly temperature-dependent structure in the measured PL spectra, however, seems to indicate the presence of discrete levels in the radiative transition. This type of structure is at odds with the broad, featureless luminescence predicted by the model and seen in "bulk" a-Si:H (Street, 1984), a-Si:O_x:N_y:H (Augustine, 1995b), and porous

crystalline silicon. Instead, it may be evidence of luminescence from defect centers or impurity levels. The aging data of Figure 4.12 also suggest that perhaps several processes are occurring in porous a-Si:H as oxidation strongly reduces the 1.6 eV peak while it only slightly reduces the ~2.2-2.3 eV luminescence.

At this point, we can draw several conclusions regarding the stoichiometry of these samples. First, addition of carbon to the a-Si:H films results in both an increase in bandgap of the unetched film and an increase in PL energy of the porous film. This finding suggests that band states of the remaining amorphous material are involved in the radiative transition; however, we cannot completely rule out the possibility that the differences in PL are the result of etching differences, which may cause variations of structure size or surface chemistry. Second, we see a correlation with the presence of boron and the observation of visible PL. If we account for the difference in absorption of 365 nm excitation light, the p^+ films, which contain approximately 10-20 times more boron but are approximately one tenth the thickness of the p^- films, would have roughly 10 times greater quantum efficiency than the p^- films (assuming that the absorption coefficient of the porous layers was small). Moreover, higher boron concentrations appear to yield porous films with increased PL intensity in a broad range of visible energies centered at ~2.2 eV. It would be worthwhile investigating the correlation of this peak with various boron compounds such as B_2O_3 and to see if such emission exists in borosilicate glasses. Finally, the 1.6 eV PL is still present after annealing at 800°C for 1 hour. While some structural relaxation should occur at this temperature, possibly even crystallization, the major effect would be

evolution of nearly all hydrogen from the film. Therefore, we conclude that hydrogen, while perhaps providing partial passivation of defects, is not necessary for the red luminescence.

For porous crystalline silicon, it is often suggested that quantum confinement in silicon nanocrystals provides carriers with sufficient energy to populate high energy surface tail states (Koch, 1993) or luminescence centers (Lin, 1994). In porous amorphous silicon, we do not expect quantum confinement effects, and therefore carrier injection into high energy radiative states must result from another mechanism. Assuming that photocarriers are created in the internal amorphous silicon nanostructures, then possible carrier injection paths may be through hot carrier tunneling into surface radiative states or through the effective bandgap widening discussed in Chapter III. A third possibility is that photocarriers are generated by optical absorption in a separate luminescent material, which is not a-Si.

As a final point for discussion, we compare our results with those reported earlier by Bustarret *et al.* (Bustarret, 1992b) and Lazarouk *et al.* (Lazarouk, 1994). The main differences between the properties of our porous a-Si:B:H films and those of Bustarret *et al.* appear to be the low quantum efficiencies of our samples and the structure that we observe in many of the PL spectra. Since our etching techniques are sufficiently similar, it would seem that these differences originate from either the stoichiometry or the morphology of the starting a-Si:B:H material, which would not be surprising given the differences in growth conditions. Under conditions of low SiH₄ concentration, high plasma power density, and low substrate temperature, columnar growth has been observed in

glow discharge a-Si:H films (Knights, 1980). This film morphology would certainly etch much differently than a more homogeneous layer. Unfortunately, without a side-by-side comparison of starting a-Si:H films, it is difficult to postulate what differences exist. In reference to the phosphorous-doped n-type films of Lazarouk *et al.*, we were not able to obtain porous layers or visible photoluminescence from similarly anodized n^+ doped films.

D. Conclusions

We have observed room temperature red-orange light emission from anodized porous a-Si:H films, clearly demonstrating that crystallinity is not a requirement for light emission. Luminescent porous layers were produced over a range of boron doping concentrations. No red emission was observed from phosphorous-doped n-type a-Si:H films. The nominally 1.6 eV room temperature peak energy was not affected by variations in layer porosity induced by changing etchant HF concentration or etching current density, though PL from undoped a-Si:H deposited onto porous SiO₂ substrates is consistent with a size dependence of the low temperature PL. Temperature-dependent PL from anodized p^+ a-Si:H shows considerable structure in the spectra, which is consistent with discrete defect or impurity states playing a role in the radiative process. Investigation of PL energy versus bandgap energy of porous p-type a-Si:C:H films revealed a close correlation between the two, which is consistent with band states being involved in the luminescence. Finally, from PL results after annealing at 800°C, we infer that hydrogen is not necessary for the visible PL from porous a-Si:H.

CHAPTER V

ELECTROABSORPTION MEASUREMENTS OF POROUS SILICON

A. Introduction

A principal missing link in our understanding of porous silicon is knowledge of what the bandgap energy, or range of energies, is of silicon nanocrystals in the material. If we could accurately measure porous silicon bandgaps, we could compare these energies with observed luminescence energies and immediately decide if the radiative transition originates from extended band states, from sub-bandgap localized states, or from super-bandgap localized states. With this information, one would resolve many of the mysteries of porous silicon. In particular, we want to know if silicon nanocrystals exhibit quantum confinement effects, and if so, are these effects involved in the luminescence transition. Unfortunately, optical absorption measurements of porous silicon are not sufficient to determine the porous silicon bandgap. The absorption edge in porous silicon tends to be shallow, as shown later, and the

inhomogeneous mix of amorphous and crystalline material in the porous structure tends to spread out the absorption features even further.

One method that has been used to successfully locate the band edge in amorphous semiconductors, where ambiguities also exist in determining the bandgap, is electroabsorption. An electric field applied across a semiconductor changes its absorption coefficient slightly. Since the change in absorption is greatest near the semiconductor band edge, the electroabsorption signal peaks at that energy. By measuring electroabsorption of porous silicon, we should therefore observe a large change in absorption over the range of bandgap energies of silicon crystallites in the material. If the luminescence transition is from extended states in quantum confined silicon crystallites, then we should observe an overlap of the photoluminescence and electroabsorption peaks. If, on the other hand, the luminescence is from localized states, then we should not expect to see overlapping photoluminescence and electroabsorption peak energies.

In this chapter, I discuss our* electroabsorption measurements of porous silicon. To provide a little background, I first review some of the electro-optic effects in silicon that lead to electroabsorption. In the following section, I then discuss the results of our measurements. Electroabsorption signals from porous silicon are quite measureable, but a

*I give special thanks to Melanie Fewings and Lee Hirsch, undergraduate researchers, who helped with the electroabsorption measurements and sample preparation.

number of complications must be overcome to fully understand the results of the measurement. I show data from several porous layers that give evidence of quantum confined states in porous silicon. In the final section of this chapter, I discuss possible implications of our electroabsorption results as well as ways to improve the experiment.

B. Electro-optic Effects in Silicon

Unlike direct band gap materials, such as gallium arsenide, which exhibit very sharp and strong absorption at the band edge, indirect gap crystalline silicon has relatively weak band edge absorption and hence weak band edge nonlinearities. Even a-Si:H with its quasi-direct bandgap shows only moderate electro-optic modulation at its nominally 1.7 eV band edge due to disorder-induced tail states (Weiser, 1988). In addition, both a-Si:H and c-Si are centrosymmetric materials so that there are no $\chi^{(2)}$ optical nonlinearities. Although the electro-optic properties of silicon are not great, several effects, which I discuss below, do contribute to measurable electroabsorption.

1. Franz-Keldysh Effect

Under an applied electric field, the bands in a crystalline semiconductor tilt, as shown in Figure 5.1, allowing carriers to tunnel some distance into the band gap. The spatial overlap of electron and hole wavefunctions near the band edges due to the applied field results in an exponential absorption tail below the band edge and an oscillatory absorption above the band edge. The exponential falloff of the carrier wavefunctions into the bandgap has a characteristic energy given by (Parikove, 1971)

$$\Delta E = \frac{3}{2} (m^*)^{-1/3} (q\hbar F)^{2/3}, \quad (5.1)$$

where m^* is the carrier effective mass, q is the elemental charge, \hbar is Planck's constant, and F is the applied electric field. This phenomenon is known as the Franz-Keldysh effect. The largest absorption change occurs for photon energies very near the band gap energy.

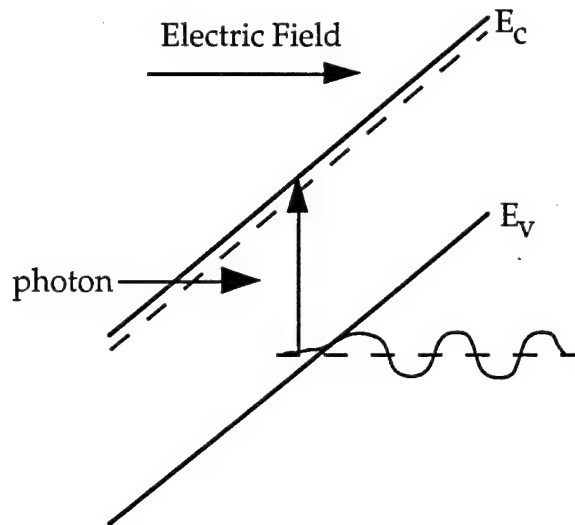


Figure 5.1. Diagram showing the concept of the Franz-Keldysh effect. Application of an electric field across a crystalline semiconductor results in tilted conduction (E_C) and valence (E_V) bands. Photon absorption below the crystalline band edge to conduction band states (solid line) or exciton states (dashed line) is possible due to carrier tunneling into the forbidden gap.

In Figure 5.2, I show the Franz-Keldysh-induced change in absorption coefficient, $\Delta\alpha$, near the indirect bandgap of crystalline silicon for two applied electric field regimes (Wendland, 1965). According to Wendland and Chester, the two electroabsorption peaks at 1.06 eV and 1.175 eV in the high field curve of Figure 5.2 are due to the tunneling-assisted optical transition from valence-band states to conduction-band states and involve TO phonon absorption and TO phonon emission

processes, respectively (Wendland, 1965). In the low field regime, the final state in the optical absorption is an exciton state. Although the theory of Franz-Keldysh electroabsorption at an indirect bandgap predicts a field dependence of $\Delta\alpha \propto F^{4/3}$ (Chester, 1965), the 1.175 eV $\Delta\alpha$ peak in the data of Wendland and Chester exhibits an $F^{2.18}$ field dependence. The source of this discrepancy is unknown. In a-Si:H, the Franz-Keldysh effect appears to be negligible (Weiser, 1988), perhaps due to localization of the carrier wavefunctions and to the presence of tail states in the bandgap. The dominant effect in a-Si:H appears to be the Kerr effect, which is discussed below.

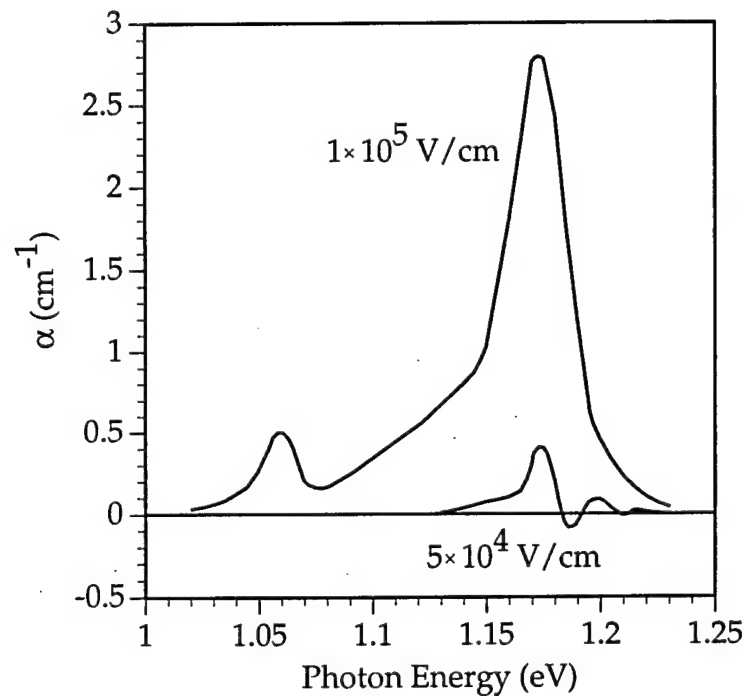


Figure 5.2. Electroabsorption spectra of crystalline silicon for two different applied electric fields (data from Wendland and Chester (Wendland, 1965)).

2. DC Kerr Effect

Our usual assumption that the polarization of a medium responds linearly with applied electric field leads to an index of refraction and absorption coefficient that are essentially independent of applied field strength. In reality, nonlinearities in the polarization response start to occur when the total electric field strength (optical field plus applied d.c. field) becomes large enough to noticeably distort the quadratic potential wells of the bound electrons. Thus, whereas the Franz-Keldysh effect is caused by extended wavefunctions, the Kerr effect is due to bound, or localized, wavefunctions (Butcher, 1990). In this case, the polarization of the medium may be modelled by a Taylor series expansion in electric field of the form

$$P = \epsilon_0 \cdot (\chi^{(1)}F + \chi^{(2)}F^2 + \chi^{(3)}F^3 + \chi^{(4)}F^4 \dots), \quad (5.2)$$

where P is the induced polarization, ϵ_0 is the electric permeability of vacuum, $\chi^{(i)}$ are the optical susceptibilities of the medium, and F is the total applied electric field (a.c. optical field plus d.c. applied field). For centrosymmetric media, such as silicon, all the even terms in Equation 5.2 drop out. Neglecting all but the first and third terms, the nonlinear, complex index of refraction ($\hat{n} = n + ik$) along the x-polarization direction is given by

$$\begin{aligned} \hat{n}_x &\approx \sqrt{1 + \hat{\chi}^{(1)} + \hat{\chi}^{(3)} |F_x^{dc}|^2} \\ &\approx n_0 + \frac{\hat{\chi}^{(3)} |F_x^{dc}|^2}{2n_0}, \end{aligned} \quad (5.3)$$

where $\hat{\chi}^{(1)}$ and $\hat{\chi}^{(3)}$ are the first order linear and third order nonlinear optical susceptibilities, respectively, n_0 is the zero-field index of refraction, and F_x^{dc} is the applied d.c. electric field along the x-direction. The change in refractive index (including the imaginary absorption term) is given by

$$\Delta\hat{n}_x \approx \hat{n}_0 + \frac{1}{2}\hat{\chi}^{(3)}|F_x^{dc}|^2, \quad (5.4)$$

where \hat{n}_0 is the complex index of refraction at zero applied field. This electro-optic effect is called the d.c. Kerr effect, and it is the dominant electric field effect in a-Si:H.

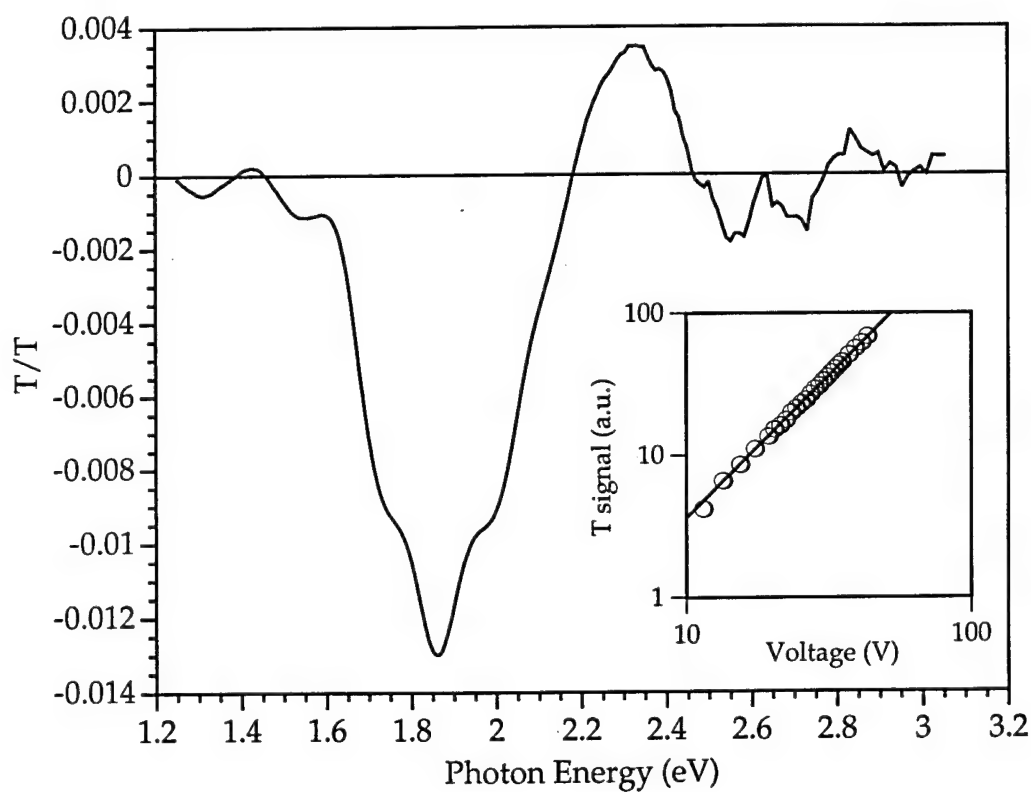


Figure 5.3. Measured electroabsorption spectrum of an a-Si:H/a-Si:C:H multilayer film showing the largest change in absorption near the nominally 1.9 eV bandgap. The quadratic voltage dependence of the electroabsorption, shown in the inset plot, suggests that the Kerr effect is responsible for the electro-optic response in amorphous silicon.

Figure 5.3 shows the measured electroabsorption spectrum ($\Delta\alpha$) of an a-Si:H/a-Si:C:H multilayer film, illustrating that resonant enhancement of the Kerr effect produces the strongest electro-optic effect near the nominally 1.9 eV band edge. The inset of Figure 5.3 shows the quadratic field dependence of $\Delta\alpha$. I show the measured electroabsorption from the multilayer film simply because I had the best data from this sample; single layer a-Si:H films showed very similar electroabsorption spectra peaking at ~1.7 eV and also having the quadratic voltage dependence. In crystalline silicon, the Kerr effect is generally masked by the larger Franz-Keldysh effect (Soref, 1987).

3. Free Carrier Absorption

The presence of free charge carriers in a semiconductor creates optical absorption at energies below the bandgap. This effect is reasonably well described by the Drude model of the optical properties of metals (Peyghambarian, 1993). The Drude model predicts a linear increase in the absorption coefficient with the density of free carriers, n_e , as

$$\alpha(\lambda) = \alpha_o(\lambda) + \frac{4\pi n_e q^2 \tau}{cm^* n(\lambda)}, \quad (5.5)$$

where q is the elemental charge, τ is the carrier relaxation time, c is the speed of light, m^* is the carrier effective mass, and $n(\lambda)$ is the index of refraction. Below the plasma frequency, optical excitation of free charges causes them to oscillate in phase with the optical field. The induced charge-displacement generates an internal field 180° out of phase with the optical wave and thereby cancels out this wave. This process explains why metals absorb visible light.

Because of its large internal surface area, we expect that porous silicon has a large density of carrier trapping states and consequently very few free carriers. Even for well passivated quantum structures, the expanded bandgap will result in very low intrinsic carrier concentrations. Thus, we do not anticipate observable free carrier absorption effects in porous silicon.

4. Electro-optic Effects in Quantum Size Structures

By sharpening the band edge transition, quantum confinement of carriers in a semiconductor enhances band edge nonlinearities. Application of an electric field across quantum-confined structures shifts the allowed eigenstates of the quantum well. If we neglect the Coulomb interaction of electrons and holes, the resulting electro-optic effect in crystalline semiconductors is the quantum-confined Franz-Keldysh effect (Miller, 1986). However, since quantum confinement increases the ionization energy of Wannier excitons in the semiconductor, which, therefore, can exist at much higher temperatures, we often cannot neglect the Coulomb interaction that leads to exciton formation (Peyghambarian, 1993). In this case, an applied electric field not only shifts the allowed energy levels of the quantum well, but it shifts the energy of the sharp excitonic absorption peak as well. This effect is known as the quantum confined Stark effect and may result in large optical modulation (Peyghambarian, 1993).

As a simple example of how quantum confinement may enhance electroabsorption, I show here a simulation of the electroabsorption we might expect from a slight shift in the peak absorption energy of a sharp

absorption line. For simplicity, I neglect the wave nature of electrons and holes. I also show how a distribution, in energy, of different absorbers might change the observed electroabsorption.

As we have seen, an applied electric field shifts the eigenstates in the quantum well. Particularly for 0-d quantum dots (spheres), where the density of states function becomes quite discrete, this shift in energy levels will result in a large electro-optic effect. Consider, for example, the sharp Gaussian-like absorption line in the transmission spectrum shown in the top graph of Figure 5.4. Let us assume that an applied electric field red-shifts this absorption to slightly lower energies. Neglecting changes in the wavefunction overlap caused by band bending, the electroabsorption spectrum from this single absorber is simply the difference between the two absorption spectra, as shown in the bottom graph of Figure 5.4. Now, if we consider a distribution of absorbers with different absorption energies, such as we might expect from a collection of different size silicon quantum dots, we see in Figure 5.5 that the net electroabsorption spectra is broadened by the distribution but retains the same derivative-like spectral shape. The fact that the low energy ΔT peak is negative and the high energy peak positive indicates that the electric field red-shifted the absorption edges.

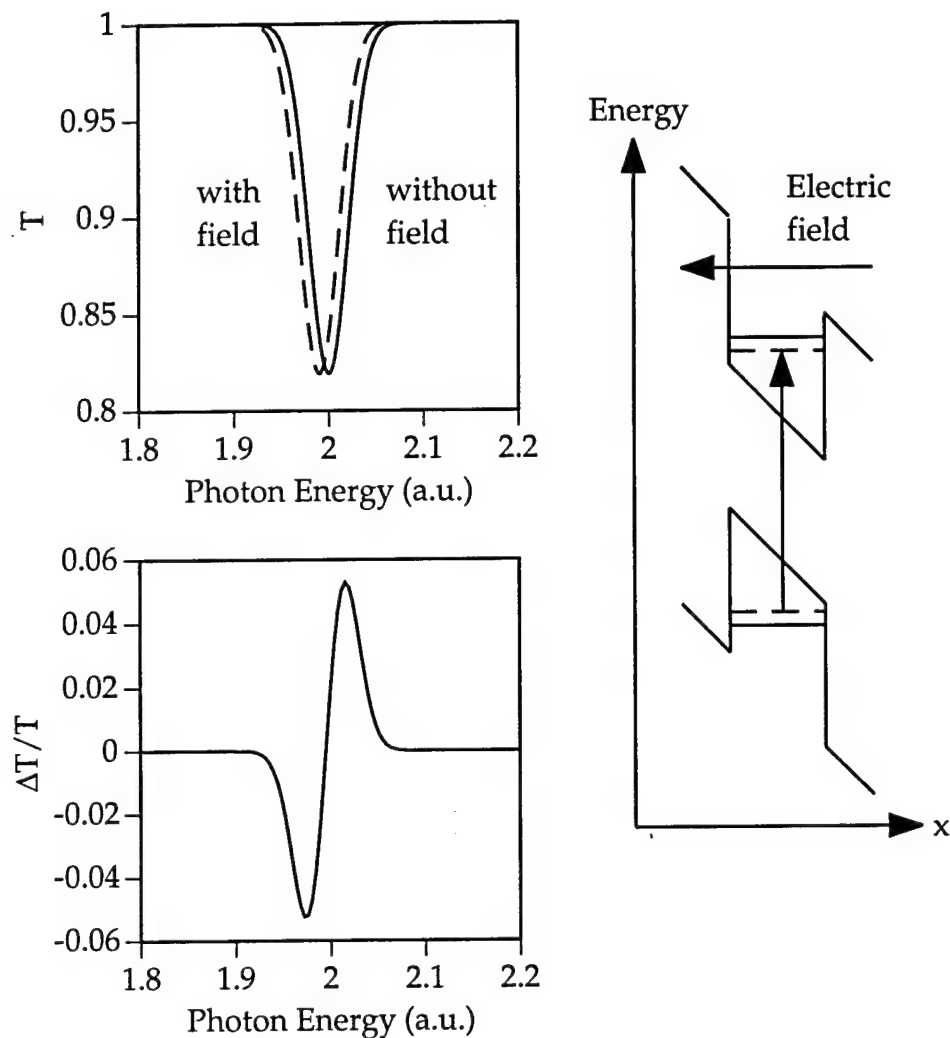


Figure 5.4. Simulation showing the effect of a slight redshift in a sharp absorption feature in the optical transmission (top graph) due to an applied electric field, as may arise in a quantum confined structure shown in the sketch at right. Under an electric field, the allowed energy levels shift down to the levels shown by the dashed lines. The resulting change in transmission from this single absorber is shown in the bottom graph.

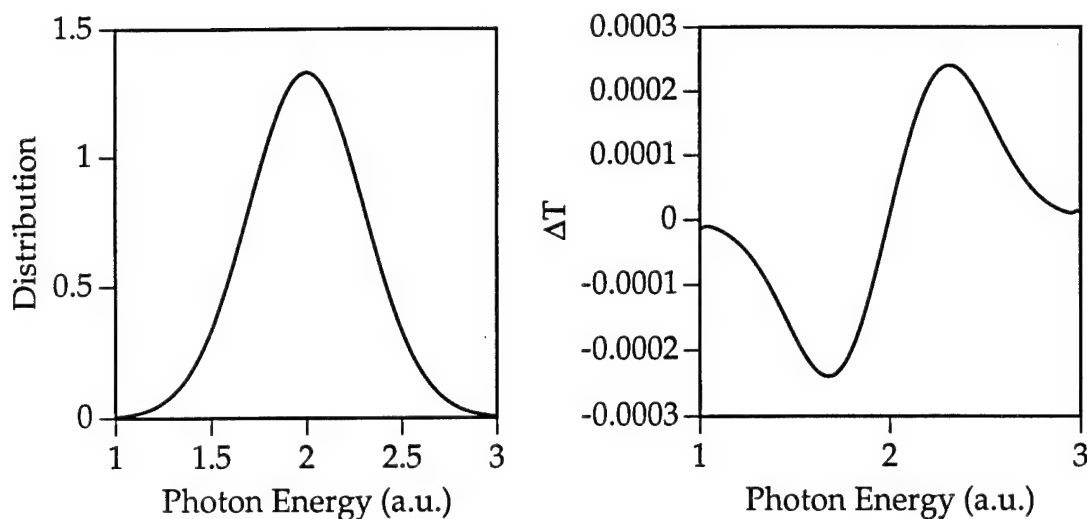


Figure 5.5. Simulated data showing the effect of a distribution of absorbers, such as that shown in Figure 5.4, with different absorption peak energies. The graph at left shows a Gaussian distribution function which broadens the change in transmission from that in Figure 5.4 to that shown in the graph at right. We may see similar electroabsorption effects from a distribution of silicon quantum dots.

The magnitude of the enhancement from quantum confinement depends upon the degree of confinement, since sharper absorption features result in stronger electro-optic effects (Galbraith, 1993). Assuming that the nanometer-size crystalline silicon structures present in porous silicon are quantum confined, then we should expect strong enhancement of the electroabsorption over that observed in bulk silicon. Unfortunately, the nature of the silicon bandgap in such small structures is largely unknown. Whether the silicon bandgap remains indirect or whether it transitions to a direct bandgap, as some theoretical calculations predict, remains to be determined. Electroabsorption measurements may provide insight into these questions.

C. Measurements on Free-Standing Porous Silicon Films

We prepared free-standing porous silicon films, which were sandwiched between ITO/glass electrodes, using the methods outlined in Chapter II. We then measured the photoluminescence, optical transmission, and electroabsorption from these samples. I present the results of these measurements below, with particular emphasis on trying to find a correlation between photoluminescence energy and corresponding features in the electroabsorption spectra.

Table 5.1. Preparation conditions of the free-standing porous layers used for electroabsorption measurements.

Sample number	Crystal orientation	Etching current (mA/cm ²)	Etchant HF concentration	Etching time (min)
1307-10	(100)	10	16%	5
1807-1	(100)	5	25%	15
0802-1	(100)	5	16%	10
0802-2	(111)	5	25%	10

In Table 5.1, I list the preparation conditions for four free-standing porous silicon samples that displayed strong electroabsorption signals. All samples were produced from polished 1-20 Ω cm p-type silicon with the crystal orientations listed in the table. The porous layers etched in 16% HF solutions had noticeably rougher bottom surfaces than the layers etched in 25% HF. Samples #0802-1 and #0802-2 had ~ 3000 Å thick PMMA layers between the top surface of porous silicon and the ITO electrode. In Figure 5.6, I show the measured transmission (solid lines) and photoluminescence (dashed lines) spectra of the four samples. The two PL

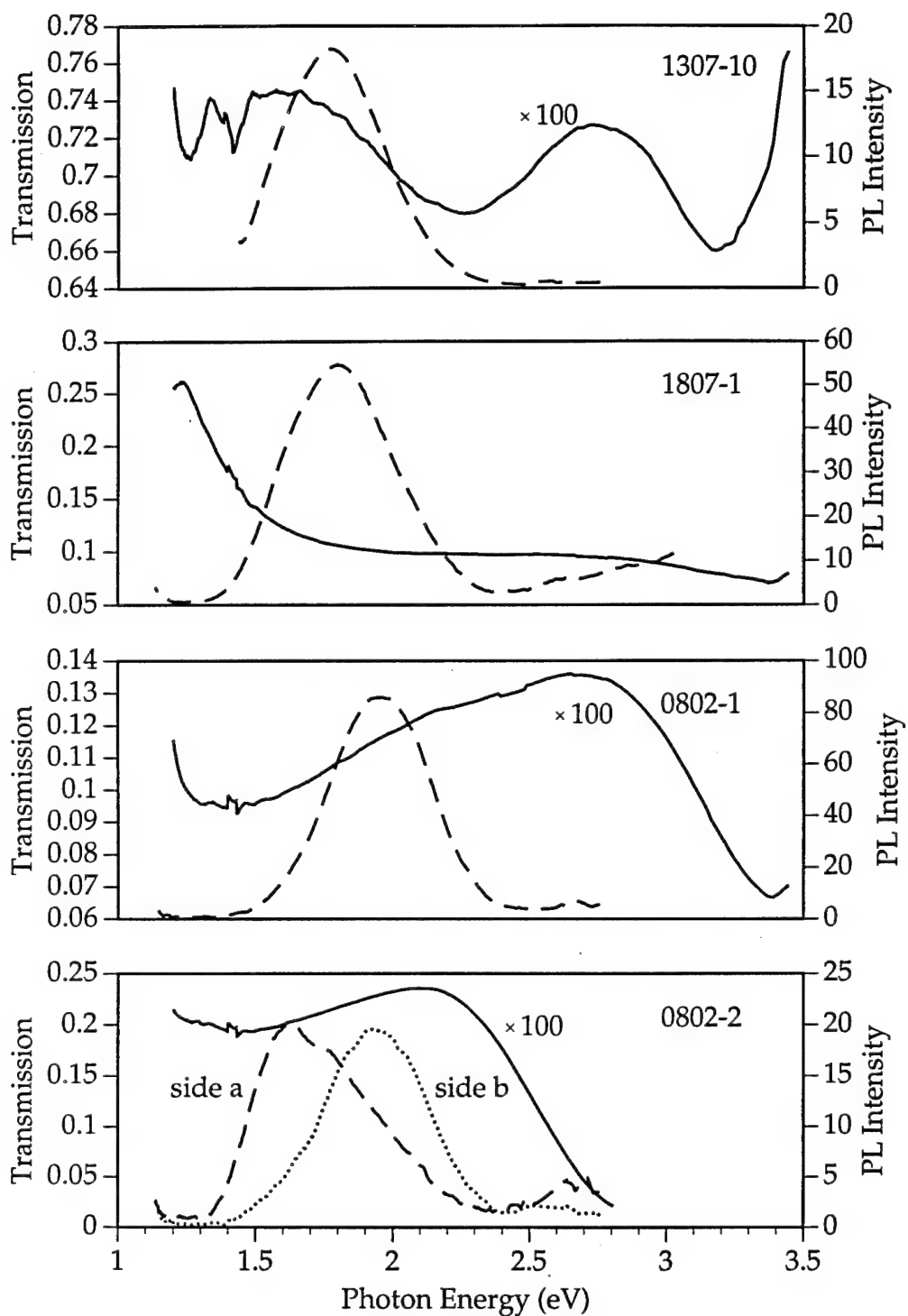


Figure 5.6. Measured transmission (solid lines) and photoluminescence (dashed lines) from the four free-standing porous silicon layers used for electroabsorption.

spectra shown in the bottom graph of Figure 5.6 for sample #0802-2 illustrate the difference in PL from the top and bottom of the porous layer. The very rough free-standing porous layers scattered the incident light quite noticeably. Hence, the transmission spectra probably do not accurately reflect absorption in the films. Very slight optical interference fringes are apparent in the transmission spectra of sample #1307-10.

In Figure 5.7, I show measured electroabsorption spectra from sample #1307-10 for applied voltages of 100 V, 60 V, and 30 V (rms voltages of 50 V, 30 V, and 15 V, respectively, from the square-wave applied voltage waveforms). The two curves on each plot are the in-phase (0°) and quadrature (90°) components of the electroabsorption signal relative to the phase of the applied square wave voltage. We note that the closely-spaced oscillations in the spectra are most likely due to optical interference fringes, as they do not change much in spacing or position with applied voltage. We suspect that these fringes originate from a uniform depletion region on the smooth, top surface of the porous layer across which a large fraction of the applied voltage drops. The rough bottom surface of the porous layer then would not contribute to the electroabsorption. Because of the low HF concentration used in the etchant solution, this sample is highly porous and not very absorptive. As I show in Figure 5.8, the voltage dependence of the magnitude of the electroabsorption oscillations is quadratic, strongly suggesting that the change in transmission is due to the Kerr effect. Since the envelope of the modulated interference fringes is nearly symmetrical about $\Delta T/T=0$, the change in transmission is due mostly to modulation of the real part of the index of refraction and not to absorption modulation. Furthermore,

because the Kerr effect near the band edge in bulk crystalline silicon is much weaker than the Franz-Keldysh effect (Soref, 1987), and since electro-optic effects near the bandgap on a crystallite (quantum confined or not) would show mostly absorption modulation, we suspect that the electrorefraction from this sample originates from non-absorptive, localized states in disordered media and not from absorptive, extended states in crystalline silicon. Based on these arguments, we conclude that the electroabsorption oscillations are likely due to electrorefraction effects in a-SiO_x near the top surface of the porous layer.

Two peaks are present at ~1.6 eV and ~2.2 eV in the envelope of the interference fringes of Figure 5.7. These peaks do not shift with applied voltage and may be related to the weak interference features of the transmission spectrum of Figure 5.6. Since the bottom surface of the porous silicon is so rough, we suspect that these broad interference features may be due to a very thin gap between the top surface of the porous silicon and the top ITO electrode. An electric-field-induced change in the index of refraction of the porous silicon surface would result in an electroreflectance-like modulation of the optical interference. In Figure 5.9, I show a cross section of the porous silicon cell illustrating the narrow gap and thick depletion region that may have led to our observations.

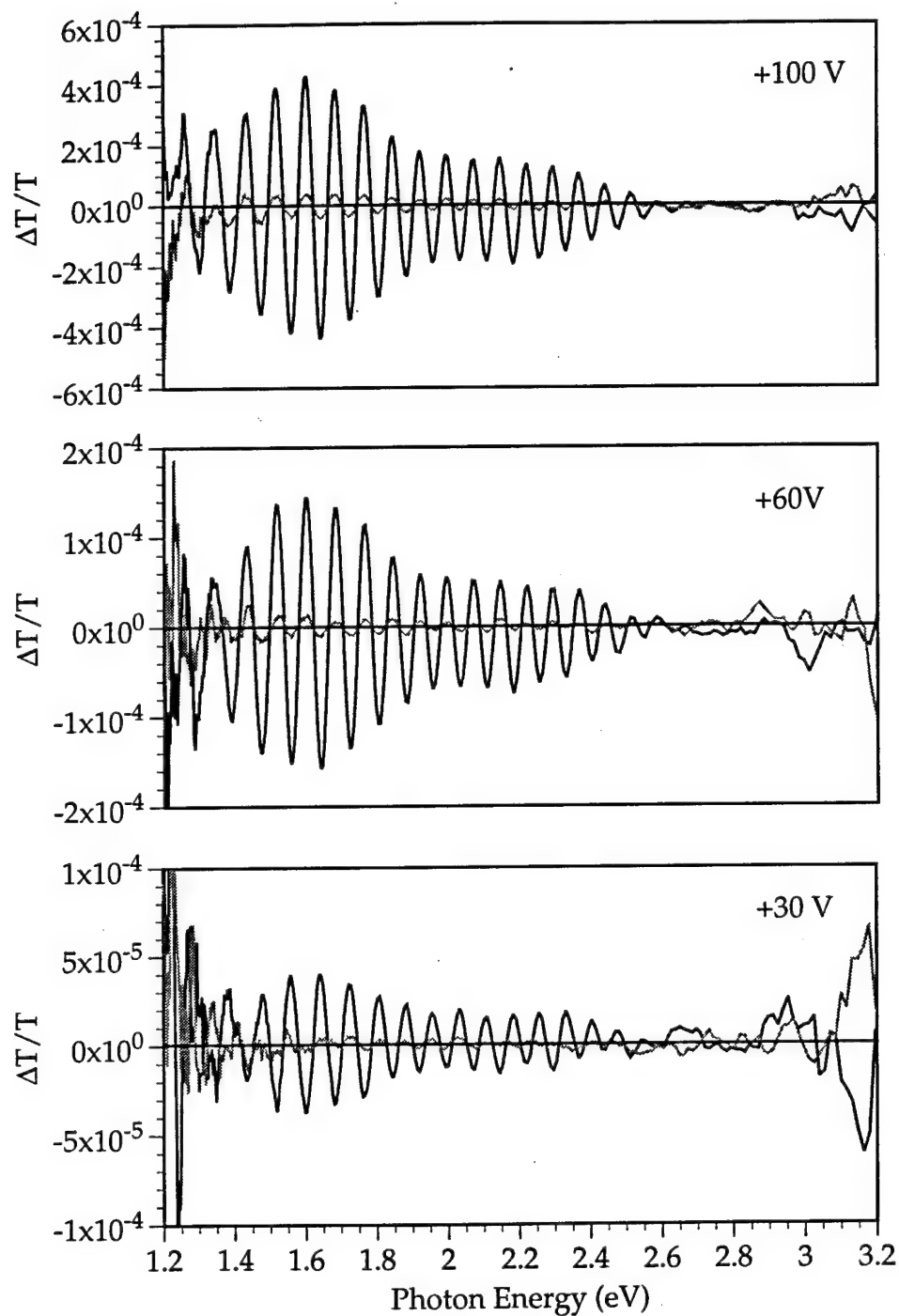


Figure 5.7. Measured electroabsorption spectra of porous silicon sample #1307-10 at applied voltages of 100 V, 60 V, and 30 V. The dark lines represent in-phase (0°) electroabsorption signals while the lighter grey lines represent quadrature (90°) signals.

Finally, I should note that a slight asymmetry towards negative $\Delta T/T$ at ~ 2.2 eV suggests the presence of a weak absorption edge, possibly due to quantum confined silicon crystallites. More experimental investigation is needed to confirm this observation.

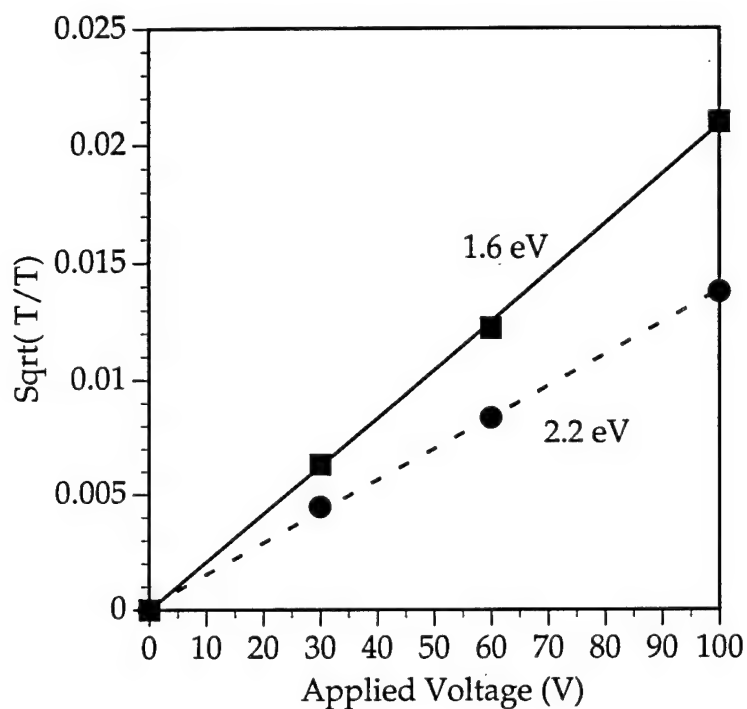


Figure 5.8. Voltage dependence of the envelope of electroabsorption oscillations of sample #1307-10 at photon energies of 1.6 eV and 2.2 eV. The straight lines are quadratic fits to data.

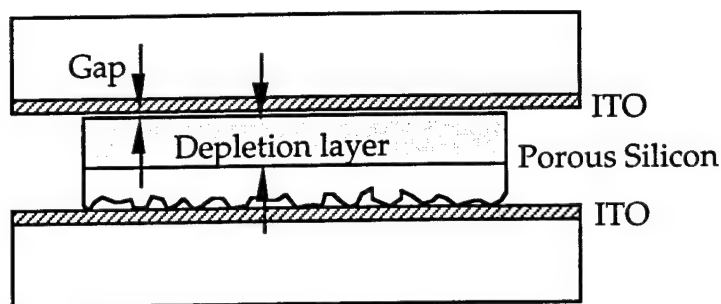


Figure 5.9. Porous silicon cell diagram showing two possible sources of interference fringes in the electroabsorption spectra. A very thin gap between the flat top surface of the porous silicon and the ITO electrode may lead to broad fringes due to electrorefraction of the top surface of the porous silicon. The applied voltage may drop across a thicker, but very uniform, depletion layer in the porous silicon that would lead to closely spaced fringes.

In contrast to the interference-dominated electrorefraction of sample #1307-10 above, the electroabsorption spectra from sample #1807-1 show evidence of crystalline silicon features. The in-phase and quadrature electroabsorption components for this sample are shown in Figure 5.10 for applied voltages of +100 V and -100 V at a frequency of 1 kHz. The sharp peak in $\Delta T/T$ near 1.2 eV resembles the 1.175 eV electroabsorption peak at the band edge of bulk crystalline silicon shown in Figure 5.2. This feature in our data needs further study, particularly at photon energies below 1.1 eV, since the detector response falls sharply at these energies.

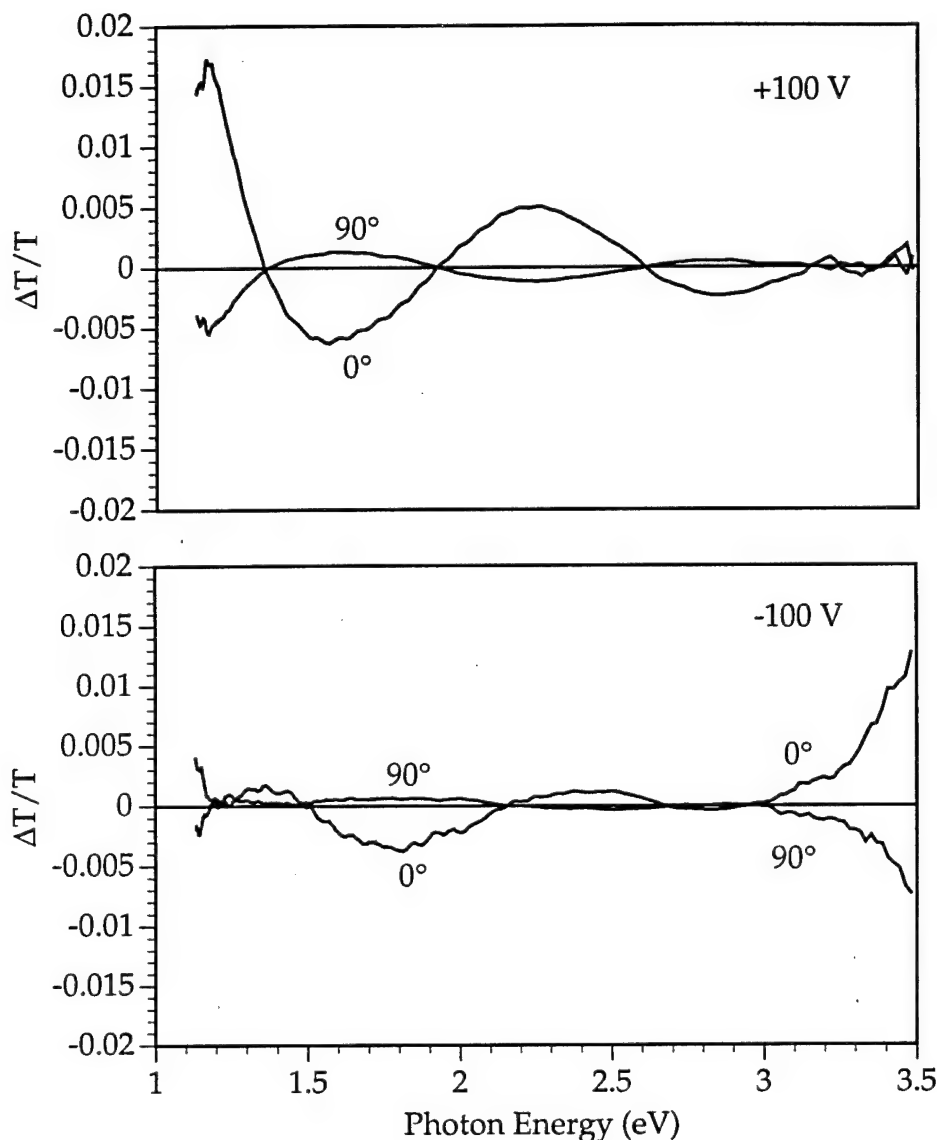


Figure 5.10. Electroabsorption spectra of porous silicon sample #1807-1 measured with applied voltages of +100 V (top graph) and -100 V (bottom graph). The two curves on each graph correspond to the in-phase (0°) signal and out-of-phase (90°) signal components.

As we see in Figure 5.11, the spectral shape of $\Delta T/T$ for sample #1807-1 is highly voltage-dependent. The oscillations in $\Delta T/T$ at voltages above 40 V look similar to the voltage-dependent Franz-Keldysh oscillations observed in $\text{CdS}_x\text{Se}_{1-x}$ crystallites in glass (Cotter, 1990). However, as shown in Figure 5.12, the half period of the oscillations, ΔE_{12}

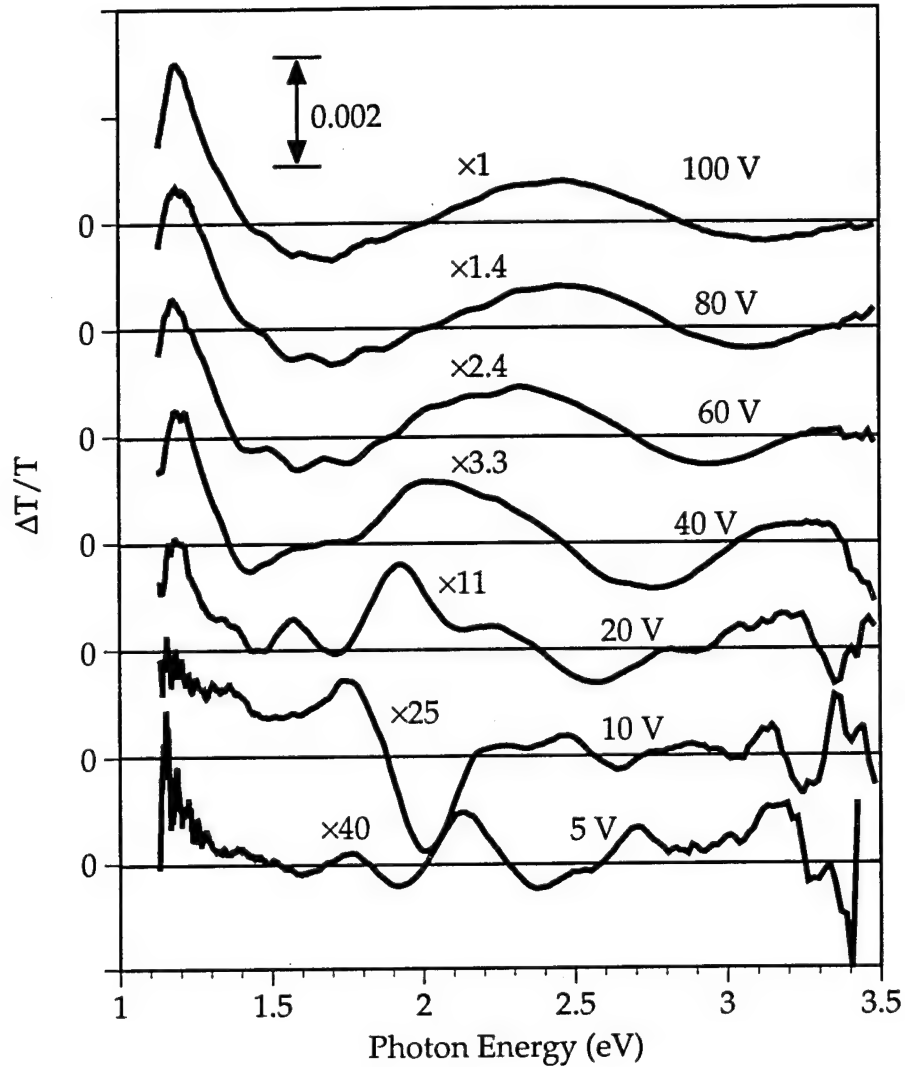


Figure 5.11. Voltage-dependent electroabsorption spectra (in-phase components) of sample #1807-1. The horizontal lines through each curve denote the $\Delta T/T=0$ level for that curve. The applied voltage and scale factor are indicated above each curve. Features in the low voltage spectra may correspond to confined silicon crystallites while features in the high voltage spectra may correspond to bulk-like silicon.

(the energy difference between the first and second zeroes in the $\Delta T/T$ spectrum), increases with increasing applied field, F , by only $\Delta E_{12} \propto F^{0.1}$ instead of the $\Delta E \propto F^{2/3}$ increase predicted for the Franz-Keldysh effect. As I show in Figure 5.13, the oscillations are also not consistent with the modulation of optical interference fringes via the Kerr effect, as the

magnitude of $\Delta T/T$ increases at a rate much less than the F^2 predicted for the Kerr effect. The voltage dependence of the 1.2 eV electroabsorption peak (straight line fit in Figure 5.13) goes as $\Delta T/T \propto F^{1.5}$. While the magnitude predicted by the Franz-Keldysh effect goes as $F^{4/3}$, recall that the measured c-Si electroabsorption peak is proportional to $F^{2.18}$.

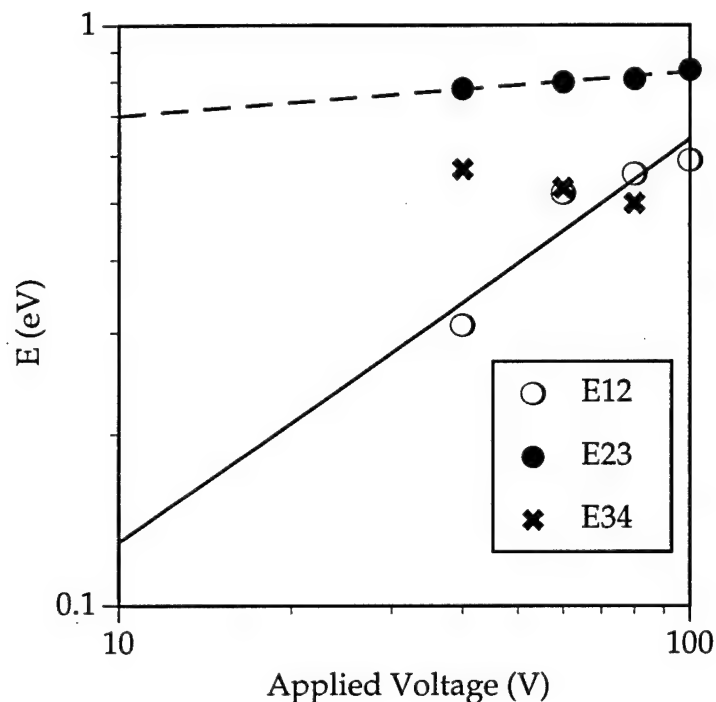


Figure 5.12. Voltage dependence of the oscillation half-periods of the electroabsorption of sample #1807-1. ΔE_{12} is the energy difference between the first and second zeroes, ΔE_{23} is the difference between second and third zeroes, and ΔE_{34} is the difference between third and fourth zeroes of the electroabsorption spectra of Figure 5.11. The straight-line (power-law) fits are $\Delta E_{12} \propto F^{0.08}$ and $\Delta E_{23} \propto F^{0.75}$.

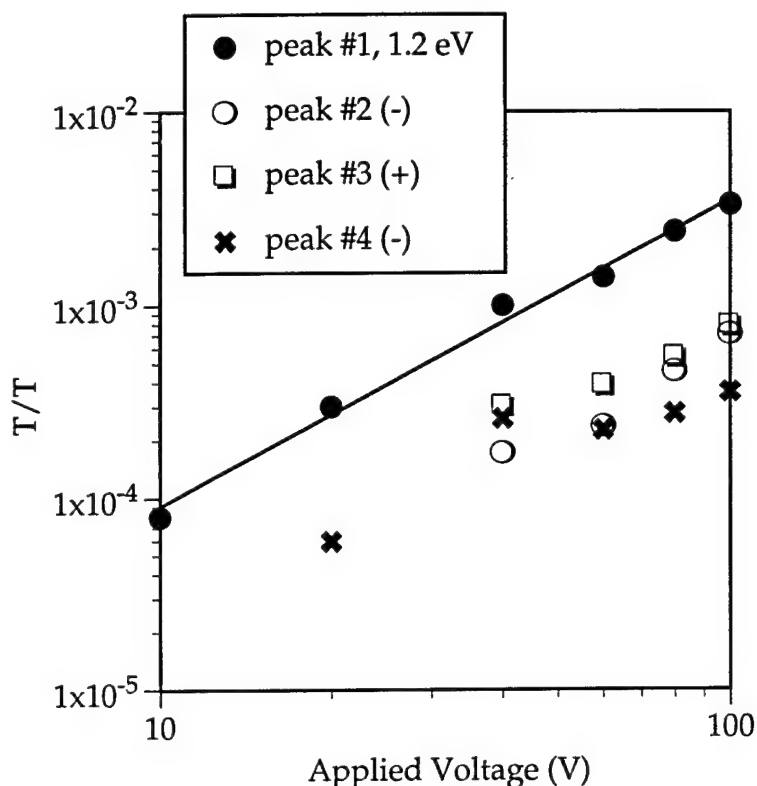


Figure 5.13. Voltage dependence of the high voltage electroabsorption peaks from sample #1807-1 shown in Figure 5.10. The straight line is a power law fit ($\sim V^{1.5}$) to the 1.2 eV peak magnitude.

At low applied fields, the electroabsorption spectra of Figure 5.11 exhibit a radically different shape than at high fields. In fact, the oscillatory features in the 5, 10, and 20 V spectra, particularly between 1.6-2.4 eV, look much more like the features we would expect to observe from a distribution of silicon quantum dots (as shown in Figure 5.5). Because of the amount of structure in the spectra, and because it is difficult to follow the voltage evolution of any particular feature, we cannot define a bandgap with any certainty. The range of energies of these low voltage features would seem to be just slightly higher than the photoluminescence energies, which peak at 1.8 eV. One possible explanation for the strong voltage dependence of the electroabsorption

spectral shape is that the applied voltage drops primarily across a top nanoporous insulating region as well as a lower mesoporous charge depletion region, as I show in Figure 5.14. We have already seen that the top $\sim 1\text{-}2\text{ }\mu\text{m}$ of the porous layer has the smallest silicon remnants. Thus, for low applied voltages, the voltage may drop mostly across this top nanoporous layer where we see evidence of quantum dot structures in the electroabsorption. For high applied voltages, a depletion layer may form in the more bulk-like, mesoporous bottom layer, and the observed electroabsorption may well represent features inherent to bulk silicon. We note that the presence of a depletion layer whose width depends on applied voltage means that the electric field across this layer will not be proportional to the applied voltage so that attempts to compare the voltage dependence with theory will be complicated, if not impossible. The differences between the high field electroabsorption spectra and the low field spectra may be due, as was the case for bulk c-Si, to field ionization of excitons.

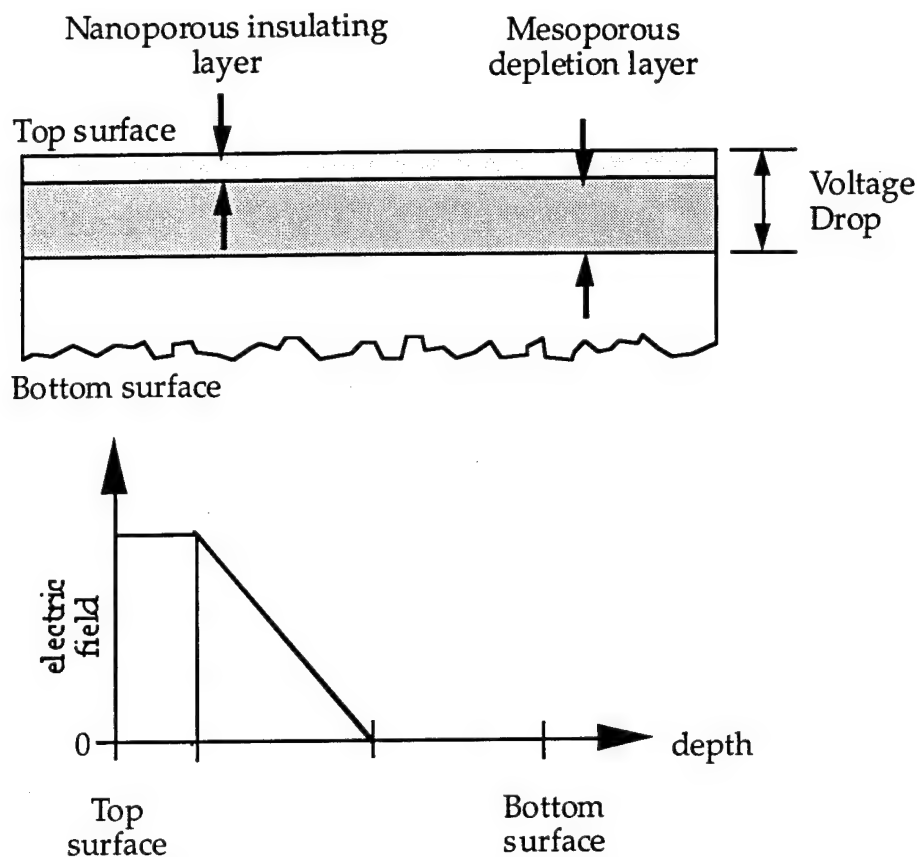


Figure 5.14. Diagram showing possible electric field distribution in a free-standing porous layer. Voltage may drop across a top nanoporous insulating layer as well as a lower mesoporous depletion layer.

The third sample in our series (Table 5.1) is #0802-1. Like sample #1307-10, sample #0802-1 was also etched in 16% HF solution and should have comparable porosity. I show the electroabsorption spectra of this sample in Figure 5.15. The measured electroabsorption does not exhibit the strong interference fringe features of sample #1307-10 but instead shows broad, nearly constant absorption change from ~ 1.2 - 2.5 eV. The oscillation in $\Delta T/T$ between ~ 2.5 - 3 eV, which is similar to that observed at ~ 1.6 - 2.4 eV in the low voltage spectra of sample #1807-1, may also be indicative of silicon quantum dots. We note that the photoluminescence from this sample peaks at approximately 1.95 eV. In Figure 5.16, we see

the voltage dependence of the electroabsorption spectra of sample #0802-1. The many small features in each spectrum appear to have correspondence at different voltages. We cannot rule out the possibility that these oscillations may be due to optical interference effects as in sample #1307-10. By averaging $\Delta T/T$ over the energy range 1.4-2.4 eV and plotting this value versus applied voltage, we obtain the voltage dependence shown in Figure 5.17. A power-law fit to the last four data points (40-100 V) yields an $F^{1.37}$ field dependence, which is close to that predicted for the Franz-Keldysh effect but much lower than the quadratic dependence of sample #1307-10.

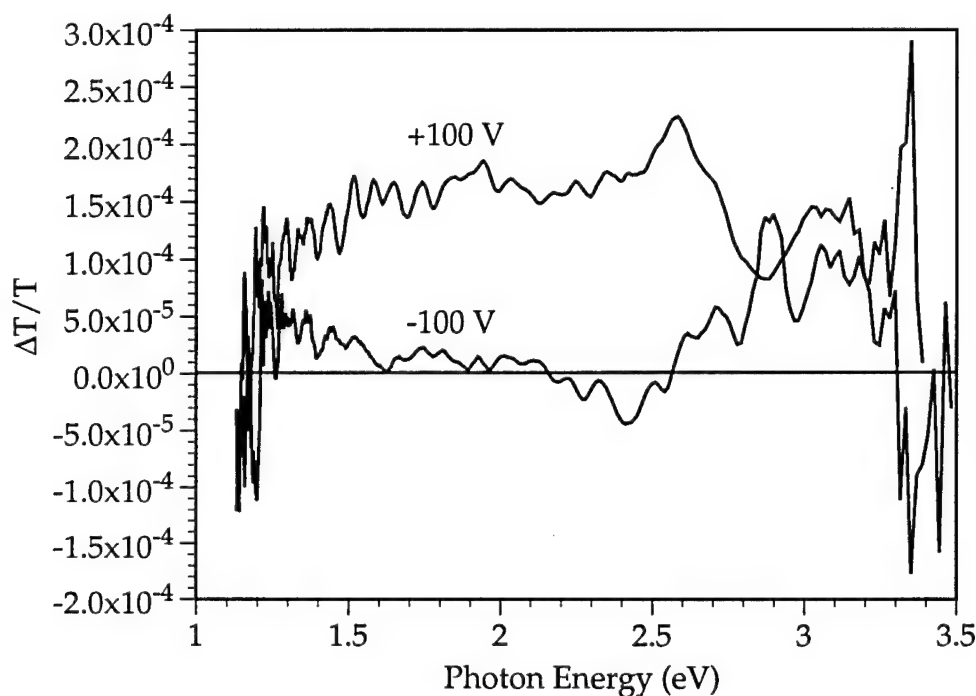


Figure 5.15. Electroabsorption spectra (in-phase components) of sample #0802-1 measured at applied voltages of +100 V and -100 V.

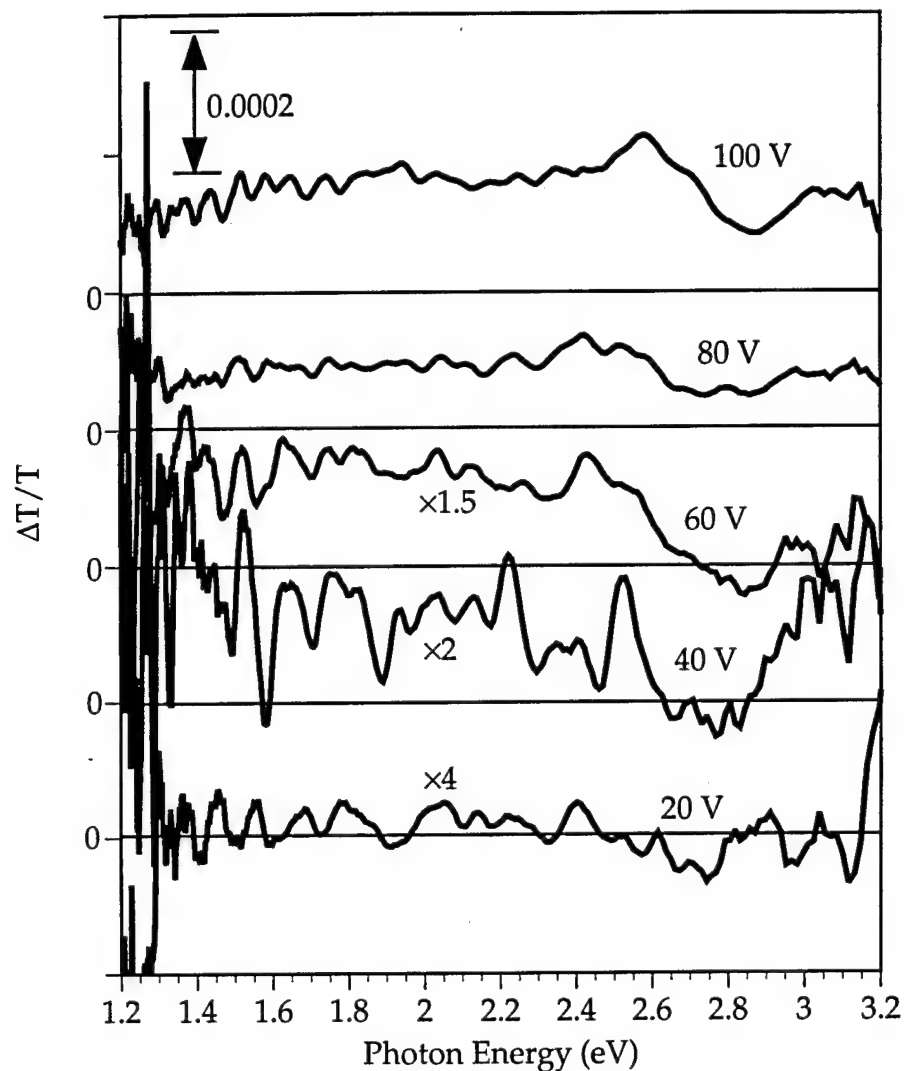


Figure 5.16. Voltage-dependent electroabsorption spectra (in-phase components) of porous silicon sample #0802-1. The horizontal lines through each curve represent the zero level for that spectrum. The voltage and scale factor are indicated above each curve.

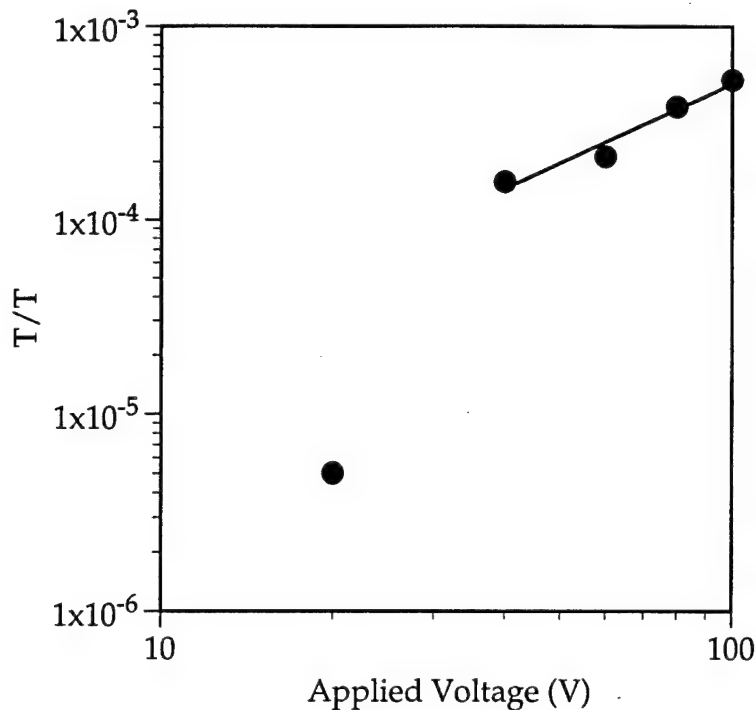


Figure 5.17. Voltage dependence of the average value of $\Delta T/T$ for sample #0802-1 over the photon energy range from 1.4 eV to 2.4 eV. The power law fit to the last four data points shows an $F^{1.37}$ dependence.

As I show in Figure 5.18, the electroabsorption spectrum of sample #0802-1 is nearly constant with frequency of the applied voltage from 10 Hz to 1 kHz. For the 10 kHz electroabsorption spectrum, not shown in Figure 5.18, the magnitude of the $\Delta T/T$ spectrum at this frequency is well below that at 1 kHz, probably due the capacitance of the porous silicon cell. This data simply demonstrates that dielectric relaxations or carrier redistributions in the porous layer occur at times much shorter than 1 msec.

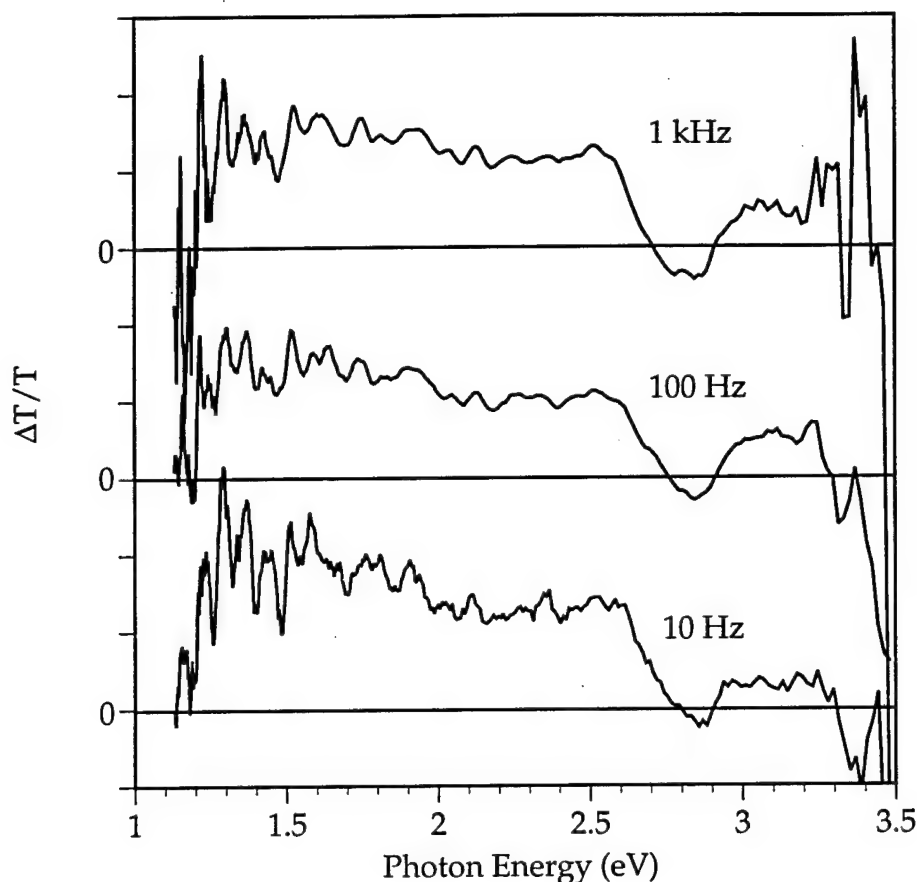


Figure 5.18. Frequency-dependent electroabsorption of sample #0802-1 showing that the spectra are independent of frequency up to 1 kHz. The magnitude of the electroabsorption drops considerably by 10 kHz. The zero lines for each spectra are indicated on the left axis.

Our fourth sample, #0802-2, was etched in 25% HF solution under conditions similar to that of sample #1807-1. The electroabsorption spectra for applied voltages of ± 100 V are plotted in Figure 5.19. Two features are prominent in these spectra, a sharp peak at ~ 1.9 eV and a broad peak at ~ 2.8 eV. The photoluminescence from sample #0802-2 peaks at 1.95 eV on one side of the sample and at 1.6 eV on the other side. As with the other samples, correlation of photoluminescence energy with electroabsorption features is speculative at best.

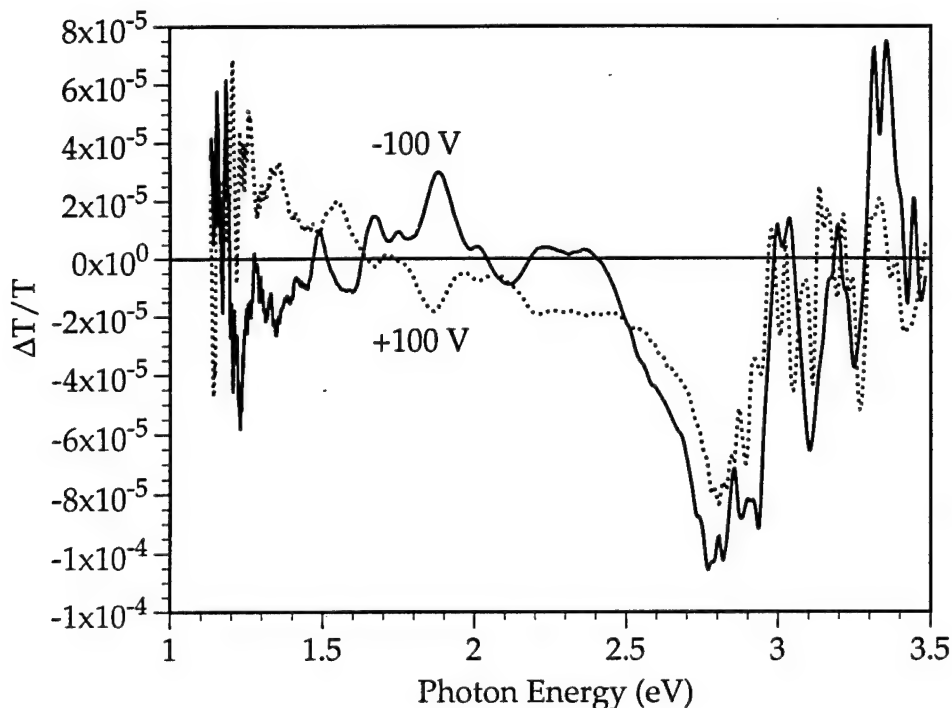


Figure 5.19. Measured electroabsorption spectra of sample #0802-2 for applied voltages of +100 V and -100 V.

C. Discussion

In Table 5.2, I summarize the observed electroabsorption effects in our porous silicon films (where known), in bulk crystalline silicon, and in amorphous silicon. We attribute the oscillations in the electroabsorption of sample #1307-10 to Kerr effect electrorefraction in a weakly-absorbing top a-SiO_x layer of the porous film. Because the voltage dependence is close to the theoretical $V^{4/3}$, we attribute the 1.2 eV electroabsorption peak of sample #1807-1 to the Franz-Keldysh effect at the band edge of essentially bulk crystalline silicon. The spectral shapes of the ~1.6-2.7 eV features in the low field electroabsorption spectra of sample #1807-1 are similar to the relatively sharp electroabsorption spectra predicted for a distribution of quantum dot structures (Figure 5.5) and observed in $\text{CdS}_x\text{Se}_{1-x}$ quantum dots (Cotter, 1990). Because of these similarities, we

suspect that the ~1.6-2.7 eV electroabsorption in sample #1807-1 may be due to modulation at the band edge of silicon quantum dots via the quantum confined Stark effect. We see similar electroabsorption features at ~2.4-2.8 eV in sample #0802-1 and at 1.9 eV and 2.8 eV in sample #0802-2, which may also be due to the presence of silicon quantum dot absorptions.

Table 5.2. Summary of the observed electroabsorption effects in our porous silicon samples (P-Si), in crystalline silicon, and in amorphous silicon.

Sample	$\Delta T/T$ Peak Energies	Absorptive/Refractive	$\Delta T/T$ Voltage Dependence	Suspected Effect
#1307-10 P-Si	oscillations, envelope peaks: 1.6 eV 2.2 eV	refractive	V^2	Kerr, Δn
#1807-1 P-Si	High Field: oscillations 1.2 eV Low Field: 1.6-2.7 eV	? absorptive absorptive	varies $V^{1.5}$?	? Franz-Keldysh Stark?
#0802-1 P-Si	2.4 eV-2.8 eV	absorptive	$V^{1.37}$	Stark?
#0802-2 P-Si	1.9 eV 2.8 eV	absorptive	?	Stark?
Bulk c-Si	1.06 eV 1.175 eV	absorptive	$V^{2.18}$	Franz-Keldysh
a-Si:H	~1.7 (bandgap-dependent)	absorptive	V^2	Kerr, $\Delta \alpha$

As the data presented above clearly demonstrates, electroabsorption signals from free-standing porous silicon layers are quite measurable and may provide evidence of quantum confined silicon band states. Unfortunately, there is not much similarity between the electroabsorption spectra from different samples and no clear understanding yet of the processes involved in porous silicon electroabsorption. Producing free-standing porous silicon layers of large enough areas was extremely difficult. Our efforts to produce identical samples to check reproducibility

have so far been futile. A more thorough investigation would certainly help derive more meaning from the data. An in-depth study of the electroabsorption features near the bulk silicon band edge at 1.1 eV might be useful in separating the effects of bulk-like structures from those of highly confined structures. In addition, temperature-dependent electroabsorption and further low field measurements might lead to an understanding of the interesting low voltage features from sample #1807-1 of Figure 5.11.

A number of issues complicate data interpretation. In particular, the effects of optical scattering appear to mask absorption features. Scattering effects could be minimized by using an integrating sphere or by using photothermal deflection spectroscopy. In addition, optical interference effects presumably caused by a thin gap between the top surface of porous silicon and the top ITO electrode could be eliminated by using an evaporated metal top contact.

D. Conclusions

We have successfully measured electroabsorption spectra from several free-standing porous silicon films. These data vary greatly from sample to sample, but we do see evidence that the applied voltage primarily drops across a uniform depletion or insulating region near the top surface of the porous layer. In addition, oscillatory features in the low field electroabsorption spectra would seem to indicate the presence of sharp absorption lines that may be due to quantum states in silicon nanocrystals. In one highly porous sample, #1307-10, we attribute the oscillatory electroabsorption spectra to Kerr effect electrorefraction in a

weakly-absorbing α -SiO_x layer near the top surface of the porous silicon. Our experiments strongly suggest that electroabsorption measurements of porous silicon may yield valuable information about the nature of the silicon bandgap in highly confined crystallites; however, further investigation is required, and definitely endorsed, to understand these results.

CHAPTER VI

INVESTIGATION OF POSSIBLE REDEPOSITION PROCESSES IN POROUS SILICON

A. Introduction

Much discussion in the porous silicon literature has focused on the possibility that the luminescence in porous silicon arises from surface molecular agents, such as siloxene (see chapter I). Not much has been said, however, about possible origins of luminescent surface agents in porous silicon. Since these compounds typically contain silicon, oxygen, and hydrogen, they could conceivably form on the porous surface by air exposure after etching the porous layer, by some reaction of the chemical etchant with the bare silicon surface, or by redeposition onto the porous surface during the etching process. In this chapter, I discuss our*

*I am indebted to Lee Hirsch, an undergraduate research assistant, who performed many of the experiments in this chapter and to Kevin Kuhn, who helped with the XPS measurements.

investigation into the latter process -- redeposition of luminescent compounds.

We do not know whether redeposition takes place in porous silicon, and, if it does, whether the deposited compounds are luminescent. The hypothesis would seem to have some merit, though. Since porous silicon etches predominantly at the bottoms of very narrow (<100 Å diameter) and very long (up to tens of microns) pores, the etchant near the bottoms of the pores should be highly saturated with silicon in solution. On its way out of the pores, the saturated etchant would come in contact with a large surface area of porous silicon. Thus, the situation may be favorable for the solid phase redeposition of silicon compounds. Furthermore, several researchers have noted that the topmost 1-2 μm layer of porous silicon is predominantly amorphous and yet emits light more efficiently than lower layers (Noguchi, 1992; Prokes, 1992), which may be an indication that amorphous compounds deposit in the upper layers. While I have used siloxene as an example, redeposition of other potentially luminescent compounds, such as amorphous silicon, amorphous silicon oxyhydrides (a-Si:O:H), or even defective oxides, seems equally possible.

Our experiments, which were designed to check for redeposition, included investigating a luminescent residue that formed on n-type porous silicon during etching in saturated chemical etchant, anodizing and soaking porous silicon layers in solutions saturated with silicon compounds, and etching silicon through a free-standing porous alumina mask. We found that the residue on chemically-etched n-type silicon had a lower energy photoluminescence (PL) peak than that of the underlying

porous silicon layer. We performed x-ray photoelectron spectroscopy (XPS) measurements on this residue and identified the primary chemical compounds in it. Anodizing and soaking porous layers in fluosilicic acid solutions after etching significantly enhanced the nominally 1.6-1.8 eV PL from the porous layers. Finally, we found very limited evidence for redeposition of luminescent compounds in the porous alumina etch masks. Preceding discussion of these results, in the following section I give a brief introduction to anodic and chemical etching processes in porous silicon with emphasis on how silicon is removed from the porous network.

B. Silicon Etching Chemistry

1. Anodic Etching

Lehmann and Gösele (Lehmann, 1990) proposed the mechanism shown in Figure 6.1 for the anodic dissolution of silicon in porous silicon. In the first step, a F^- ion plus an injected electronic hole (h^+) team up to replace the Si-H bond at the surface with a Si-F bond. In step 2, a second F^- ion attacks the other Si-H bond and injects an electron into the silicon. The two H atoms combine and are released as H_2 gas. Because of fluorine's high electronegativity, the Si-F bonds polarize the silicon atom and lower the electron density of the remaining Si-Si bonds, thereby weakening these bonds for attack by HF as shown in step 3. Once all four silicon bonds have been broken, the silicon is removed from the surface in the form of SiF_4 . SiF_4 may then react with 2 HF molecules to form H_2SiF_6 (fluosilicic acid), which in solution ionizes to $2H^+ + SiF_6^{2-}$. I have shown the reaction in step 4 of Figure 6.1 as a two-way reaction since above some

threshold aqueous concentration (approximately 13.3% at standard temperature and pressure), H_2SiF_6 decomposes back into $2\text{HF} + \text{SiF}_4$. (Budavari, 1989)

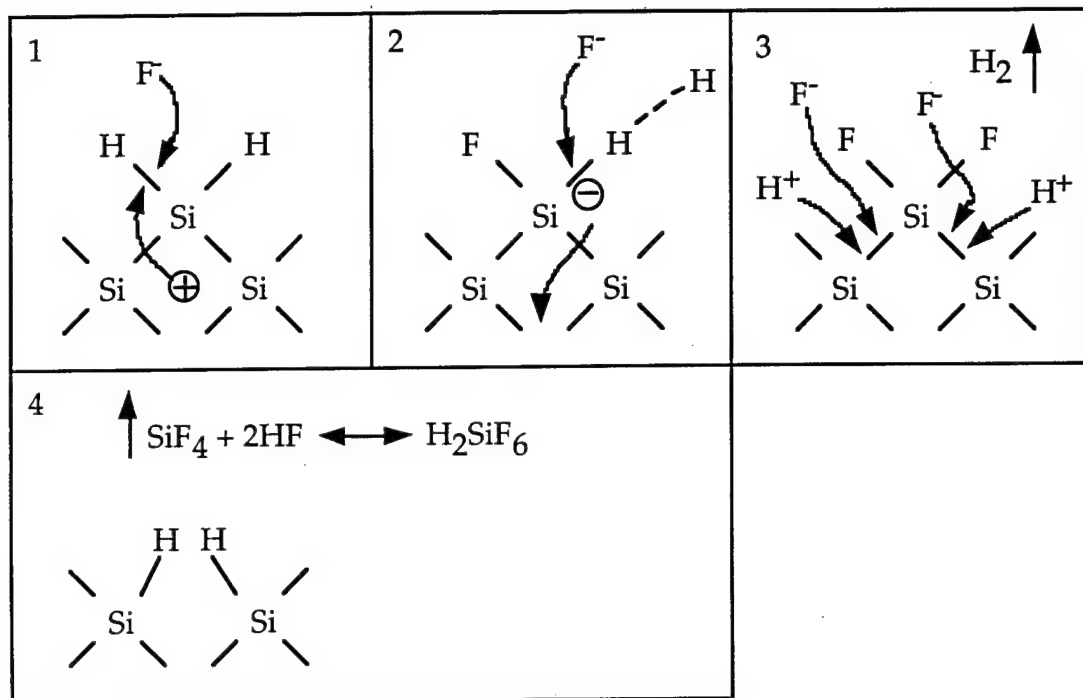


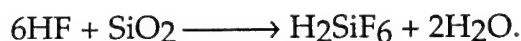
Figure 6.1. Mechanism proposed by Lehmann and Göesele for the anodic dissolution of silicon.

As the dissolution reaction continues, electronic holes are preferentially injected to silicon atoms at the bottom of the pit left by removal of the previous silicon atom. In this way, pores begin to form. Lehmann and Göesele suggest that, in p-type silicon, as the pore walls become thinner, quantum confinement effects cause a widening of the bandgap and a dramatic decrease in conductivity. The remaining pore walls cease to etch and a porous structure results. In n-type silicon, dissolution of the pore walls ceases once all carriers are depleted from the walls due to the surface space-charge-region formed under anodic bias.

Subsequent experiments suggest, however, that charged surface traps are responsible for the higher resistivity of the remaining pore walls (Lehmann, 1995). Whatever the cause, the end result is the same -- porous silicon.

2. Chemical Stain Etching

Chemical stain etches generally consist of an oxidizing agent and an oxide etchant, typically HF. While the chemistry of the silicon oxidizing reaction is a matter of debate (Kelly, 1994), the chemistry of SiO₂ dissolution in HF is simply



Thus, again we end up with the same reaction product, fluosilicic acid, carrying away silicon atoms.

3. Redeposition

As we have seen, silicon diffuses out of the porous network in the form of either SiF₄ (g) or H₂SiF₆ (l). The question is: are there any chemical reactions taking place as silicon leaves the pores that would create solid phase redeposition? All the atomic species are available to create potentially luminescent silicon compounds such as amorphous silicon (a-Si), amorphous silicon oxides (a-SiO_x), siloxenes (Si₆O₃H₆), or polysilanes ((SiH)_n). An analysis of these possible reactions would be extremely complex.

The relative concentrations of H₂SiF₆ and SiF₄ must be in dynamic equilibrium at each point in the porous layer. Although this would seem

to be a closed loop system, other silicon compounds and radicals almost certainly must exist, even if in minute quantities or for very short periods of time. Furthermore, the highest concentrations of reactive radicals or intermediate compounds would have to be at the point of greatest change in local equilibrium. This point must certainly be at the top interface between the porous silicon layer and the etchant solution, where highly saturated etchant under very high pressure from hydrogen gas meets the bulk, unsaturated etchant solution. Thus, by these purely speculative arguments, redeposition should have the highest probability of occurring at the very top layer of porous silicon. Our hypothesis correlates well with the observations of Noguchi *et al.* and Prokes *et al.*, referenced earlier, of strong luminescence and low crystallinity in the topmost layers of porous silicon.

C. Redeposition Experiments

As I outlined in the introduction of this chapter, we tried a variety of experiments looking for evidence of redeposited luminescent compounds. In this section, I present the results of three such experiments from which we may infer evidence for redeposition.

1. Analysis of the Luminescent Residue on n-type Porous Silicon

The initial purpose of this experiment was to see the effects of chemically stain-etching porous silicon in highly saturated etchant solutions with the reasoning that if silicon compounds indeed redeposit out of saturated etch, then porous silicon etched in saturated etchant solutions may yield higher intensity PL than those layers etched in fresh solutions. While most of the results from this experiment were

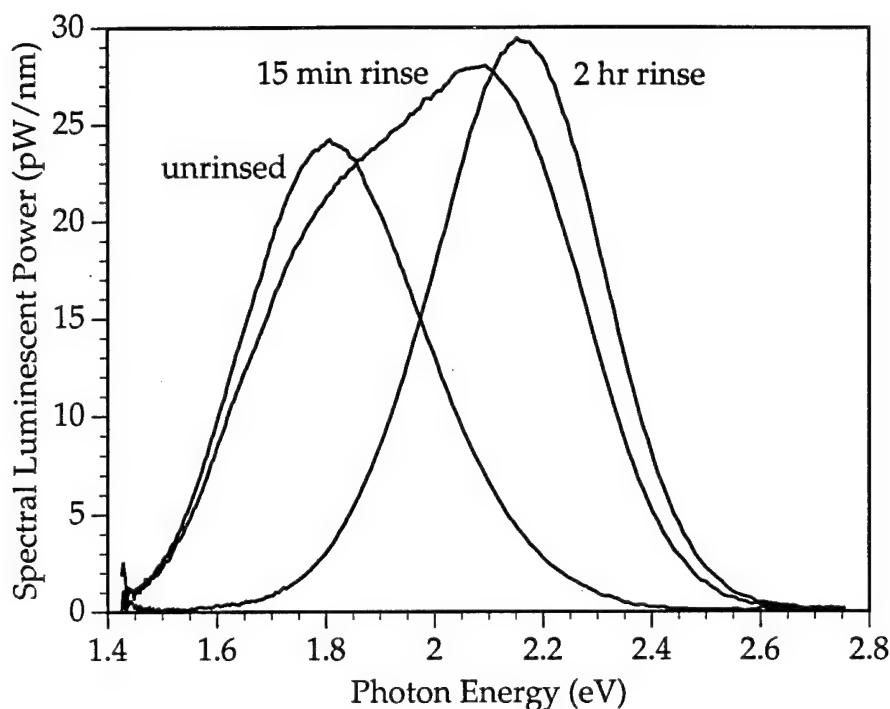


Figure 6.2. Photoluminescence spectra of stain etched (111) n-type porous silicon as a function of H₂O rinsing time to remove the cream-colored residue from the sample surface.

uninteresting, we found that by etching unpolished, (111)-oriented, n-type silicon wafers in the HF:H₂SO₄:NaNO₂:H₂O (1 ml:4.5 ml:0.158 g: 4.5 ml) etchant of Kelly *et al.* (Kelly, 1994) for long times (several hours), a thick, cream-colored residue formed on the porous silicon surface. In addition, a white precipitate formed in the etchant solution. The precipitate was soluble in water but not alcohol. We separated the precipitate from the etchant, dried it, and put it aside for further measurements. The cream-colored residue was barely soluble in water and gave bright orange PL. As I show in Figure 6.2, the PL from the residue had a peak energy of 1.8 eV. Rinsing in deionized water slowly removed the residue and shifted the PL peak energy to nearly 2.2 eV. Since the residue was fairly thick in appearance, we expect that the 1.8 eV PL indeed came from the residue and not from the porous layer below. Two very distinct peaks are visible in

Figure 6.2 as the residue is removed. These data provided us with our first indication of the possible redeposition of luminescent compounds.

To find out what the chemical composition of the residue was, we used x-ray photoelectron spectroscopy (XPS), which provides an ideal method to characterize the atomic species and their bonding configurations on the surface. Since XPS is sensitive only to the top ~ 50 Å surface layer, this technique allowed us to measure the chemical makeup of the residue versus the chemical makeup of the rinsed porous surface. We performed these measurements using a Perkin-Elmer XPS system with a monochromatic Cu $K\alpha$ x-ray source. The XPS spectra were corrected for background electron emission as well as sample charging effects. We measured five samples: n-type with residue, n-type rinsed (no residue), p-type unrinsed, p-type rinsed, and the dried white precipitate from the etch solution. All samples were etched with the HF:H₂SO₄:NaNO₂:H₂O solution. Table 6.1 gives the XPS-measured atomic concentrations for each sample surface. We note that the Na Auger line has the same binding energy as the oxygen O1s peak from which we compute oxygen concentration. The computed O concentrations from samples with significant amounts of Na will therefore be slightly higher than the true O concentrations. Also, adsorbed H₂O increases the O reading.

Table 6.1 indicates that the surfaces of the n-type rinsed, p-type unrinsed, and p-type rinsed samples are all primarily composed of SiO₂ plus carbon contaminants. We did not carry out more in-depth studies of these samples to see what bonding configurations were present at the surfaces. The precipitate, which luminesced blue under UV light, appears

to be composed of sodium sulfates and possibly carbonates. The amount of silicon present seems to be negligible, making the precipitate uninteresting for this study. However, it may account for the blue PL observed in some chemically-etched porous layers.

Table 6.1. XPS results showing atomic concentrations at the surfaces of the five samples. The subscript on the elemental symbols indicates the orbitals measured.

Element	Atomic Concentration (%)				
	n-type unrinsed (residue)	n-type rinsed	p-type unrinsed	p-type rinsed	precipitate
O _{1s}	45.7	67.3	59.4	59.1	49.0
Si _{2p}	23.5	29.0	27.4	23.9	0.4
C _{1s}	1.3	2.4	11.1	16.4	32.0
F _{1s}	22.4	1.4	1.7	0.3	-
Na _{1s}	7.0	-	-	-	8.0
S _{2p}	<1	-	-	-	9.2
N _{1s}	-	-	0.4	0.3	1.3

We can figure out the bonding configurations of the different elements by comparing the peak energies for each emission line with a table of previously measured energies for different compounds. In Figure 6.3 I show the Si_{2p} line of the residue on the unrinsed n-type sample. This emission line is well fit by three nearly Gaussian peaks with binding energies at 104.8, 103.3, and 100.5 eV, which correspond to silicon bonded as SiF₆²⁻, SiO₂, and either SiC or Si¹⁺ (silicon with one Si-O and three Si-Si, or possibly Si-H, bonds) (Himpsel, 1988), respectively. Based on the

relative areas of these three emission lines, as well as the bonding configurations of O, F, Na, and C, we estimate that the residue consists of ~44% SiO₂, ~32% NaSiF₆, and ~24% of an undetermined origin. Of this unknown material, ~22% are Si atoms, ~68% are O atoms, ~5% are C atoms, and ~5% are F atoms. The XPS measurement is not sensitive to hydrogen. There appears to be a small fraction (~2-3%) of SiC in the residue. Certainly, a large fraction of the remaining oxygen is in the form of adsorbed water on the surface; however, we still appear to have some unaccounted-for silicon (~2%) that may be bonded in the Si¹⁺ oxidation state. "Siloxenes" (which appears to be something of a misnomer since the bonding models indicate that the Si-O bond is a single, not a double, bond) (Brandt, 1992), siloxanes, and silanols all may have this oxidation state. As a cautionary note, I should say that the fractional errors of the measurement are on the order of a percent so that more XPS data really needs to be collected and analyzed before we can conclude that a measurable amount of Si¹⁺ is present.

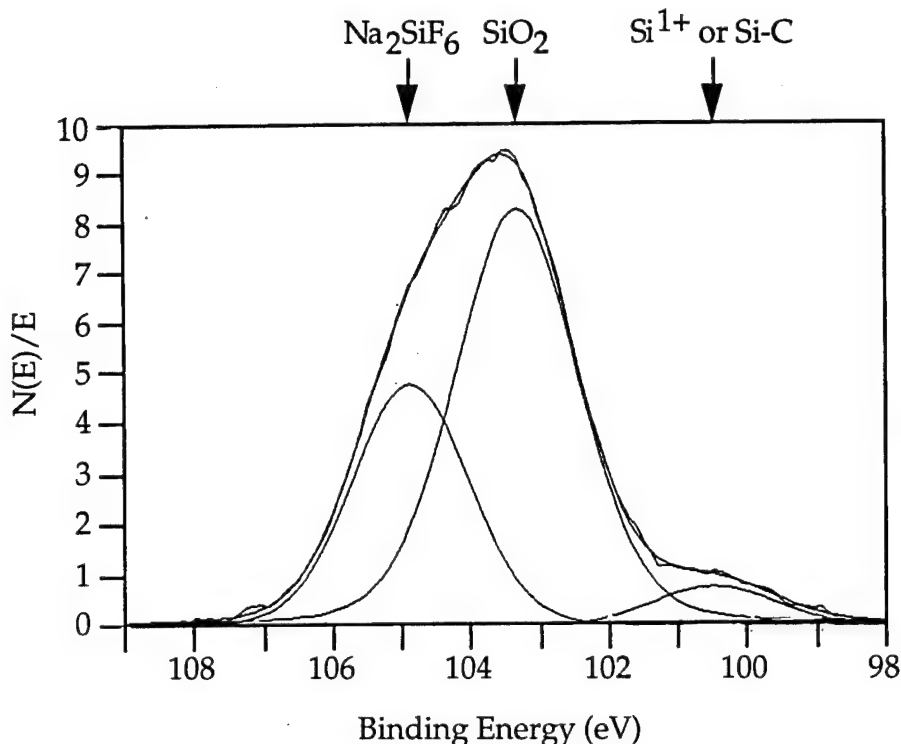


Figure 6.3. Si_{2p} XPS spectrum of the cream-colored residue on stain etched (111) n-type silicon. The spectrum indicates that ~32% of the silicon is bonded as SiF₆ (104.8 eV), ~63% as SiO₂ (103.3 eV), and ~5% as SiC or Si¹⁺ (~100.5 eV).

2. Anodizing and Soaking Porous Silicon Layers in H₂SiF₆ Solution

The purpose of this set of experiments was to determine the effect of saturated etchant, which we know to be in the form of H₂SiF₆, on previously-etched porous silicon layers. To see if the H₂SiF₆ enhanced the PL, we anodized and soaked anodically-etched porous layers in aqueous H₂SiF₆ solutions and compared the resulting PL to that of porous layers with no post treatments.

We produced the aqueous H₂SiF₆ solution (~13% concentration) by the reaction of HF and SiO₂ (glass microscope slides) using excess SiO₂ so

that the HF would be completely depleted. A steam-like gas evolved (probably SiF_4 and steam) during the reaction, and a white precipitate formed. We believe the precipitate is silicic acid, H_2SiO_3 , which is also known as silica gel. When separated and dried, this precipitate gave off strong blue photoluminescence, which may account, at least in part, for the blue PL observed in some porous silicon samples. We extracted the aqueous fluosilicic acid by filtering out the precipitate particles.

a. Anodizing Porous Silicon Layers in H_2SiF_6

We produced three identical porous silicon samples for this experiment by anodically etching (100)-oriented, 150-250 Ω cm p-type silicon wafers for 10 min in 25% ethanoic HF at current densities of 5 mA/cm^2 . We anodized one of the porous silicon layers further in 13% aqueous H_2SiF_6 solution and another in 0.1 M KNO_3 . Both of these samples were anodized at 1 mA/cm^2 for 10 min on the freshly etched and H_2O -rinsed porous silicon layers. The third porous layer had no post-etch treatment and was used as a control sample. Bustarret *et al.* (Bustarret, 1992a) previously reported that anodizing porous silicon in 0.1 M KNO_3 after etching produces an anodic oxide layer in the porous network and has the effect of increasing PL intensity and increasing PL energy. The purpose of anodizing our third sample in 0.1 M KNO_3 was to check that the post-etch anodization in aqueous H_2SiF_6 solution did not produce such an electro-oxidized layer.

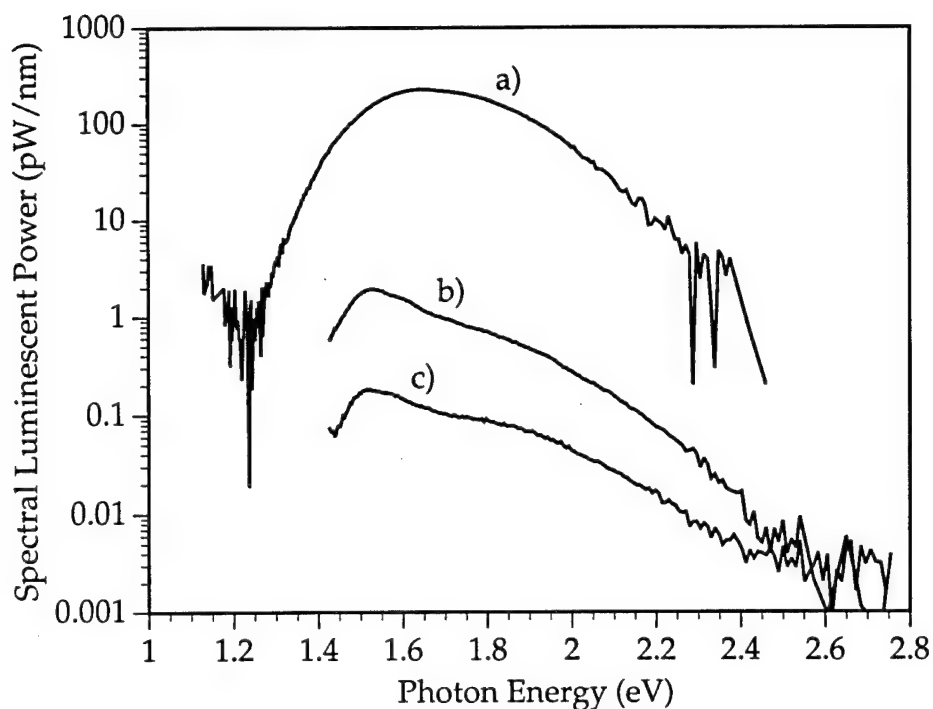


Figure 6.4 Comparison of the photoluminescence spectra of porous silicon samples subjected to a) anodization in 0.1 M KNO_3 , b) anodization in 13% aq H_2SiF_6 , and c) no post-etch treatment. The similarity between curves b) and c) indicate possible redeposition.

I show the resulting PL from these three samples in Figure 6.4. As expected, electro-oxidizing in 0.1 KNO_3 (curve (a)) blue-shifted the PL and dramatically increased its intensity. In contrast, however, anodizing in H_2SiF_6 (curve (b)) increased the PL intensity by nearly one order of magnitude while retaining the PL spectral shape of the untreated sample (curve (c)). Two competing processes may explain the similarity in spectral shape between curves (b) and (c). The first possibility is that anodizing in H_2SiF_6 simply continues the etching process, making the porous layer thicker while retaining its inherent structure sizes. The increased PL intensity would then be due to greater absorption of the incident ultraviolet light. The second possibility is that additional luminescent compounds redeposit out of the H_2SiF_6 solution onto the

surface of the porous layer, increasing the PL intensity. Since the starting porous layer is fairly thick to begin with (not measured, but probably thicker than 10 μm), we expect that all of the 365 nm excitation light is absorbed in the top layers of the porous structure. Thus, increasing its thickness by the first hypothesis, further etching, would not increase PL intensity. Based on this argument, we infer that the second hypothesis, redeposition, is a real possibility.

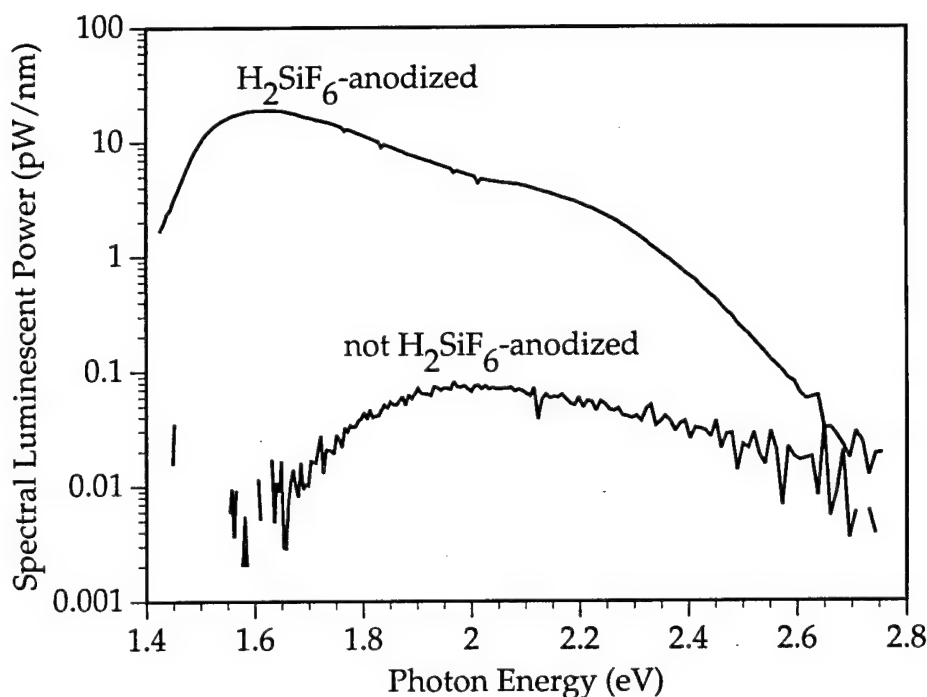


Figure 6.5 Photoluminescence spectra of two porous layers anodized at 30 mA/cm² for 10 min in 25% HF. The higher intensity spectrum at top is for a sample post anodized in ~13% H₂SiF₆, while the lower spectrum is for the sample with no post anodization.

I show additional evidence of redeposition in Figure 6.5, where I compare the PL spectra of a high porosity control sample with an identically-etched sample anodized in H₂SiF₆. The starting porous layers were formed by anodizing (111)-oriented, 1-20 Ω cm p-type silicon in 25%

ethanoic HF at 30 mA/cm² for 10 min. The post-treated sample was anodized at 10 mA/cm² for 15 min. The porous layer on the control sample (not anodized in H₂SiF₆) almost completely disintegrated while the sample anodized in H₂SiF₆ remained intact. We note that the PL spectral shape of the H₂SiF₆-anodized sample is similar to that of the control and H₂SiF₆-anodized samples in Figure 6.4. The fact that anodizing in H₂SiF₆ creates an additional PL peak at ~1.50-1.65 eV in this sample is consistent with redeposition of luminescent material that has PL energies of ~1.5-1.7 eV. We also note that in both Figures 6.4 and 6.5 two PL peaks are clearly visible and may be evidence of multiple PL processes.

b. Soaking Porous Silicon Layers in H₂SiF₆

Like the H₂SiF₆-anodization treatments described above, soaking porous silicon layers in H₂SiF₆ solutions also enhances PL intensity. We performed H₂SiF₆-soaking experiments on both chemically- and anodically-etched porous silicon samples.

We made four identical chemically-etched porous silicon layers by etching (100)-oriented, 10-20 Ω cm, p-type Si in the HF:H₂SO₄:NaNO₂:H₂O etchant for 15 min. One sample, the control, was etched, rinsed in deionized water, and blown dry with nitrogen. A second sample was etched and immediately transferred to an aqueous H₂SiF₆ solution for a 90 min soak. After soaking, the sample was removed, rinsed, and blown dry. The third and fourth samples were etched, rinsed, dried, and allowed to sit overnight. The next day, the third sample was immersed in H₂SiF₆, while the fourth sample was dipped in HF (1:10) for 10 min to remove the native

oxide and then transferred to the H_2SiF_6 solution. After the 90 min soaks, the samples were rinsed and dried.

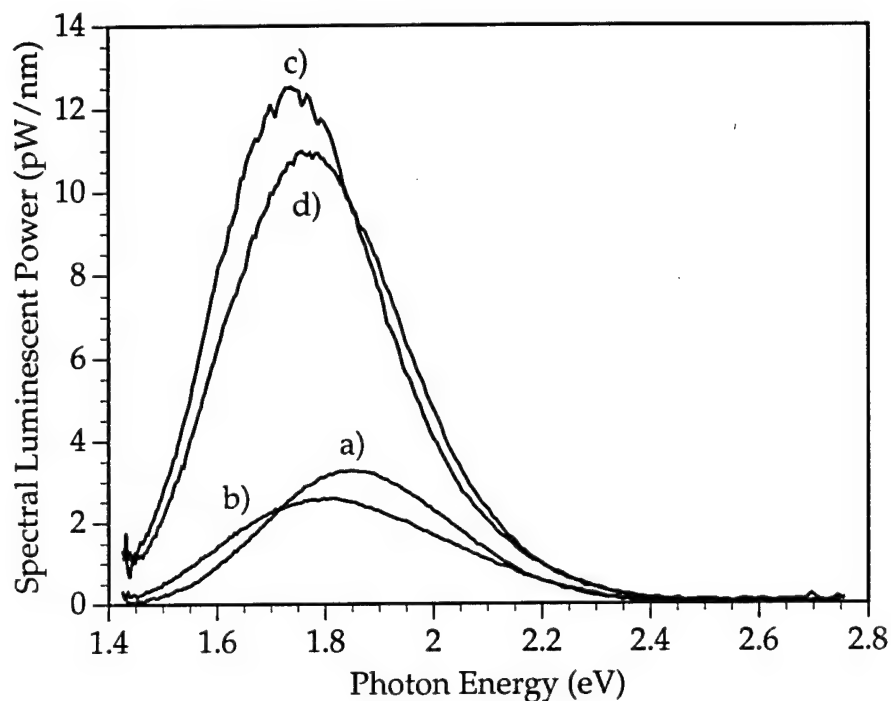


Figure 6.6. Comparison of the PL spectra of stain-etched porous silicon samples subjected to: a) no post-etch treatment, b) immediate 90 min soak in H_2SiF_6 , c) 90 min soak in H_2SiF_6 after sample sat in air for 1 day, and d) 90 min soak in H_2SiF_6 after 1 day and immediately after HF dip.

In Figure 6.6, I show the PL spectra of the four chemically-etched porous silicon samples measured. We measured the PL three days after the fluosilicic acid soaking. A clear difference, both in PL intensity and peak energy, exists between the samples soaked one day after etching and the other two samples. One possible explanation of these results is that the H_2SiF_6 reacts with and somehow augments luminescent surface species that have only formed upon oxidation of the sample in air. If this explanation is correct, then we infer from the data of Figure 6.6 that this

luminescent compound is nearly impervious to HF, which would seem to rule out oxide-related PL.

We also made four identical anodically-etched porous silicon samples by anodizing (100)-oriented, 150-250 Ω cm, p-type wafers in 25% ethanoic HF for 10 min at 5 mA/cm². The first sample was a control sample and had no post-treatment. The second and third samples sat in air for one day before being soaked in 13% aqueous H₂SiF₆ solution in the dark for 2 hrs. After soaking, the second sample was quickly dipped in water to rinse off the H₂SiF₆ and blown dry. The third sample was rinsed in flowing water for 15 min and then blown dry. Finally, the fourth sample was soaked, also after a one day exposure to air, for 2 hrs under white light illumination from a tungsten lamp (power density >100 mW/cm²). The fourth sample was given a quick rinse and blown dry. We measured the photoluminescence spectra from all samples two days after soaking.

In Figure 6.7, I show the PL spectra of the four anodically-etched samples. Soaking in H₂SiF₆ resulted in increased PL intensity with the spectra retaining nearly the same shape and peak energy as the untreated control sample. The PL intensity of the sample soaked under white-light illumination (curve (d)) was 25 times brighter than the control sample. This sample appeared to have been etched by the H₂SiF₆ as the color of the porous layer changed from blackish to yellowish. In addition, upon immersion all the samples reacted with the acid solution and formed bubbles on the porous silicon surface. If the porous layers were indeed etched by the H₂SiF₆, and if the PL is size dependent, then we should expect that the PL spectra should shift to higher energy, which apparently

is not the case. The blue PL of the sample soaked in the dark and given a quick rinse (curve (b)) is very likely due to the residual white precipitate in the H_2SiF_6 solution (see section 6.C.2). The increase in PL intensity and constant PL spectral shape for samples soaked in H_2SiF_6 appears to be evidence of the deposition, or at least activation, of luminescent surface compounds. Also, as we have previously noted concerning other samples, the PL spectra show evidence of multiple luminescence peaks.

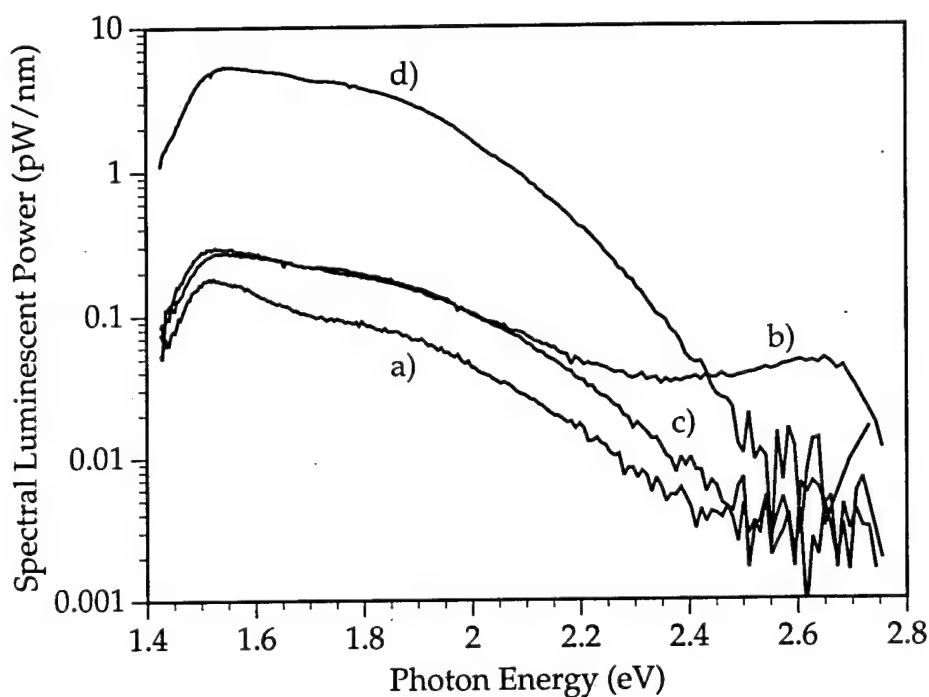


Figure 6.7. Comparison of the photoluminescence from porous silicon etched in 25% HF and subsequently subjected to: a) no post-etch treatment; b) 2 hr dark soak in H_2SiF_6 and quick rinse in water; c) 2 hr dark soak in H_2SiF_6 and 15 min rinse; and d) 2 hr soak in H_2SiF_6 under white light illumination and quick rinse.

3. Etching Silicon Through a Porous Alumina Mask

Perhaps one of the most direct ways to check for redeposition of luminescent compounds from the porous silicon etch is to force the

silicon-containing effluent through a passive and detachable porous network. In this way, if luminescent material is deposited inside the pores or at the top surface, we can remove the porous etch mask and observe luminescence similar to that from the porous silicon thereby proving the redeposition concept. We carried out this experiment using a free-standing porous alumina template, which was tens of microns thick and had ~200 nm diameter pores extending through its thickness. Because HF attacks the alumina, we could perform this experiment only with anodic etchants having low HF concentrations. In Figure 6.8, I show a diagram of the experiment.

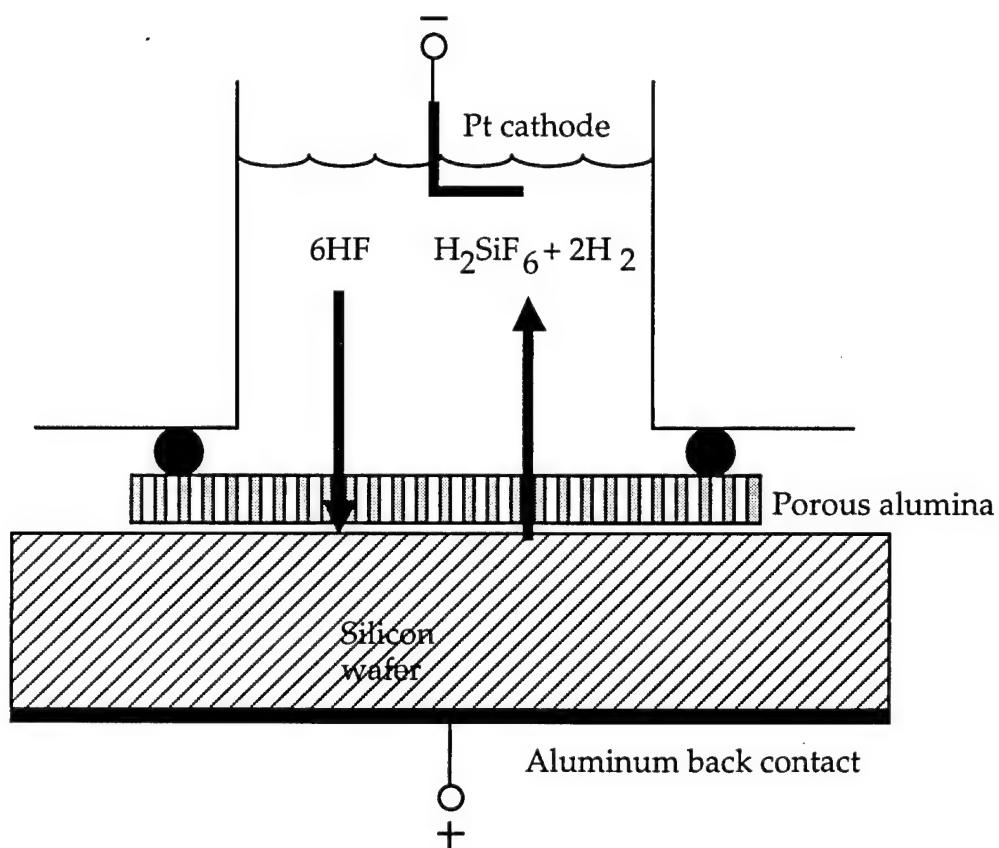


Figure 6.8. Diagram of anodic etching experiment using a porous alumina mask. The idea of the experiment is to force silicon effluent through the porous alumina structure in hopes of depositing luminescent silicon compounds in the pores.

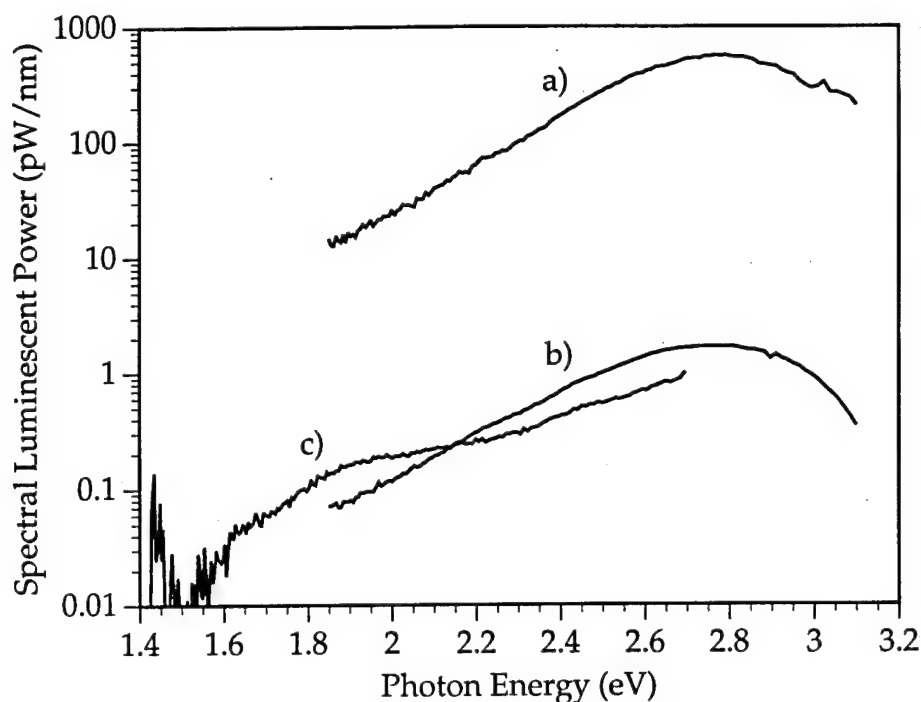


Figure 6.9. Photoluminescence spectra of: a) white crystalline-like residue on porous alumina etch mask, b) unetched porous alumina, and c) orange spot on etched porous alumina mask. Because of the similarity in spectral shape and energy between curves a) and b), the white residue on the etched alumina is probably an alumina-related compound and not from the silicon.

Using the porous alumina as an etch mask, we etched (111)-oriented p-type silicon using 1% and 5% ethanoic HF solutions. We set the current source for 50 mA/cm², but the current density was voltage-limited to only a few mA/cm². After several minutes of etching, the alumina mask showed white deposits around the rim of the etch area. As shown in Figure 6.9, this residue glowed very bright blue under UV illumination; however, because the shape of this PL spectrum matches that from unetched alumina, we must conclude that this residue is from the alumina mask. In only one sample out of five etched did we observe any evidence of orange light emission. The PL from this spot, which was less than a millimeter in diameter, faded quickly with UV illumination.

Curve (c) in Figure 6.9 shows the spectrum of the orange spot, which had a PL peak energy of ~ 2 eV and shoulders at ~ 1.6 eV and ~ 2.4 eV. Because we could not reproduce this result, and because it was only a small spot on the sample, we suspect that a chunk of porous silicon broke loose from the surface and lodged in the alumina. Thus, we conclude that this experiment yielded no solid evidence of redeposition.

D. Discussion

In all three of the experiments above, we find indirect evidence of the redeposition of luminescent compounds. Like most porous silicon experiments, however, the data are incomplete. Further XPS studies of the surfaces of these porous silicon samples might elucidate what silicon compounds are present. The possible presence of the Si^{1+} oxidation state in the stain-etched n-type samples is certainly intriguing as it may come from siloxenes, siloxanes, or silanols. XPS might also be useful in characterizing the differences in surface chemistry of the porous layers subject to post-treatments in fluosilicic acid.

As we have seen in many of the photoluminescence spectra, multiple PL peaks are evident, particularly in samples with low PL intensity. Samples with high PL intensity tend to have only one well defined peak. Thus, several competing radiative processes may occur simultaneously in porous silicon such that in samples with very bright PL, only one of these processes dominates. Further investigation of these features in the PL spectra would be very interesting. In particular, time-resolved photoluminescence measurements may reveal if these PL peaks have to a common origin or not.

E. Conclusions

I have presented experimental evidence consistent with the hypothesis that luminescent compounds redeposit out of silicon-rich etchant solutions. We investigated the luminescent residue formed on stain-etched n-type porous silicon and found it to be composed of SiO_2 , NaSiF_6 , SiC , and possibly some small fraction of the Si^{1+} silicon oxidation state. The Si^{1+} state may indicate the presence of oxygenated polymeric silicon, such as siloxene. Post-anodizing and post-soaking porous silicon layers in aqueous fluosilicic acid solution yielded greatly increased luminescence intensities, especially around the PL energies of 1.5-1.6 eV. Like many experimental characterizations of porous silicon, these results are open to other interpretations. Further investigations might address the origin of multiple PL peaks, particularly in weak PL spectra. Additional XPS study of the top surface of porous silicon subjected to various post treatments may also help clarify what silicon compounds are present and which ones correlate with observed PL peaks.

CHAPTER VII

CONCLUSIONS

A. Summary of Results

The purpose of this thesis has been to gain new understanding into the possible light emission process, or processes, in nanostructured silicon. Below, I summarize the major results of my investigations.

I presented a luminescence model for confined amorphous silicon showing that size-dependent luminescence is predicted from the statistics of accessible states in a recombination volume. Reducing the recombination volume by spatial confinement of carriers in an amorphous semiconductor blue shifts the luminescence. This model accounts for both the localized nature and size dependence of porous silicon luminescence. We tested the validity of the confined amorphous silicon luminescence model by investigating possible size effects in anodically-etched porous a-Si:H films. We observed visible photoluminescence from these films, clearly demonstrating that crystallinity, and presumably, quantum confinement, is not required for

light emission. However, we found that photoluminescence energy remained constant with varying porosity in porous a-Si:H, which seems to be inconsistent with my model. In addition, we observed considerable structure in the temperature-dependent photoluminescence spectra from these samples, which is more consistent with luminescence from discrete defect or impurity levels.

We also investigated possible quantum confinement effects in porous crystalline silicon by measuring the electroabsorption of free-standing porous films. We found the first reported, to our knowledge, electroabsorption in porous silicon films. While a number of experimental complications make data interpretation difficult, sharp electroabsorption features in some of these spectra appear to be consistent with quantum confinement effects. More measurements are needed to understand the origin of these electroabsorption features and to deduce whether they have any correlation with photoluminescence. I am convinced that porous silicon is an extremely complex material and that a simple understanding of it may not be possible; the variety of results from electroabsorption measurements on different porous silicon samples may be evidence of that.

We investigated the hypothesis that luminescent amorphous silicon compounds redeposit onto the porous silicon surface during etching. N-type porous silicon produced in depleted chemical etchant solution had a cream-colored residue on the surface that glowed bright orange under ultraviolet light illumination. Using x-ray photoelectron spectroscopy, we found evidence of the Si^{1+} oxidation state, which may be due to siloxene, in this residue. Enhancement of the photoluminescence

from porous silicon layers anodized or soaked in H_2SiF_6 after etching is also consistent with redeposition. We conclude that redeposition likely occurs in porous silicon, but further investigation is certainly needed to confirm our findings.

Finally, we found some other interesting effects, which we did not have time to explore further. In Appendix C, I present the results of temperature-dependent photoluminescence from chemically-etched porous microcrystalline silicon films. We observed an anomalous red-shift in the photoluminescence peak energy with decreasing temperature from boron-doped and intrinsic porous microcrystalline silicon samples. As with the porous amorphous silicon, the observed red shifts may be due to several competing luminescence processes. In Appendix D, I show the photoluminescence spectra resulting from AC etching of porous silicon layers. The photoluminescence peak energy and intensity are highly frequency-dependent. One possible explanation for this effect is the cathodic injection of electronic holes via H^+ ion interaction with the porous surface followed by anodic etching of the positively-charged silicon surface.

B. Suggestions for Future Research

I would like to have pursued my studies into the light emission mechanisms from porous and nanostructured silicon further. Many of my results were more ambiguous than I had hoped they would be, and so I think my contributions to the understanding of porous silicon were incremental. I believe that much larger gains in understanding porous and nanostructured silicon could be achieved by pursuing some of the

investigations in this thesis further. Below, I suggest some directions for future research based on my findings.

1. Porous Amorphous Silicon

The correlation of photoluminescence energy and intensity with boron concentration, but not with porosity, in porous a-Si:H films is quite interesting. One possible explanation for these results is that boron introduces microvoids into the morphology of the starting amorphous silicon layer. Since silicon bonds of the surfaces of these voids might tend to be more strained than bonds in the interior silicon network, anodic etching would conceivably proceed along the microvoids faster than it would into the silicon network. Thus, the density and sizes of microvoids in the starting layer may determine, more so than etching current and etchant HF concentration, the nanostructure of the porous a-Si:H layer. Small-angle x-ray scattering measurements may reveal whether this hypothesis is accurate.

2. Electroabsorption Measurements of Porous Silicon

The electroabsorption studies of Chapter V, perhaps more than any other investigation in this thesis, are worth pursuing. The sharp electroabsorption features exhibited by several samples are particularly fascinating, as they could very possibly be due to band-edge electroabsorption from quantum confined silicon crystallites. Further investigation into the voltage dependence of these features, as well as correlations with photoluminescence would almost certainly be fruitful. I highly recommend a modified experiment, designed to minimize optical

scattering effects in the measurement, such as using an integrating sphere or photothermal deflection spectroscopy.

3. XPS Studies of Porous Silicon Surfaces

X-ray photoelectron spectroscopy (XPS) is an extremely powerful probe of surface chemistry. As such, further XPS measurements of porous silicon surfaces may reveal the presence of possibly luminescent silicon compounds, such as siloxene. These measurements could be made on samples subjected to post-etch treatments to see if correlations exist between photoluminescence intensity and surface molecular compounds.

"I was relieved to be able to answer promptly. I said, 'I don't know.'"

- Mark Twain

REFERENCES

Handbook of X-ray Photoelectron Spectroscopy (Perkin-Elmer Corporation).

J. Luminescence 57 (1993).

Materials Research Society 1994 Fall Meeting, Boston, MA, 358, *Microcrystalline and Nanocrystalline Semiconductors* (Materials Research Society, 1994).

Thin Solid Films 255 (1995).

Adler, D., "Chemistry and Physics of Covalent Amorphous Semiconductors," Chap. in *Physical Properties of Amorphous Materials*, D. Alser *et al.*, Eds., (Plenum Publishing Corporation, 1985) pp. 5-103.

Augustine, B.H., Y.Z. Hu, E.A. Irene and L.E. McNeil, "Real-Time Ellipsometry Study of the Annealing of Luminescent Amorphous Silicon-Rich Silicon Oxynitride Thin Films," Appl. Phys. Lett. (1995a).

Augustine, B.H., E.A. Irene, Y.J. He, K.J. Price, L.E. McNeil, K.N. Christensen and D.M. Maher, "Visible Light Emission from Thin Films Containing Si, O, N, and H," J. Appl. Phys. (1995b).

Bao, X.-M. and H.-Q. Yang, "Control of porous silicon luminescent pattern formation by ion implantation," Appl. Phys. Lett. 63, 2246-2247 (1993).

Brandt, M.S., H.D. Fuchs, M. Stutzmann, J. Weber and M. Cardona, "The Origin of Visible Luminescence from "Porous Silicon": A New Interpretation," Solid State Comm. 81, 307 (1992).

Brandt, M.S. and M. Stutzmann, "Triplet excitons in porous silicon and siloxene," Solid State Comm. 93, 473-477 (1995).

Brus, L., "Luminescence of Silicon Materials: Chains, Sheets, Nanocrystals, Nanowires, Microcrystals, and Porous Silicon," J. Phys. Chem. 98, 3575 (1994).

Budavari, S., M.J. O'Neil, A. Smith and P.E. Heckleman, *The Merck Index* (Merck & Co., Inc., Rahway, N. J., 1989).

Bustarret, E., J. Cali, Y. Cros, M. Brunel, I. Mihalcescu and M. Ligeon, "Preparation and properties of anodized amorphous silicon," Journal of Non-Crystalline Solids 164-166, 937-940 (1993a).

Bustarret, E., M. Ligeon, J.C. Bruyère, F. Muller, R. Hérino, F. Gaspard, L. Ortega and M. Stutzmann, "Visible light emission at room temperature from anodized plasma-deposited silicon thin films," *Appl. Phys. Lett.* **61**, 1552 (1992a).

Bustarret, E., M. Ligeon and L. Ortéga, "Visible light emission at room temperature from partially oxidized amorphous silicon," *Solid State Comm.* **83**, 461-464 (1992b).

Bustarret, E., M. Ligeon and M. Rosenbauer, "Anodized Amorphous Silicon: Present Status," *Physica Status Solidi (b)* **190**, 111-116 (1995).

Bustarret, E., I. Mihalcescu, M. Ligeon, R. Romestain, J.C. Vial and F. Madéore, "Comparison of room temperature photoluminescence decays in anodically oxidized crystalline and X-ray-amorphous porous silicon," *J. Luminescence* **57**, 105-109 (1993b).

Butcher, P.N. and D. Cotter, *The Elements of Nonlinear Optics*, (Cambridge University Press, Cambridge, U. K., 1990).

Canham, L., "Silicon optoelectronics at the end of the rainbow?," *Physics World March*, 4 (1992).

Canham, L., "Progress Toward Crystalline-Silicon-Based Light-Emitting Diodes," *MRS Bulletin July*, 22 (1993).

Canham, L.T., "Silicon quantum wire array fabrication by electrochemical and chemical dissolution of wafers," *Appl. Phys. Lett.* **57**, 1046-1048 (1990).

Carius, R., R. Fischer, E. Hozenkämpfer and J. Stuke, "Photoluminescence in the amorphous system SiO_x," *J. Appl. Phys.* **52**, 4241-4243 (1981).

Carlos, W.E. and S.M. Prokes, "The EX defect center in porous silicon," *J. Appl. Phys.* **78**, 2129-2131 (1995).

Chester, M. and L. Fritsche, "Phonon-Assisted Electroabsorption," *Physical Review* **139**, A518-A525 (1965).

Collins, R.W., M.A. Paesler and W. Paul, "The temperature dependence of photoluminescence in a-Si:H alloys," *Solid State Comm.* **34**, 833-836 (1980).

Cotter, D. and H.P. Girdlestone, "Electroabsorption by semiconductor microcrystallites in glass: observation of Franz-Keldysh oscillations," *Electronics Letters* **26**, 183-184 (1990).

Dahn, J.R., B.M. Way, E.W. Fuller, W.J. Weydanz, J.S. Tse, D.D. Klug, T.V. Buuren and T. Tiedje, "X-ray diffraction and x-ray absorption studies of porous silicon, siloxene, heat-treated siloxene, and layered polysilane," J. Appl. Phys. **75**, 1946 (1994).

Delerue, C., M. Lannoo and G. Allan, "Theory of the luminescence of porous silicon," J. Luminescence **57**, 249 (1993).

Dunstan, D.J. and F. Boulitrop, "Photoluminescence in hydrogenated amorphous silicon," Phys. Rev. B **30**, 5945 (1984).

Estes, M.J., L.R. Hirsch, S. Wichart and G. Model, "Investigation of the Visible Photoluminescence from Anodized a-Si:H and a-Si:C:H Films," Unpublished (1995).

Fathauer, R.W., T. George, A. Ksendzov and R.P. Vasquez, "Visible luminescence from silicon wafers subjected to stain etches," Appl. Phys. Lett. **60**, 995 (1992).

Galbraith, I. and B. Ryvkin, "Empirical determination of the electroabsorption coefficient in semiconductors," J. Appl. Phys. **74**, 4145-4148 (1993).

Guyader, P., P. Joubert, M. Guendouz, C. Beau and M. Sarret, "Effect of grain boundaries on the formation of luminescent porous silicon from polycrystalline silicon films," Appl. Phys. Lett. **65**, 1787-1789 (1994).

Higa, K., T. Asano and T. Miyasato, "Variation of Photoluminescence Properties of Stain-Etched Si with Crystallinity of Starting Polycrystalline Si Films," Jpn. J. Appl. Phys. **33**, L1733-L1736 (1994).

Himpsel, F.J., F.R. McFeely, A. Taleb-Ibrahimi, J.A. Yarmoff and G. Hollinger, "Microscopic structure of the SiO₂/Si interface," Phys. Rev. B **38**, 6084-6096 (1988).

Hollingsworth, R.E., M.J. Estes, C. DeHart and P.K. Bhat, "Visible photoluminescence from plasma deposited nanocrystalline silicon thin films," NANO 3: Third International Conference on Nanometer-scale Science and Technology, Denver, CO, (American Vacuum Society) (1994).

Jung, K.H., S. Shih, D.L. Kwong, C.C. Cho and B.E. Gnade, "Visible photoluminescence from porous Si formed by annealing and chemically etching amorphous Si," Appl. Phys. Lett. **61**, 2467 (1992).

Kalkhoran, N.M., F. Namavar and H.P. Maruska, "Optoelectronic applications of porous polycrystalline silicon," Appl. Phys. Lett. **63**, 2661 (1993).

Kanemitsu, Y., "Visible photoluminescence from oxidized Si nanometer-sized spheres: Exciton confinement on a spherical shell," *Phys. Rev. B* **48**, 4883 (1993a).

Kanemitsu, Y., "Luminescence properties of nanometer-sized Si crystallites: Core and surface states," *Phys. Rev. B* **49**, 16845 (1994).

Kanemitsu, Y., K. Suzuki, S. Kyushin and H. Matsumoto, "Visible photoluminescence from silicon-backbone polymers," *Phys. Rev. B* **51**, 13103-13110 (1995).

Kanemitsu, Y., H. Uto, Y. Masumoto, T. Matsumoto, T. Fitago and H. Mimura, "Microstructure and optical properties of free-standing porous silicon films: Size dependence of absorption spectra in Si nanometer-sized crystallites," *Phys. Rev. B* **48**, 2827-2830 (1993b).

Kelly, M.T., J.K.M. Chun and A.B. Bocarsly, "High efficiency chemical etchant for the formation of luminescent porous silicon," *Appl. Phys. Lett.* **64**, 1693 (1994).

Kemp, M., "Is thermalization due to electronic self-trapping?," 1995 Materials Research Society Spring Meeting, San Francisco, CA, (Materials Research Society) (1995).

Knights, J.C., "Growth morphology and defects in plasma-deposited a-Si:H films," *Journal of Non-Crystalline Solids* **35 & 36**, 159-170 (1980).

Koch, F., V. Petrova-Koch and T. Muschik, "The luminescence of porous Si: the case for the surface state mechanism," *J. Luminescence* **57**, 271 (1993).

Kohno, K., Y. Osaka, F. Toyomura and H. Katayama, "Photoluminescence of Si Microcrystals Embedded in SiO₂ Glass Films," *Jpn. J. Appl. Phys.* **33**, 6616-6622 (1994).

Lazarouk, S., S. Katsuba, N. Kazuchits, G.D. Cesare, S.L. Monica, G. Maiello, E. Proverbio and A. Ferrari, "Fabrication of photoluminescent amorphous pillar silicon structures," *Microcrystalline and Nanocrystalline Semiconductors*, Boston, MA, 358, *Materials Research Society Symposia Proceedings* (Materials Research Society) p.93-97 (1994).

Lehmann, V. and U. Gösele, "Porous silicon formation: A quantum wire effect," *Appl. Phys. Lett.* **58**, 856-858 (1990).

Lehmann, V., F. Hofmann, F. Möller and U. Grüning, "Resistivity of porous silicon: a surface effect," *Thin Solid Films* **255**, 20-22 (1995).

Lin, J., L.Z. Zhang, Y.M. Huang, B.R. Zhang and G.G. Qin, "Photoluminescence of Sm doped porous silicon -- evidence for light emission through luminescence centers in SiO₂ layers," Appl. Phys. Lett. **64**, 3282 (1994).

Littau, K.A., P.J. Szajowski, A.J. Muller, A.R. Kortan and L.E. Brus, "A Luminescent Silicon Nanocrystal Colloid via a High-Temperature Aerosol Reaction," J. Phys. Chem. **97**, 1224 (1993).

Matsumoto, T., J. Takahashi, T. Tamaki, T. Futagi and Y. Kanemitsu, "Blue-green luminescence from porous silicon carbide," Appl. Phys. Lett. **64**, 226 (1994).

Miller, D.A.B., D.S. Chemla and S. Schmitt-Rink, "Relation between electroabsorption in bulk semiconductors and in quantum wells: The quantum-confined Franz-Keldysh effect," Phys. Rev. B **33**, 6976-6982 (1986).

Miyazaki, S., K. Sakamoto, K. Shiba and M. Hirose, "Photoluminescence from anodized and thermally oxidized porous germanium," Thin Solid Films **255**, 99-102 (1995).

Nassiopoulos, A.G., S. Grigoropoulos, E. Gogolides and D. Papadimitriou, "Visible luminescence from one- and two-dimensional silicon structures produced by conventional lithographic and reactive ion etching techniques," Appl. Phys. Lett. **66**, 1114-1116 (1995).

Noguchi, N., K. Suemune, M. Yamanishi, G.C. Jua and N. Otsuka, "Study of Luminescent Region in Anodized Porous Silicons by Photoluminescence Imaging and Their Microstructures," Jpn. J. Appl. Phys. **31**, L490-L493 (1992).

Ookubo, N., "Depth-dependent porous silicon photoluminescence," J. Appl. Phys. **74**, 6375 (1993).

Pankove, J.I., *Optical Processes in Semiconductors*, (Dover Publications, Inc., New York, 1971).

Pankove, J.I., "Silicon, Hydrogenated Amorphous," Chap. in *Encyclopedia of Physical Science and Technology*, (Academic Press, Inc., 1987) pp. 647-658.

Perez, J.M., J. Villalobos, P. McNeill, J. Prasad, R. Cheek, J. Kelber, J.P. Estrera, P.D. Stevens and R. Glosser, "Direct evidence for the amorphous silicon phase in visible photoluminescent porous silicon," Appl. Phys. Lett. **61**, 563 (1992).

Peyghambarian, N., S. Koch and A. Mysyrowicz, *Introduction to Semiconductor Optics*, (Prentice-Hall, Inc., Englewood Cliffs, New Jersey, 1993).

Prokes, S.M., W.E. Carlos and O.J. Glembocki, "Defect-based model for room-temperature visible photoluminescence in porous silicon," *Phys. Rev. B* 50, 17093-17096 (1994).

Prokes, S.M., J. J. A. Freitas and P.C. Searson, "Microluminescence depth profiles and annealing effects in porous silicon," *Appl. Phys. Lett.* 60, 3295 (1992).

Risbud, S.H., L.-C. Liu and J.F. Shackelford, "Synthesis and luminescence of silicon remnants formed by truncated glassmelt-particle reaction," *Appl. Phys. Lett.* 63, 1648 (1993).

Rüter, D., T. Kunze and W. Bauhofer, "Blue light emission from silicon surfaces prepared by spark-erosion and related techniques," *Appl. Phys. Lett.* 64, 3006 (1994).

Saeta, P.N. and A.C. Gallagher, "Photoluminescence of a single-crystal silicon quantum well," *Materials Research Society Fall Meeting*, Boston, MA, 358, *Microcrystalline and Nanocrystalline Semiconductors* (Materials Research Society) p.981-986 (1994a).

Saeta, P.N. and A.C. Gallagher, "Visible Luminescence from Single Crystal-Silicon Quantum Wells," *J. Appl. Phys.* 77, 4639-4642 (1994b).

Sagnes, I., A. Halimaoui, G. Vincent and P.A. Badoz, "Optical absorption evidence of a quantum size effect in porous silicon," *Appl. Phys. Lett.* 62, 1155-1157 (1992).

Seo, Y.H., K.S. Nahm, M.H. An, E.-K. Suh, Y.H. Lee, K.B. Lee and H.J. Lee, "Formation Mechanism and Pore Size Control of Light-Emitting Porous Silicon," *Jpn. J. Appl. Phys.* 33, 6425-6431 (1994).

Shih, S., K.H. Jung, T.Y. Hsieh, J. Sarathy, J.C. Campbell and D.L. Kwong, "Photoluminescence and formation mechanism of chemically etched silicon," *Appl. Phys. Lett.* 60, 1863 (1992).

Soref, R.A. and B.R. Bennett, "Electrooptical Effects in Silicon," *IEEE J. Quant. Elec.* QE-32, 123-129 (1987).

Street, R.A., "Luminescence and recombination in hydrogenated amorphous silicon," *Advances in Physics* 30, 593-676 (1981).

Street, R.A., "Luminescence in a-Si:H," Chap. 7, in *Semiconductors and Semimetals*, J. Pankove Ed., (Academic Press, New York, 1984) pp. 197-244.

Takagi, H., H. Ogawa, Y. Yamazaki, A. Ishizaki and T. Nakagiri, "Quantum size effects on photoluminescence in ultrafine Si particles," *Appl. Phys. Lett.* **56**, 2379 (1990).

Takeda, K. and K. Shiraishi, "Electronic structure of Si-skeleton materials," *Phys. Rev. B* **39**, 11028 (1989).

Takemoto, K., Y. Nakamura and O. Nittono, "Microstructure and Crystallinity of N-Type Porous Silicon," *Jpn. J. Appl. Phys.* **33**, 6432-6436 (1994).

Tiedje, T., "Amorphous semiconductor multilayer structures: Interface and layer thickness effects in photoluminescence," *Materials Issues in Applications of Amorphous Silicon Technology*, San Francisco, CA, 49, *Materials Research Society Symposia Proceedings* (Materials Research Society, Pittsburgh) p.121-125 (1985a).

Tiedje, T., B. Abeles and B.G. Brooks, "Energy Transport and Size Effects in the Photoluminescence of Amorphous-Germanium/Amorphous-Silicon Multilayer Structures," *Phys. Rev. Lett.* **54**, 2545-2548 (1985b).

Tsai, C., K.-H. Li, D.S. Kinosky, R.-Z. Qian, T.-C. Hsu, J.T. Irby, S.K. Banerjee, A.F. Tasch, J.C. Campbell, B.K. Hance and J.M. White, "Correlation between silicon hydride species and the photoluminescence intensity of porous silicon," *Appl. Phys. Lett.* **60**, 1700 (1992).

Tsang, J.C., M.A. Tischler and R.T. Collins, "Raman scattering from H or O terminated porous Si," *Appl. Phys. Lett.* **60**, 2279-2281 (1992).

Vasquez, R.P., R.W. Fathauer, T. George and A. Ksendzov, "Electronic structure of light-emitting porous Si," *Appl. Phys. Lett.* **60**, 1004 (1992).

Vial, J.C., A. Bsiesy, F. Gaspard, R. Hérino, M. Ligeon, F. Muller, R. Romestain and R.M. Macfarlane, "Mechanism of visible-light emission from electro-oxidized porous silicon," *Phys. Rev. B* **45**, 14171 (1992).

von Behren, J., K.B. Ücer, L. Tsybeskov, J.V. Vandyshv and P.M. Fauchet, "Properties of ultrathin films of porous silicon," *J. Vac. Sci. Tech. B* **13**, 1225-1229 (1995).

Walker, C.M., "Preparation of Hydrogenated Amorphous Silicon and its Characterization by Transient Photoconductivity," PhD, University of Colorado, 1992.

Weiser, G., U. Dersch and P. Thomas, "Polarized electroabsorption spectra of amorphous semiconductors," *Philos. Mag. B* **57**, 721-735 (1988).

Wendland, P.H. and M. Chester, "Electric field effects on indirect optical transitions in silicon," Phys. Rev. **140**, 1384-1390 (1965).

Wilson, W.L., P.F. Szajowski and L.E. Brus, "Quantum Confinement in Size-Selected, Surface-Oxidized Silicon Nanocrystals," Science **262**, 1242 (1993).

Xie, Y.H., M.S. Hybertsen, W.L. Wilson, S.A. Ipri, G.E. Carver, W.L. Brown, E. Dons, B.E. Weir, A.R. Kortan, G.P. Watson and A.J. Liddle, "Absorption and luminescence studies of free-standing porous silicon films," Phys. Rev. B **49**, 5386-5397 (1994).

Yakimov, A.I., N.P. Stepina, A.V. Dvurechenskii and L.A. Scherbakova, "Low-dimensional hopping conduction in porous amorphous silicon," Physica B **205**, 298-304 (1995).

Zaidi, S.H., A.-S. Chu and S.R.J. Brueck, "Scalable Fabrication and Optical Characterization of nm Si Structures," Materials Research Society 1994 Fall Meeting, Boston, MA, 358, *Microcrystalline and Nanocrystalline Semiconductors* (Materials Research Society) p.957-968 (1994).

BIBLIOGRAPHY

Adler, D., "Chemistry and Physics of Covalent Amorphous Semiconductors," Chap. in *Physical Properties of Amorphous Materials*, D. Alser et al. Eds., (Plenum Publishing Corporation, 1985) pp. 5-103.

Bustarret, E., M. Ligeon and L. Ortéga, "Visible light emission at room temperature from partially oxidized amorphous silicon," *Solid State Comm.* **83**, 461-464 (1992).

Muller, R. S., and T. I. Kamins, *Device Electronics for Integrated Circuits*, (John Wiley & Sons, New York, NY, 1986).

Pankove, J.I., *Optical Processes in Semiconductors*, (Dover Publications, Inc., New York, 1971).

Peyghambarian, N., S. Koch and A. Mysyrowicz, *Introduction to Semiconductor Optics*, (Prentice-Hall, Inc., Englewood Cliffs, New Jersey, 1993).

Soref, R.A. and B.R. Bennett, "Electrooptical Effects in Silicon," *IEEE J. Quant. Elec.* **QE-32**, 123-129 (1987).

Street, R.A., "Luminescence in a-Si:H," Chap. 7, in *Semiconductors and Semimetals*, J. Pankove Ed., (Academic Press, New York, 1984) pp. 197-244.

APPENDIX A

CONFINED AMORPHOUS SILICON MODEL: IDL

PROGRAM LISTINGS

PRO aSiH_spectra_vs_temp, Nnr, Nsnr, Einj, num_temp, num_energy, fname

```
;      Program to compute spectral shape and peak energy of the INTENSITY
;      spectra of BULK a-Si:H as a function of temperature.
```

```
;      Parameters passed:
;      Nnr = bulk defect density (per cm^3)
;      Nsnr = surface defect density (per cm^2)
;      Einj = carrier injection (excitation) energy (eV)
;      fname = filename to store data
```

COMMON a_SiH, kToc, kTov, Noc, Nov, Kc, Kv, Emg

```
;      a-Si:H material parameters
```

```
kToc = double(0.026)      ;conduction band tail energy in eV
kTov = double(0.043)      ;valence band tail energy in eV
Noc = double(1.e21)       ;conduction band mobility edge density of states in cm^-3, eV^-1
Nov = double(1.e21)       ;valence band mobility edge density of states in cm^-3, eV^-1
Kc = Noc*SQRT(2./kToc)    ;conduction band density of states constant
Kv = Nov*SQRT(2./kTov)    ;valence band density of states constant
Emg = double(1.9)         ;mobility gap in eV
Ko = double(2.e-3)        ;radiative efficiency prefactor (1/yo in R.A. Street)
To = double(23)           ;characteristic temperature in Kelvin
Nnro = double(1.e16)      ;bulk non-radiative density (cm^-3) to compute Rc
```

```
pi = double(3.1415926535)
```

```
;      Spectra calculation
```

```
delta_Ec = (Einj - Emg)/2. & delta_Ev = delta_Ec
T_min = double(40.) & T_max = double(300.)
T = (T_max-T_min)*dindgen(num_temp)/(1.*num_temp-1) + T_min
Rc = dblarr(num_temp)
Rc = (3/(4.*pi*Nnro)*alog(Ko*exp(T/To) + 1))^(1/3.)
Emin = double(0.8)
Emax = double(1.8)
spectra = dblarr(num_temp, num_energy)
maxima = dblarr(num_temp)
energy = (Emax - Emin)*dindgen(num_energy)/(1.*num_energy-1) + Emin
vc = 4./3.*pi*Rc^3
```

```
for i = 0, num_temp-1 do begin
    spectra(i,*) = exp(-vc(i)*Nnr) * $
    spectrum(vc(i), delta_Ec, delta_Ev, Emin, Emax, num_energy)
    max_val = max(spectra(i,*), index)
    maxima(i) = energy(index)
    fwhm_val(i) = FWHM(spectra(i,*), energy)
endfor
```

```
openw, 1, 'Power Mac HD:Mike:a-SiH PL Model:Data:' + fname + '.aSiH peak vs temp'
for i = 0, num_temp-1 do print, 1, format='(f8.4, 2x)', T(i), Rc(i), maxima(i)
close, 1
```

```

openw, 1, 'Power Mac HD:Mike:a-SiH PL Model:Data:' + fname + '.aSiH fwhm vs temp'
for i = 0, num_temp-1 do printf, 1, format='(3(f8.4, 2x))', T(i), Rc(i), fwhm_val(i)
close, 1

openw, 1, 'Power Mac HD:Mike:a-SiH PL Model:Data:' + fname + '.aSiH spectra vs temp'
or i = 0, num_energy-1 do begin
    for j = 0, num_temp-1 do printf, 1, format='(e10.4, TR2, $)', spectra(j, i)
    printf, 1, format='/'
endfor
close, 1

end

*****
PRO eff_vs_size, Nnr, Nsnr, T, num_size, fname

;
;   Program to compute radiative efficiency
;   of confined a-Si:H structures (2-d slabs, 1-d round wires, and 0-d spherical dots)
;   as a function of structure size.
;   Parameters passed:
;       Nnr = bulk defect density (per cm^3)
;       Nsnr = surface defect density (per cm^2)
;       T = Temperature (K)
;       fname = filename to store data

COMMON a_SiH, kToc, kTov, Noc, Nov, Kc, Kv, Emg

;
;   a-Si:H material parameters

kToc = double(0.026)           ;conduction band tail energy in eV
kTov = double(0.043)           ;valence band tail energy in eV
Noc = double(1.e21)            ;conduction band mobility edge density of states in cm^-3, eV^-1
Nov = double(1.e21)            ;valence band mobility edge density of states in cm^-3, eV^-1
Kc = Noc*SQRT(2./kToc)         ;conduction band density of states constant
Kv = Nov*SQRT(2./kTov)         ;valence band density of states constant
Emg = double(1.9)              ;mobility gap in eV
Ko = double(2.e-3)             ;radiative efficiency prefactor (1/yo in R.A. Street)
To = double(23)                ;characteristic temperature in Kelvin
Nnro = double(1.e16)           ;bulk non-radiative density (cm^-3) to compute Rc

pi = double(3.1415926535)

;
;   Radiative efficiency

Rc = (3/(4.*pi*Nnro)*alog(Ko*exp(T/To) + 1))^(1/3.)
Rt_min = double(5.e-8)         ;minimum size dimension in cm
Rt_max = double(5.e-5)         ;maximum size dimension in cm
slab_eff = dblarr(num_size)
wire_eff = dblarr(num_size)
dot_eff = dblarr(num_size)
Rt = 10^(alog10(Rt_min) + dindgen(num_size)/(num_size-1)*(alog10(Rt_max)-alog10(Rt_min)))
for i = 0, num_size-1 do begin
    slab_eff(i) = a_slab_eff(Rc, 2.*Rt(i), Nnr, Nsnr)
    wire_eff(i) = a_wire_eff(Rc, Rt(i), Nnr, Nsnr)
    dot_eff(i) = a_dot_eff(Rc, Rt(i), Nnr, Nsnr)
endfor

plot_oo, Rt, dot_eff, title='Radiative Efficiency of Confined a-Si:H', $
                                xtitle='Size Dimension (cm)', ytitle='Efficiency'

oplot, Rt, wire_eff
oplot, Rt, slab_eff

openw, 1, 'Power Mac HD:Mike:a-SiH PL Model:Data:' + fname + '.eff vs size'
for i = 0, num_size-1 do printf, 1, format='(4(e10.4, 4x))', $
                                Rt(i), slab_eff(i), wire_eff(i), dot_eff(i)
close, 1

end

```

PRO spectra_vs_size, Nnr, Nsnr, T, Einj, num_size, num_energy, num_dist, fname

```

:      Program to compute spectral shape and peak energy of the INTENSITY
:      spectra of confined a-Si:H structures (2-d slabs, 1-d round wires, and 0-d spherical dots)
:      as a function of structure size.
:      Parameters passed:
:          Nnr = bulk defect density (per cm^3)
:          Nsnr = surface defect density (per cm^2)
:          T = temperature (K)
:          Einj = carrier injection (excitation) energy (eV)
:          fname = filename to store data

```

COMMON a_SiH, kToc, kTov, Noc, Nov, Kc, Kv, Emg

```

;      a-Si:H material parameters

```

```

kToc = double(0.026)      ;conduction band tail energy in eV
kTov = double(0.043)      ;valence band tail energy in eV
Noc = double(1.e21)      ;conduction band mobility edge density of states in cm^-3, eV^-1
Nov = double(1.e21)      ;valence band mobility edge density of states in cm^-3, eV^-1
Kc = Noc*SQRT(2./kToc)    ;conduction band density of states constant
Kv = Nov*SQRT(2./kTov)    ;valence band density of states constant
Emg = double(1.9)        ;mobility gap in eV
Ko = double(2.e-3)        ;radiative efficiency prefactor (1/yo in R.A. Street)
To = double(23)           ;characteristic temperature in Kelvin
Nnro = double(1.e16)      ;bulk non-radiative density (cm^-3) to compute Rc

```

pi = double(3.1415926535)

```

;      Spectra calculation

```

```

Rc = (3/(4.*pi*Nnro)*alog(Ko*exp(T/To) + 1))^(1/3.)
delta_Ec = (Einj - Emg)/2. & delta_Ev = delta_Ec
Rt_min = double(5.e-8)    ;minimum size dimension in cm
Rt_max = double(5.e-5)    ;maximum size dimension in cm
Rt = 10^(alog10(Rt_min) + dindgen(num_size)/(num_size-1)*(alog10(Rt_max)-alog10(Rt_min)))
Emin = double(1.0)
Emax = double(3.0)
slab_spectra = dblarr(num_size, num_energy)
wire_spectra = dblarr(num_size, num_energy)
dot_spectra = dblarr(num_size, num_energy)
slab_max = dblarr(num_size)
wire_max = dblarr(num_size)
dot_max = dblarr(num_size)
energy = (Emax - Emin)*dindgen(num_energy)/(1.*num_energy-1) + Emin
slab_fwhm = dblarr(num_size)
wire_fwhm = dblarr(num_size)
dot_fwhm = dblarr(num_size)

```

```

for i = 0, num_size-1 do begin

```

```

    d = Rt(i)*dindgen(num_dist)/(1.*num_dist-1)
    slab_spect = dblarr(num_dist, num_energy)
    wire_spect = dblarr(num_dist, num_energy)
    dot_spect = dblarr(num_dist, num_energy)

```

```

    for j = 0, num_dist-1 do begin

```

```

        svc = vps(Rc, 2*Rt(i), d(j))
        Ks = exp(-svc*Nnr)*exp(-aps(Rc, 2*Rt(i), d(j))*Nsnr)
        slab_spect(j,*) = Ks * spectrum(svc, delta_Ec, delta_Ev, Emin, Emax, num_energy)
        print, "slab spectra ", (j+1)/(0.01*num_dist), "% done
        wvc = vcs(Rc, Rt(i), d(j))
        Kw = exp(-wvc*Nnr)*exp(-acs(Rc, Rt(i), d(j))*Nsnr)
        wire_spect(j,*) = Kw*d(j) * spectrum(wvc, delta_Ec, delta_Ev, Emin, Emax, num_energy)
        print, "wire spectra ", (j+1)/(0.01*num_dist), "% done
        dvc = vss(Rc, Rt(i), d(j))
        Kd = exp(-dvc*Nnr)*exp(-ass(Rc, Rt(i), d(j))*Nsnr)
        dot_spect(j,*) = Kd*d(j)^2 * spectrum(dvc, delta_Ec, delta_Ev, Emin, Emax, num_energy)
        print, "dot spectra ", (j+1)/(0.01*num_dist), "% done
    endfor

```

```

      for j = 0, num_energy-1 do begin
        slab_spectra(i,j) = 1.*energy(j)/Rt(i)*int_tabulated(d, slab_spect(*,j))
        wire_spectra(i,j) = 2.*energy(j)/Rt(i)^2*int_tabulated(d, wire_spect(*,j))
        dot_spectra(i,j) = 3.*energy(j)/Rt(i)^3*int_tabulated(d, dot_spect(*,j))
      endfor

      max_val = max(slab_spectra(i,*), index)
      slab_max(i) = energy(index)
      max_val = max(wire_spectra(i,*), index)
      wire_max(i) = energy(index)
      max_val = max(dot_spectra(i,*), index)
      dot_max(i) = energy(index)
      slab_fwhm(i) = FWHM(slab_spectra(i,*), energy)
      wire_fwhm(i) = FWHM(wire_spectra(i,*), energy)
      dot_fwhm(i) = FWHM(dot_spectra(i,*), energy)
      print, (i+1)/(0.01*num_size), '% done. Size = ', Rt(i)
    endfor

    openw, 1, 'Power Mac HD:Mike:a-SiH PL Model:Data:' + fname + '.peak vs size'
    for i = 0, num_size-1 do printf, 1, format='(e10.4, 2x, 3(f8.4, 2x))', Rt(i), slab_max(i), wire_max(i), dot_max(i)
    close, 1

    openw, 1, 'Power Mac HD:Mike:a-SiH PL Model:Data:' + fname + '.fwhm vs size'
    for i = 0, num_size-1 do printf, 1, format='(e10.4, 2x, 3(f8.4, 2x))', Rt(i), slab_fwhm(i), wire_fwhm(i), dot_fwhm(i)
    close, 1

    openw, 1, 'Power Mac HD:Mike:a-SiH PL Model:Data:' + fname + '.slab spectra vs siz'
    openw, 2, 'Power Mac HD:Mike:a-SiH PL Model:Data:' + fname + '.wire spectra vs siz'
    openw, 3, 'Power Mac HD:Mike:a-SiH PL Model:Data:' + fname + '.dot spectra vs size'
    for i = 0, num_energy-1 do begin
      for j = 0, num_size-1 do begin
        printf, 1, format='(e10.4, TR2, $)', slab_spectra(j, i)
        printf, 2, format='(e10.4, TR2, $)', wire_spectra(j, i)
        printf, 3, format='(e10.4, TR2, $)', dot_spectra(j, i)
      endfor
      printf, 1, format='(/)'
      printf, 2, format='(/)'
      printf, 3, format='(/)'
    endfor
    close, 1, 2, 3

  end

```

```

*****
FUNCTION Acs, Rc, Rt, d
:
:   Function to compute the area on a truncating cylinder of radius Rt
:   that intersects or truncates a capture sphere of radius Rc.
:   The truncating cylinder is centered at x=0 and the capture
:   sphere is at x=d. It is assumed that the capture sphere
:   center is inside the truncating cylinder (d<Rt) and that
:   d>0.
:
COMMON acs_int, Rc_, Rt_, d_, pi
pi = 3.1415926535
Rc_ = Rc & Rt_ = Rt & d_ = d

IF (d GE 0.) AND (d LE Rt) AND (Rc GT 0.) AND (Rt GT 0.) THEN CASE 1 OF
  (Rt GT Rc): CASE 1 OF
    (d LE Rt-Rc): A = 0.
    (d GT Rt-Rc): A = 4*Rt*NR_QROMO('acs_integrand1', 0., SQRT(Rc^2-(Rt-d)^2), EPS=1.e-3)
    ELSE: A = 0.
  ENDCASE
  (Rt LE Rc): A = 4*Rt*NR_QROMO('acs_integrand2', 0., SQRT(Rc^2-(Rt-d)^2),
EPS=1.e-3)
  ELSE: A = 0.
  ENDCASE ELSE A = 0.
RETURN, A
END

```

```

*****
FUNCTION acs_integrand1, z
COMMON acs_int, Rc_, Rt_, d_, pi
RETURN, ARCCOS((Rt_^2-Rc_^2+z^2+d_^2)/(2.*d_*Rt_))
END

```

```

*****
FUNCTION acs_integrand2, z
COMMON acs_int, Rc_, Rt_, d_, pi

rcz = SQRT(Rc_^2 - z^2)
CASE 1 OF
    (rcz LT Rt_+d_) AND (rcz+d_ GT Rt_): BEGIN
        arc_length = ARCCOS((Rt_^2-Rc_^2+z^2+d_^2)/(2.*d_*Rt_))
    END
    (rcz LT Rt_+d_) AND (rcz+d_ LE Rt_): arc_length = 0.
    (rcz GE Rt_+d_): arc_length = pi
    ELSE: arc_length = 0.
ENDCASE

RETURN, arc_length
END

```

```

*****
FUNCTION ade_integrand, r
COMMON ade_int, Rc_, Rt_, Nnr_, Nsnr_, pi
RETURN, r^2*EXP(-Vss(Rc_,Rt_,r)*Nnr_)*EXP(-Ass(Rc_,Rt_,r)*Nsnr_)
END

```

```

*****
FUNCTION Ai, Rc, Rt, d
:
:   Function to compute the area of intersection of two circles.
:   Variables passed:
:       Rc:   Capture circle radius, center at (d,0)
:       Rt:   Truncating circle radius, center at (0,0)
:       d:    Separation of circle centers
:   Returns the overlapping area, A, inside circle Rc as truncated by Rt
:   assuming d>0.
:
pi=3.1415926535
IF (Rc GT 0.) AND (Rt GT 0.) AND (d GE 0.) THEN CASE 1 OF
    (Rt GE Rc): CASE 1 OF
        (d LE Rt-Rc): A = pi*Rc^2
        (d GE Rc+Rt): A = 0.
        (d GT Rt-Rc) AND (d LT Rt+Rc): BEGIN
            xi = (Rt^2-Rc^2+d^2)/(2*d)
            A = -(d-xi)*SQRT(Rc^2 - (d-xi)^2) + Rc^2*(pi/2. - ARCSIN((d-xi)/Rc)) $
              - xi*SQRT(Rt^2 - xi^2) + Rt^2*(pi/2. - ARCSIN(xi/Rt))
        END
        ELSE: A = 0.
    ENDCASE
    (Rt LT Rc): CASE 1 OF
        (d LE Rc-Rt): A = pi*Rt^2
        (d GE Rc+Rt): A = 0.
        (d GT Rc-Rt) AND (d LT Rc+Rt): BEGIN
            xi = (Rt^2-Rc^2+d^2)/(2*d)
            A = -(d-xi)*SQRT(Rc^2 - (d-xi)^2) + Rc^2*(pi/2. - ARCSIN((d-xi)/Rc)) $
              - xi*SQRT(Rt^2 - xi^2) + Rt^2*(pi/2. - ARCSIN(xi/Rt))
        END
    ENDCASE
END

```

```

                ELSE:
                ENDCASE
            ELSE:
            ENDCASE ELSE
            RETURN, A
        END
    END
    A = 0.
    A = 0.
    A = 0.

```

FUNCTION Aps, Rc, Rt, d

```

    Function to compute the area of intersection of a capture
    sphere of radius Rc and a planar slab of width Rt. It
    is assumed that the left edge of the slab is at x=0
    and the center of the sphere is at x=d. It is also
    assumed that the center of the sphere is inside the
    the slab.
    pi = 3.1415926535
    IF (Rc GT 0.) AND (Rt GT 0.) AND (d GE 0) AND (d LE Rt) THEN CASE 1 OF
        (Rt GE 2*Rc): CASE 1 OF
            (d GE Rc) AND (d LE Rt-Rc):    A = 0.
            (d LT Rc):                      A = pi*(Rc^2 - d^2)
            (d GT Rt-Rc):                   A = pi*(Rc^2 - (Rt-d)^2)
            ELSE:                           A = 0.
            ENDCASE
        (Rt LT 2*Rc): CASE 1 OF
            (d GE Rc):                      A = pi*(Rc^2 - (Rt-d)^2)
            (d LE Rt-Rc):                   A = pi*(Rc^2 - d^2)
            (d GT Rt-Rc) AND (d LT Rc):    A = pi*(2*Rc^2 - d^2 - (Rt-d)^2)
            ELSE:                           A = 0.
            ENDCASE
        ELSE:                              A = 0.
        ENDCASE ELSE A = 0.
    RETURN, A
    END

```

FUNCTION arcos, x

```

    CASE 1 OF
        (x GT 1.): ans = 0.
        (x LT -1.): ans = 3.14159265
        ELSE:      ans = ACOS(x)
    ENDCASE
    RETURN, ans
    END

```

FUNCTION arsin, x

```

    CASE 1 OF
        (x GT 1.): ans = 3.14159265/2
        (x LT -1.): ans = -3.14159265/2
        ELSE:      ans = ASIN(x)
    ENDCASE
    RETURN, ans
    END

```

FUNCTION ase_integrand, r

```

    COMMON ase_int, Rc_, Rt_, Nnr_, Nsnr_, pi

```

```

RETURN, EXP(-Vps(Rc,Rt_r)*Nnr_)*EXP(-Aps(Rc,Rt_r)*Nsnr_)
END

```

```

FUNCTION Ass, Rc, Rt, d

```

```

:      Function to compute the area on a truncating sphere of radius Rt
:      that intersects or truncates a capture sphere of radius Rc.
:      The truncating sphere is centered at x=0 and the capture
:      sphere is at x=d. It is assumed that the capture sphere
:      center is inside the truncating sphere (d<Rt) and that
:      d>0.
:

```

```

pi = 3.1415926535
IF (d GE 0.) AND (d LE Rt) AND (Rc GT 0.) AND (Rt GT 0.) THEN CASE 1 OF
  (Rc EQ 0.): CASE 1 OF
    (d EQ 0.): A = 4*pi*Rt^2
    (d GT 0.): BEGIN
      xi = (Rt^2-Rc^2+d^2)/(2*d)
      A = 4*pi*(Rt*SIN(0.5*ARCOS(xi/Rt)))^2
      END
    ELSE: A = 0.
  ENDCASE
  (Rc LT Rt): CASE 1 OF
    (d LE Rt-Rc): A = 0.
    (d GT Rt-Rc): BEGIN
      xi = (Rt^2-Rc^2+d^2)/(2*d)
      A = 4*pi*(Rt*SIN(0.5*ARCOS(xi/Rt)))^2
      END
    ELSE: A = 0.
  ENDCASE
  (Rc GT Rt): CASE 1 OF
    (d LE Rc-Rt): A = 4*pi*Rt^2
    (d GT Rc-Rt): BEGIN
      xi = (Rt^2-Rc^2+d^2)/(2*d)
      A = 4*pi*(Rt*SIN(0.5*ARCOS(xi/Rt)))^2
      END
    ELSE: A = 0.
  ENDCASE
  ELSE: A = 0.
ENDCASE ELSE A = 0.
RETURN, A
END

```

```

FUNCTION awe_integrand, r

```

```

COMMON awe_int, Rt_, Rc_, Nnr_, Nsnr_, pi

```

```

RETURN, r*EXP(-Vcs(Rc,Rt_r)*Nnr_)*EXP(-Acs(Rc,Rt_r)*Nsnr_)
END

```

```

FUNCTION fc, E, delta_Ec, Vc

```

```

:      Function to compute the probability density of lowest energy conduction band states
:      within the capture volume Vc in a-Si:H. Given an injection energy level offset,
:      delta_Ec, from the conduction band mobility edge, the function returns the probability
:      density of the lowest energy level being at energy E below the injection level.
:

```

```

COMMON a_SiH, kToc, kTov, Noc, Nov, Kc, Kv, Emg

```

```

IF (E LT delta_Ec) THEN BEGIN
  n = nc(delta_Ec)
  n_e = nec(E, delta_Ec)

```

```

      f = (n_e/n)^(Vc*n-1)*Nc_dos(E)*Vc
ENDIF ELSE f = 0.
RETURN, f
END

```

```

*****
FUNCTION fcfv, E1
:
:   Function to compute the integrand of the convolution integral between
:   the functions fc and fv.
:
COMMON fcfv_conv, delta_Ec, delta_Ev, ED, Vc

RETURN, fc(E1, delta_Ec, Vc)*fv(delta_Ev+delta_Ec-ED-E1, delta_Ev, Vc)
END

```

```

*****
FUNCTION fv, E, delta_Ev, Vc
:
:   Function to compute the probability density of lowest energy valence band states
:   within the capture volume Vc in a-Si:H. Given an injection energy level offset,
:   delta_Ev, from the valence band mobility edge, the function returns the probability
:   density of the lowest energy level being at energy E below the injection level.
:
COMMON a_SiH, kToc, kTov, Noc, Nov, Kc, Kv, Emg

IF (E LT delta_Ev) THEN BEGIN
  n = nv(delta_Ev)
  n_e = nev(E, delta_Ev)
  f = (n_e/n)^(Vc*n-1)*Nv_dos(E)*Vc
ENDIF ELSE f = 0.
RETURN, f
END

```

```

*****
function FWHM, y, x
:
:   Compute the full width at half maximum (FWHM) of a single peaked function
:   y(x).
:
hm = 0.5 * max(y)

p = where(y GE hm)
ia = min(p)
ib = max(p)

x1a = x(ia) & x2a = x(ib-1)
y1a = y(ia) & y2a = y(ib-1)
x1b = x(ib) & x2b = x(ib+1)
y1b = y(ib) & y2b = y(ib+1)

xa = (x2a-x1a)/(y2a-y1a)*(hm - y1a) + x1a
xb = (x2b-x1b)/(y2b-y1b)*(hm - y1b) + x1b

return, xb-xa
end

```

```

*****
FUNCTION nc, delta_Ec
:
:   Function to compute the total density of states below the injection level
:   in a-Si:H. The injection energy level is E = Ec + delta_Ec, where Ec is the
:   conduction band mobility edge and delta_Ec is the injection offset.
:

```



```

COMMON a_SiH, kToc, kTov, Noc, Nov, Kc, Kv, Emg

IF (delta_Ec LE 0.) THEN BEGIN
    n_states = Noc*kToc*EXP(delta_Ec/kToc)
ENDIF ELSE
    n_states = (2/3.)*Kc*((delta_Ec+0.5*kToc)^1.5 - (0.5*kToc)^1.5) + Noc*kToc

RETURN, n_states
END

```

```

FUNCTION Nc_dos, E
:
:   Function to compute the conduction band density of states at the energy E (relative to
:   the conduction band mobility edge).
:
COMMON a_SiH, kToc, kTov, Noc, Nov, Kc, Kv, Emg

CASE 1 OF
    (E LE 0.): N = Noc*EXP(E/kToc)
    (E GT 0.): N = Kc*(E + 0.5*kToc)^0.5
    ELSE:      N = 0.
ENDCASE

RETURN, N
END

```

```

FUNCTION nec, E, delta_Ec
:
:   Function to compute the total density of states from the injection energy level
:   offset, delta_Ec, to the energy E below the injection level.
:
COMMON a_SiH, kToc, kTov, Noc, Nov, Kc, Kv, Emg

IF (E LT delta_Ec) THEN CASE 1 OF
    (delta_Ec LE 0.): n_states = Noc*kToc*(EXP(delta_Ec/kToc) - EXP(E/kToc))
    (delta_Ec GT 0.) AND (E LE 0.): BEGIN
        n_states = (2/3.)*Kc*((delta_Ec+0.5*kToc)^1.5 - (0.5*kToc)^1.5)
        n_states = n_states + Noc*kToc*(1-EXP(E/kToc))
    END
    (delta_Ec GT 0.) AND (E GT 0.): BEGIN
        n_states = (2/3.)*Kc*((delta_Ec+0.5*kToc)^1.5 - (E+0.5*kToc)^1.5)
    END
    ELSE: n_states = 0.
ENDCASE ELSE n_states = 0.
RETURN, n_states
END

```

```

FUNCTION nev, E, delta_Ev
:
:   Function to compute the total density of states from the injection energy level
:   offset, delta_Ev, to the energy E below the injection level.
:
COMMON a_SiH, kToc, kTov, Noc, Nov, Kc, Kv, Emg

IF (E LT delta_Ev) THEN CASE 1 OF
    (delta_Ev LE 0.): n_states = Nov*kTov*(EXP(delta_Ev/kTov) - EXP(E/kTov))
    (delta_Ev GT 0.) AND (E LE 0.): BEGIN
        n_states = (2/3.)*Kv*((delta_Ev+0.5*kTov)^1.5 - (0.5*kTov)^1.5)
        n_states = n_states + Nov*kTov*(1-EXP(E/kTov))
    END
    (delta_Ev GT 0.) AND (E GT 0.): BEGIN
        n_states = (2/3.)*Kv*((delta_Ev+0.5*kTov)^1.5 - (E+0.5*kTov)^1.5)
    END
    ELSE: n_states = 0.
ENDCASE ELSE n_states = 0.

```

```

RETURN, n_states
END

```

```

*****
FUNCTION nv, delta_Ev
:
:   Function to compute the total density of states below the injection energy level
:   in a-Si:H. The injection energy level is  $E = E_v + \text{delta\_Ev}$ , where  $E_v$  is the
:   conduction band mobility edge and delta_Ev is the injection offset.
:
COMMON a_SiH, kToc, kTov, Noc, Nov, Kc, Kv, Emg

IF (delta_Ev LE 0.) THEN BEGIN
    n_states = Nov*kTov*EXP(delta_Ev/kTov)
ENDIF ELSE
    n_states = (2/3.)*Kv*((delta_Ev+0.5*kTov)^1.5 - (0.5*kTov)^1.5) + Nov*kTov

RETURN, n_states
END

```

```

*****
FUNCTION Nv_dos, E
:
:   Function to compute the valence band density of states at the energy E (relative to
:   the valence band mobility edge).
:
COMMON a_SiH, kToc, kTov, Noc, Nov, Kc, Kv, Emg

CASE 1 OF
(E LE 0.): N = Nov*EXP(E/kTov)
(E GT 0.): N = Kv*(E + 0.5*kTov)^0.5
ELSE:      N = 0.
ENDCASE

RETURN, N
END

```

```

*****
FUNCTION Vcs, Rc, Rt, d
:
:   Function to compute the volume inside a capture sphere of radius Rc
:   as truncated by a cylinder of radius Rt. The center of the
:   cylinder is at x=0 and the center of the sphere is at x=d. It
:   is assumed that the center of the sphere is inside the cylinder
:   ( $d < Rt$ ) and that  $d > 0$ .
:
COMMON vcs_int, Rc_, Rt_, d_
pi = 3.1415926535
Rc_ = Rc & Rt_ = Rt & d_ = d

IF (d GE 0.) AND (d LE Rt) AND (Rc GT 0.) AND (Rt GT 0.) THEN CASE 1 OF
(Rt GE Rc): CASE 1 OF
(d LE Rt-Rc): V = (4./3.)*pi*Rc^3
(d GT Rt-Rc): V = 2*NR_QROMO('vcs_integrand', 0., Rc, EPS=1.e-3)
ELSE:         V = 0.
ENDCASE
(Rt LT Rc):   V = 2*NR_QROMO('vcs_integrand', 0., Rc, EPS=1.e-3)
ELSE:         V = 0.
ENDCASE ELSE
    V = 0.

RETURN, V
END

```

```

*****
FUNCTION vcs_integrand, z
COMMON vcs_int, Rc_, Rt_, d_

```

```
RETURN, Ai(SQRT(Rc^2-z^2), Rt, d_)
END
```

```
FUNCTION Vps, Rc, Rt, d
```

```

Function to compute the volume inside a capture sphere of
radius Rc as truncated by a planar-slab of width Rt. The
left edge of the slab is assumed to be at x=0 and
the center of the circle is at x=d. It is also
assumed that the center of the sphere is inside the
the slab.

pi = 3.1415926535
IF (Rc GT 0.) AND (Rt GT 0.) AND (d GE 0.) AND (d LE Rt) THEN CASE 1 OF
  (Rt GE 2*Rc): CASE 1 OF
    (d GE Rc) AND (d LE Rt-Rc): V = (4./3.)*pi*Rc^3
    (d LT Rc): V = pi*((Rc^2-d^2)*(d+Rc) + d*(d+Rc)^2
- (1./3.)*(d+Rc)^3)
    (d GT Rt-Rc): BEGIN
      V = pi*((Rc^2-d^2)*(Rt-d+Rc) + d*(Rt^2-(d-Rc)^2) - (1./3.)*(Rt^3-(d-Rc)^3))
    END
    ELSE: V = 0.
  ENDCASE
  (Rt LT 2*Rc): CASE 1 OF
    (d GE Rc): BEGIN
      V = pi*((Rc^2-d^2)*(Rt-d+Rc) + d*(Rt^2-(d-Rc)^2) - (1./3.)*(Rt^3-(d-Rc)^3))
    END
    (d LE Rt-Rc): V = pi*((Rc^2-d^2)*(d+Rc) + d*(d+Rc)^2 -
(1./3.)*(d+Rc)^3)
    (d GT Rt-Rc) AND (d LT Rc): V = pi*((Rc^2-d^2)*Rt + d*Rt^2 - (1./3.)*Rt^3)
    ELSE: V = 0.
  ENDCASE
ELSE: V = 0.
ENDCASE ELSE V = 0.
RETURN, V
END
```

```
FUNCTION Vss, Rc, Rt, d
```

```

Function to compute the volume inside a capture sphere of radius
Rc as truncated by another sphere of radius Rt. The center
of the truncating sphere is at x=0 while the capture sphere
center is at x=d. It is assumed that the center of the
capture sphere is inside the truncating sphere and that d>0.

pi = 3.1415926535
IF (d GE 0.) AND (d LE Rt) AND (Rc GT 0.) AND (Rt GT 0.) THEN CASE 1 OF
  (Rc LE Rt): CASE 1 OF
    (d LE Rt-Rc): V = (4./3.)*pi*Rc^3
    (d GT Rt-Rc): BEGIN
      xi = (Rt^2-Rc^2+d^2)/(2*d)
      V = pi*((Rc^2-d^2)*(xi-d+Rc) + d*(xi^2-(d-Rc)^2) - (1./3.)*(xi^3-(d-Rc)^3) $
+ Rt^2*(Rt-xi) - (1./3.)*(Rt^3-xi^3))
    END
    ELSE: V = 0.
  ENDCASE
  (Rc GT Rt): CASE 1 OF
    (d LE Rc-Rt): V = (4./3.)*pi*Rt^3
    (d GT Rc-Rt): BEGIN
      xi = (Rt^2-Rc^2+d^2)/(2*d)
      V = pi*((Rc^2-d^2)*(xi-d+Rc) + d*(xi^2-(d-Rc)^2) - (1./3.)*(xi^3-(d-Rc)^3) $
+ Rt^2*(Rt-xi) - (1./3.)*(Rt^3-xi^3))
    END
    ELSE: V = 0.
  ENDCASE
```

```
ELSE:  
ENDCASE ELSE V=0.  
RETURN, V  
END
```

V=0.

APPENDIX B

CAPTURE VOLUME AND SURFACE CAPTURE AREA EXPRESSIONS

The expressions for capture volume, V_c , and surface capture area, A_c , as functions of position within 2-d slabs, 1-d wires, and 0-d spheres are given here without derivation for a capture radius of R_c , a structure radius (or 2-d slab half-width) of R_t , and a center-to-center separation (or distance from left edge of 2-d slab) of r .

A. 2-d Planar Slabs

$$V_c = \begin{cases} \frac{4}{3}\pi R_c^3, & R_t \geq R_c, R_c \leq r \leq R_t - R_c \\ \pi \left[(R_c^2 - r^2)(r + R_c) + r(r + R_c)^2 - \frac{1}{3}(r + R_c)^3 \right], & R_t \geq R_c, r < R_c \\ \pi \left[(R_c^2 - r^2)(2R_t - r + R_c) + r(4R_t^2 - (r - R_c)^2 - \frac{1}{3}(4R_t^3 - (r - R_c)^3)) \right], & R_t \geq R_c, r > R_t - R_c \\ \pi \left[2(R_c^2 - r^2)R_t + 4rR_t^2 - \frac{8}{3}R_t^3 \right], & R_t < R_c, R_t - R_c \leq r \leq R_c \\ \pi \left[(R_c^2 - r^2)(2R_t - r + R_c) + r(4R_t^2 - (r - R_c)^2 - \frac{1}{3}(4R_t^3 - (r - R_c)^3)) \right], & R_t < R_c, r > R_c \\ \pi \left[(R_c^2 - r^2)(r + R_c) + r(r + R_c)^2 - \frac{1}{3}(r + R_c)^3 \right], & R_t < R_c, r < R_t - R_c \end{cases} \quad (B.1)$$

$$A_c = \begin{cases} 0, & R_t \geq R_c, R_c \leq r \leq R_t - R_c \\ \pi(R_c^2 - r^2), & R_t \geq R_c, r < R_c \\ \pi(R_c^2 - (2R_t - r)^2), & R_t \geq R_c, r > R_t - R_c \\ \pi(2R_c^2 - r^2 - (2R_t - r)^2), & R_t < R_c, R_t - R_c \leq r \leq R_c \\ \pi(R_c^2 - (2R_t - r)^2), & R_t < R_c, r > R_c \\ \pi(R_c^2 - r^2), & R_t < R_c, r < R_t - R_c \end{cases} \quad (B.2)$$

B. 1-d Cylindrical Wires

$$V_c = \begin{cases} \frac{4}{3}\pi R_c^2, & R_t \geq R_c, r \leq R_t - R_c \\ 2 \int_0^{R_c} A_i(\sqrt{R_c^2 - z^2}, R_t, r) dz, & R_t \geq R_c, r > R_t - R_c \\ 2 \int_0^{R_c} A_i(\sqrt{R_c^2 - z^2}, R_t, r) dz, & R_t < R_c \end{cases} \quad (\text{B.3})$$

where $A_i(r_1, r_2, d)$ is the area of intersection of two circles or radii r_1 and r_2 separated by a distance d and is defined by

$$A_i(r_1, r_2, d) = \begin{cases} \begin{cases} \left. \begin{aligned} &-(d+x_i)\sqrt{r_1^2 - (d+x_i)^2} \\ &+r_2^2 \left(\frac{\pi}{2} - \sin^{-1} \left(\frac{d-x_i}{r_1} \right) \right) \\ &-x_i\sqrt{r_2^2 - x_i^2} + r_2^2 \left(\frac{\pi}{2} - \sin^{-1} \left(\frac{x_i}{r_2} \right) \right) \end{aligned} \right\}, & \begin{aligned} &r_2 \geq r_1, \\ &r_2 - r_1 < d < r_2 + r_1 \end{aligned} \\ 0, & r_2 \geq r_1, d \geq r_2 + r_1 \\ \pi r_1^2, & r_2 \geq r_1, d \leq r_2 - r_1 \end{cases} \\ \begin{cases} \left. \begin{aligned} &-(d+x_i)\sqrt{r_1^2 - (d+x_i)^2} \\ &+r_1^2 \left(\frac{\pi}{2} - \sin^{-1} \left(\frac{d-x_i}{r_1} \right) \right) \\ &-x_i\sqrt{r_2^2 - x_i^2} + r_2^2 \left(\frac{\pi}{2} - \sin^{-1} \left(\frac{x_i}{r_2} \right) \right) \end{aligned} \right\}, & \begin{aligned} &r_2 < r_1, \\ &r_1 - r_2 < d < r_1 + r_2 \end{aligned} \\ 0, & r_2 < r_1, d \geq r_1 + r_2 \\ \pi r_2^2, & r_2 < r_1, d \leq r_1 - r_2 \end{cases} \end{cases} \quad (\text{B.4})$$

and where

$$x_i = \frac{R_t^2 - R_c^2 + r^2}{2r}. \quad (\text{B.5})$$

$$A_c = \begin{cases} 0, & R_t > R_c, r \leq R_t - R_c \\ 4R_t \int_0^{\sqrt{R_c^2 - (R_t - r)^2}} \cos^{-1} \left(\frac{R_t^2 - R_c^2 + r^2 + z^2}{2rR_t} \right) dz, & R_t > R_c, r > R_t - R_c \\ 4R_t \int_0^{\sqrt{R_c^2 - (R_t - r)^2}} L_{\text{arc}}(R_c, R_t, r) dz, & R_t \leq R_c \end{cases} \quad (\text{B.6})$$

where

$$L_{\text{arc}}(R_c, R_t, r) = \begin{cases} \cos^{-1} \left(\frac{R_t^2 - R_c^2 + r^2 + z^2}{2rR_t} \right), & \begin{cases} \sqrt{R_c^2 - z^2} < R_t + r, \\ \sqrt{R_c^2 - z^2} > R_t - r \end{cases} \\ 0, & \begin{cases} \sqrt{R_c^2 - z^2} < R_t + r, \\ \sqrt{R_c^2 - z^2} \leq R_t - r \end{cases} \\ \pi, & \sqrt{R_c^2 - z^2} \geq R_t + r \end{cases} \quad (\text{B.7})$$

C. 0-d Spherical Dots

$$V_c = \begin{cases} \frac{4}{3} \pi R_c^3, & R_c \leq R_t, r \leq R_t - R_c \\ \pi \left[\frac{1}{3} (R_c^2 - r^2) (x_i - r + R_c) + r (x_i^2 - (r - R_c)^2) - \frac{1}{3} (x_i^3 - (r - R_c)^3) + R_t^2 (R_t - x_i) - \frac{1}{3} (R_t^3 - x_i^3) \right], & R_c \leq R_t, r > R_t - R_c \\ \frac{4}{3} \pi R_t^3, & R_c > R_t, r \leq R_c - R_t \\ \pi \left[\frac{1}{3} (R_c^2 - r^2) (x_i - r + R_c) + r (x_i^2 - (r - R_c)^2) - \frac{1}{3} (x_i^3 - (r - R_c)^3) + R_t^2 (R_t - x_i) - \frac{1}{3} (R_t^3 - x_i^3) \right], & R_c > R_t, r > R_c - R_t \end{cases} \quad (\text{B.8})$$

$$A_c = \begin{cases} 4\pi R_t^2, & R_c = R_t, r = 0 \\ 4\pi R_t^2 \sin^2 \left(\frac{1}{2} \sin^{-1} \left(\frac{R_t^2 - R_c^2 + r^2}{2rR_t} \right) \right), & R_c = R_t, r > 0 \\ 0, & R_c < R_t, r \leq R_t - R_c \\ 4\pi R_t^2 \sin^2 \left(\frac{1}{2} \sin^{-1} \left(\frac{R_t^2 - R_c^2 + r^2}{2rR_t} \right) \right), & R_c < R_t, r > R_t - R_c \\ 4\pi R_t^2, & R_c > R_t, r \leq R_c - R_t \\ 4\pi R_t^2 \sin^2 \left(\frac{1}{2} \sin^{-1} \left(\frac{R_t^2 - R_c^2 + r^2}{2rR_t} \right) \right), & R_c > R_t, r > R_c - R_t \end{cases} \quad (\text{B.9})$$

APPENDIX C

ANOMALOUS TEMPERATURE DEPENDENCE OF THE PHOTOLUMINESCENCE FROM POROUS MICROCRYSTALLINE SILICON THIN FILMS

A. Sample Fabrication

Microcrystalline silicon thin films were deposited using plasma enhanced chemical vapor deposition (PECVD) by the Materials Research Group, Inc. (MRG). Films were deposited onto ground Corning 7059 glass substrates at substrate temperatures between 200-300° C. Phosphine or trimethylboron gas was added to the plasma to produce n-type or p-type layers, respectively. Microcrystallinity was obtained by using high hydrogen dilution ($\text{H}_2:\text{SiH}_4$ ratios of 15-60:1) and high frequency (110 MHz) rf plasmas. An rf power density of 50 mW/cm² was used, resulting in a deposition rate of 0.5-2.0 Å/sec. Film thicknesses prior to etching were 0.5-1.0 µm. The microcrystalline silicon films were subsequently stain etched in $\text{HF}:\text{HNO}_3:\text{H}_2\text{O}$ (1:3:5) to produce luminescent porous layers.

B. Temperature-Dependent Photoluminescence

We measured the temperature dependence of the photoluminescence (PL) peak energy from intrinsic, n-type, and p-type films. As I show in Figure C.1, the peak energy of the n-type porous films increased as temperature decreased. This trend is as we should expect in crystalline or amorphous semiconductors due to the shift of the bandgap

with temperature or in amorphous semiconductors due to the change of carrier mobility with temperature. However, intrinsic and p-type porous layers exhibited a decrease in photoluminescence peak energy as temperature decreased. This anomalous behavior is counter to our conventional wisdom and may be further evidence of multiple PL processes.

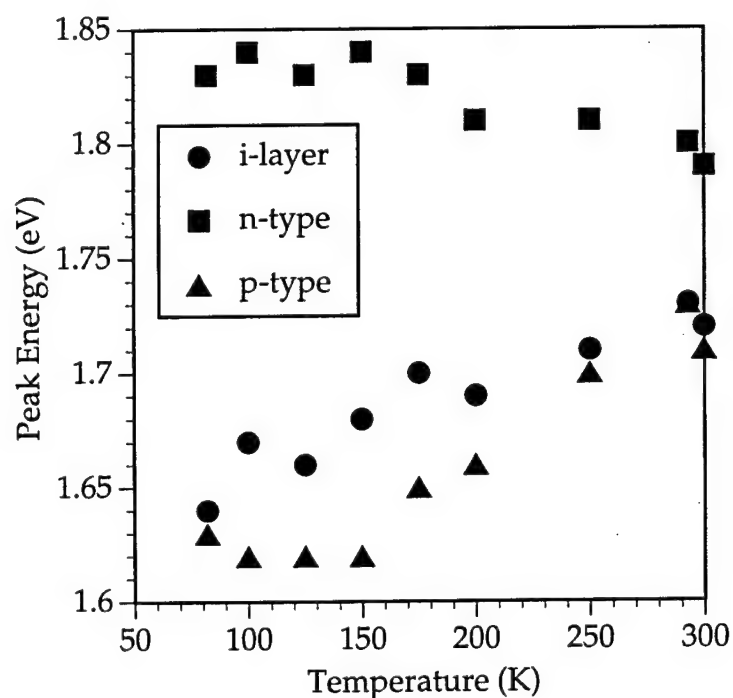


Figure C.1. Temperature dependence of the photoluminescence peak energy from porous microcrystalline silicon films as a function of doping.

APPENDIX D

SURFACE NORMAL OPTICAL MODULATION IN THIN FILM SILICON: IS IT FEASIBLE?

Michael Estes and Garret Moddel

Department of Electrical and Computer Engineering
University of Colorado, Campus Box 425
Boulder, Colorado 80309-0425
Tel: (303) 492-1889, Email: moddel@boulder.colorado.edu

I. Introduction

Unlike direct band gap materials such as GaAs, which exhibit very sharp and strong absorption at the band edge, indirect gap crystalline silicon has relatively weak band edge absorption and hence weak band edge nonlinearities[1]. Even hydrogenated amorphous silicon (a-Si:H) with its quasi-direct bandgap shows only moderate electro-optic modulation at its nominally 1.7 eV band edge[2, 3] due to disorder-induced tail states. In addition, both a-Si:H and c-Si are centrosymmetric materials so that there are no $\chi^{(2)}$ optical nonlinearities.

Silicon does, though, have some inherent advantages over conventional electro-optic materials: compatibility with conventional silicon electronics, ease of deposition over large areas, and well characterized behavior. Additionally, being an electronic material it has a potential speed advantage over liquid crystal modulators. The allure of all-silicon optoelectronics has motivated us to investigate its optical modulation potential. In the following sections we discuss basic requirements for surface-normal silicon modulators and review electro-optic modulation mechanisms in bulk and quantum confined silicon.

II. Material Requirements

The surface-normal geometry required for spatial light modulators severely limits the interaction length of light through the modulating layer. Since we do not expect the electro-optic properties of silicon to be strong, we require some resonance, either optical or electronic, to obtain sufficient modulation contrast.

A number of optically resonant structures have been proposed for III-V optical modulators. One promising structure is the active distributed Bragg reflector[4] in which the refractive index and absorption in alternating $\lambda/4$ layers are modulated to change reflectivity or transmittivity. Figure 1 shows calculated reflection and transmission change for a 50 period a-Si:H or c-Si film in which the index of refraction in alternating $\lambda/4$ layers are modified by an amount $\Delta n = \Delta k$. The unmodulated layers are assumed to be of the same material (a-Si:H or c-Si). We assume subband gap wavelengths of 0.87 μm and 1.55 μm for the a-Si:H and c-Si, respectively. We see that we need electro-optic effects with $\Delta n, \Delta k > 10^{-3}$ to realize useful modulation contrast. In the following section, we will review electro-optic effects in silicon to assess the feasibility of obtaining such modulation.

III. Optical Modulation Mechanisms in Silicon

A. Electric Field Effects

Under an applied electric field, carriers in a crystalline semiconductor may tunnel some distance into the band gap. This gives rise to an exponential absorption tail below the band edge and an oscillatory absorption above the band edge due to the spatial overlap of electron and hole wave functions. This phenomenon is known as the Franz-Keldysh effect. The largest absorption change occurs for light very near the band gap energy. The Franz-Keldysh induced change in refractive index, Δn , and absorption coefficient, $\Delta\alpha$, for c-Si versus applied field are shown in Figure 2. The data shown in the Figure were extrapolated from results given by Soref and Bennett[5]. At the dielectric breakdown field of around 4×10^5 V/cm, $\Delta n \approx 10^{-3}$ and $\Delta\alpha \approx 50 \text{ cm}^{-1}$ for $1.07 \text{ }\mu\text{m}$ light. The Franz-Keldysh effect in a-Si:H appears to be negligible[3].

Under high electric fields, the polarization response of a material becomes nonlinear. For centrosymmetric materials under an applied DC electric field the complex index of refraction changes quadratically with field by an amount

$$\Delta \hat{n}_x \equiv \hat{n}_{x0} + \frac{1}{2} \hat{\chi}^{(3)} |E_x^{dc}|^2$$

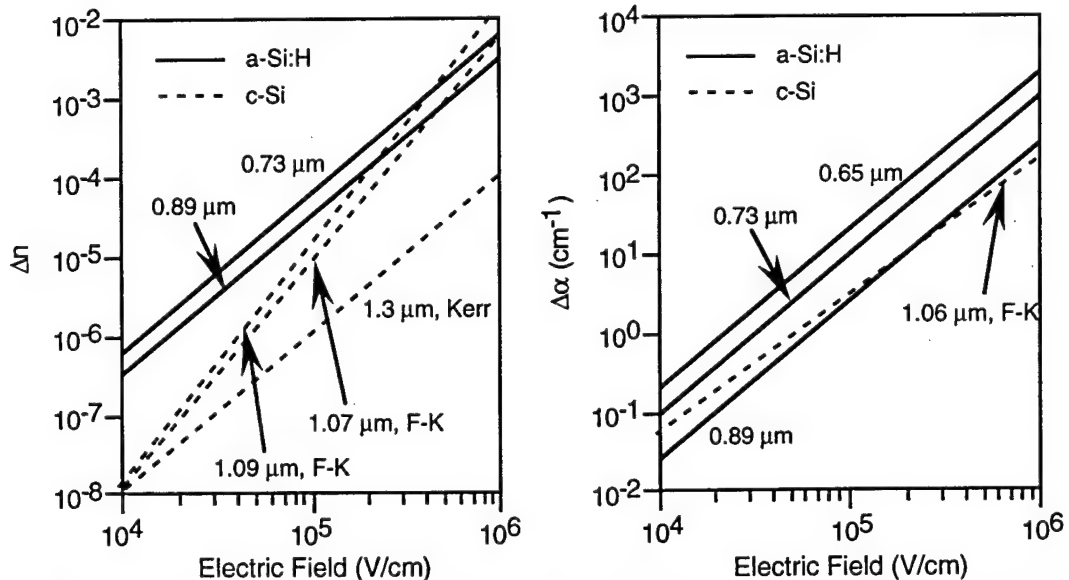


Figure 2. Electric field-induced change in the optical properties of bulk a-Si:H[2, 3] and c-Si.[5] Effects in a-Si:H are due to DC Kerr effect while those in c-Si are due to both DC Kerr and Franz-Keldysh (F-K) effects.

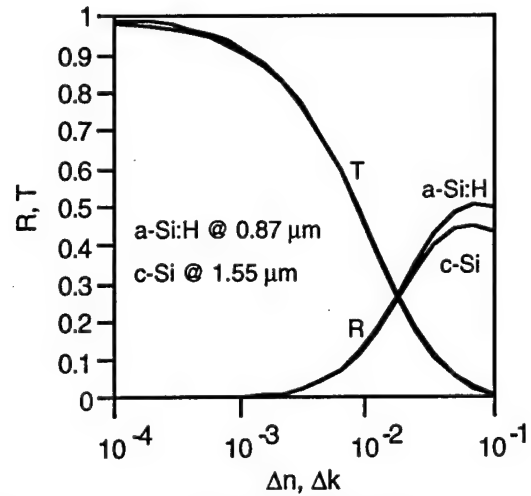


Figure 1. Calculated reflectivity (R) and transmittivity (T) of a-Si:H at $0.87 \text{ }\mu\text{m}$ and c-Si at $1.55 \text{ }\mu\text{m}$ in which alternating $\lambda/4$ layers are modified by $\Delta n = \Delta k$.

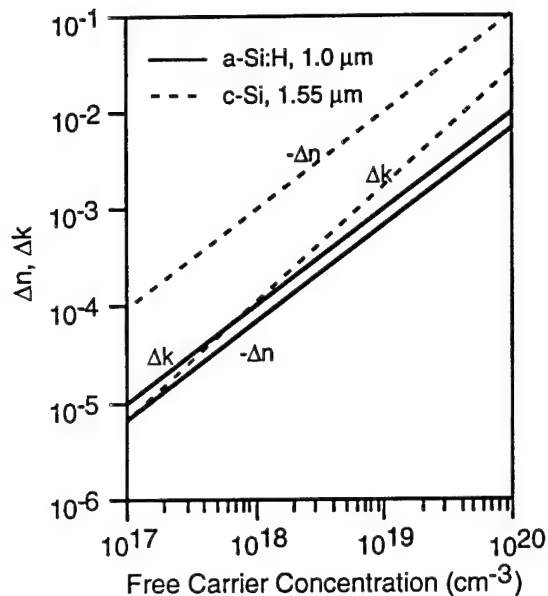


Figure 3. Free carrier absorption effects for bulk a-Si:H[7] and c-Si[5] for free electrons.

below the band gap energy. The simple Drude model predicts a linear increase in absorption coefficient with the density of free carriers, N_e , as

$$\alpha(\omega) = \alpha_o(\omega) + \frac{4\pi N_e q^2 \tau}{cm_e n(\omega)},$$

where q is the elemental charge, τ is the carrier relaxation time, c is the speed of light, m_e is the carrier effective mass, and $n(\omega)$ is the index of refraction. Thus, by injecting high carrier densities we may modify the optical constants of silicon. The change in optical constants, Δn and Δk (complex index $\hat{n} = n + ik$), versus carrier concentration for a-Si:H and c-Si is shown in Figure 3.

In a-Si:H, free carrier absorption effects have been measured using picosecond pump/probe type experiments[6-8]. The problem in a-Si:H is that the carrier decay time is only ~ 1 psec[8] and becomes even shorter for carrier densities in excess of $N_e \approx 10^{21} \text{ cm}^{-3}$. Thus, it is very difficult in a device operating in steady state to inject carrier concentrations greater than around 10^{18} cm^{-3} , though the high density of gap states may enhance below gap absorption by trapping carriers. There have been reports of increased steady state absorption due to filling boron-related defect states in the band gap of doped a-Si:H[9]. For 780 nm illumination, transmission through the a-Si:H film decreased from around 33% at low intensity to 25% at approximately 3 W/cm^2 .

As Figure 3 indicates, free carrier absorption in c-Si is substantially greater than in a-Si:H. In addition, because the carrier lifetime is fairly long -- microseconds to milliseconds for clean silicon -- relatively high carrier densities may be realized in steady state. For a carrier concentration of $N_e \approx 10^{19} \text{ cm}^{-3}$ at $\lambda = 1.55 \mu\text{m}$, $\Delta n \approx 10^{-2}$ and $\Delta \alpha \approx 100 \text{ cm}^{-1}$ [5]. Thus, for infrared modulation, free carrier effects in c-Si are reasonably large.

where $\hat{\chi}^{(3)}$ is the third order nonlinear optical susceptibility and E_x^{dc} is the DC electric field along the x-direction. This is the DC Kerr effect. The change in optical properties due to the Kerr effect are shown in Figure 2 for c-Si and a-Si:H. In c-Si this effect is small and is independent of λ . [5] In a-Si:H, though, the Kerr effect is the dominant electro-optic mechanism, and seems to be resonantly enhanced near the band edge as shown by electroabsorption studies[2, 3]. At a field of $4 \times 10^5 \text{ V/cm}$, we see maximum changes in the optical constants of about $\Delta \alpha = 300 \text{ cm}^{-1}$ ($\Delta \alpha / \alpha \approx 3\%$) at $\lambda = 0.65 \mu\text{m}$ and $\Delta n = 1.2 \times 10^{-3}$ at $\lambda = 0.73 \mu\text{m}$ in a-Si:H.

B. Free Carrier Absorption

The presence of free carriers in a semiconductor causes optical absorption

C. Modulation Effects in Quantum Confined Silicon

As we expected, optical modulation effects in bulk silicon are fairly small. In quantum confined silicon structures, however, we may expect some enhancement in the electro-optic properties of silicon due to sharpening of the absorption edge, confinement of excitons, or quantization of absorption levels.

Some enhancement of the Franz-Keldysh effect may be realized by using quantum confined c-Si structures[10], which would tend to blue-shift and sharpen the band edge absorption. In addition, confinement of excitons in quantum size structures would allow spectral shifting of the excitonic absorption edge with applied field due to the quantum confined Stark effect. Both of these effects are quite large in direct band gap semiconductors but would be weaker in indirect gap silicon. To our knowledge, no one has reported observation of these effects in silicon. Some theoretical studies have indicated a transition to a direct band gap in quantum sized silicon nanostructures[11]; however, the long luminescence lifetimes in nanoscale c-Si (eg., porous silicon) tend to refute this idea[12].

Another electro-optic effect that may be enhanced by quantum confinement is bandfilling. As the effective density of states at the band edge of bulk c-Si is around 10^{21} cm^{-3} , one would need a carrier concentration of 10^{21} cm^{-3} to observe an effective $2kT$ blue shift in the absorption. In silicon quantum dots, though, much lower carrier densities would be required because of quantization of the density of states function.

A major obstacle toward realization of devices based on quantum confinement effects in crystalline silicon is fabrication of uniform nanostructures. Since the energy levels in quantum structures are approximately proportional to $1/L^2$, where L is the size dimension, small nonuniformities in layer thickness or well width quickly wash out sharp absorption features.

To overcome problems associated with fabrication of c-Si quantum structures, some researchers have investigated quantum size effects in amorphous semiconductors. Very uniform multilayer films of amorphous semiconductors have been made using low temperature plasma enhanced chemical vapor deposition. The question is: are there quantum size effects in nanoscale a-Si:H? Though there is some experimental evidence to indicate there are quantum effects[13, 14], the overall enhancement in electro-optic properties is extremely small. This is probably due to the fact that the coherence length of carrier wave functions in amorphous semiconductors is on the order of an interatomic distance. Thus, very few of the carriers have sufficient coherence to resonate inside structures that are tens of atoms across. Figure 4 shows electroabsorption spectra for an a-Si:H/a-Si:C:H "multiple quantum well" structure grown by PECVD process. The structure consists of 50 layers of 3.1 nm thick a-Si:H wells between 13.3 nm thick a-Si:C:H barriers. We measured the Tauc gap of the a-Si:H at 1.72 eV and the gap of the a-Si:C:H at 2.10 eV. Note that the absolute change in transmission is small; we measured $\Delta T/T$ to be about 0.1% maximum for the multilayer at an applied voltage of 10 V over the nominally 1 μm thick film ($E \approx 10^5 \text{ V/cm}$). The stronger electroabsorption signal from the multilayer arises from built-in fields within the silicon well layers.

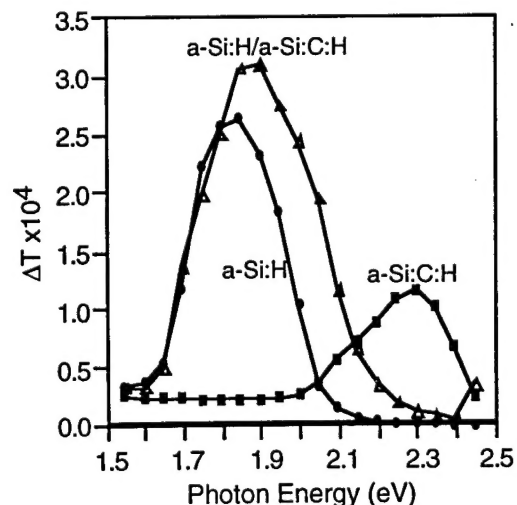


Figure 4. Measured change in transmittance of an a-Si:H/a-Si:C:H multilayer at an applied field of 10^5 V/cm along with equivalent spectra for films of a-Si:H and a-Si:C:H.

Electroabsorption in the multilayer appears to be mainly due to the a-Si:H well layers, though it is slightly blue-shifted from the bulk a-Si:H electroabsorption signal. This blue shift is likely due to spatial confinement of the a-Si:H layers, not quantum confinement[15]. Regardless, we see no evidence for quantum confinement effects in amorphous multilayers -- certainly, no significant enhancements are observed such as quantum confined Franz-Keldysh or Stark effects.

IV. Conclusions

Clearly, the electro-optic effects in bulk a-Si:H and c-Si are small. Device structures require optical and possibly electronic resonance to give useful contrast. Changes in the optical constants of $\Delta n, \Delta k > 10^{-3}$ are required. Electric field effects are not really strong enough for this change. Free carrier effects in c-Si may be useful, though high carrier concentrations of $N > 10^{18} \text{ cm}^{-3}$ are required. Such high carrier concentrations will limit switching speed and sensitivity. Enhancement by quantum confinement does not appear to be possible in a-Si:H, but may be possible to some degree in c-Si. More work is needed to investigate the magnitude of these effects. A major issue in quantum confined material is fabricating very uniform nanostructures so that we may take advantage of the sharper and stronger absorption edge.

References

1. I. Galbraith and B. Ryvkin, J. Appl. Phys. **74**, 4145 (1993).
2. S. Al Jalali and G. Weiser, J. Non-Cryst. Solids **41**, 1 (1980).
3. G. Weiser, U. Dersch, and P. Thomas, Philos. Mag. B **57**, 721 (1988).
4. A. Obeidat, J. Khurgin, and S. Li, in Spatial Light Modulators and Applications **6**, March 15-17, 1993, 1993, Palm Springs, CA, pp. 182.
5. R. A. Soref and B. R. Bennett, IEEE J. Quant. Elec. **QE-32**, 123 (1987).
6. P. M. Fauchet, D. Hulin, A. Migus, A. Antonetti, J. Kolodzey, and S. Wagner, Phys. Rev. Lett. **57**, 2438 (1986).
7. C. Tanguy, D. Hulin, A. Mourchild, P. M. Fauchet, and S. Wagner, Appl. Phys. Lett. **53**, 880 (1988).
8. J. Tauc and Z. Vardeny, Solid State Mat. Sci. **16**, 403 (1990).
9. Y. Maeda, S. Yamamoto, and M. Migitaka, Appl. Phys. Lett. **59**, 390 (1991).
10. D. A. B. Miller, D. S. Chemla, and S. Schmitt-Rink, Phys. Rev. B **33**, 6976 (1986).
11. T. Takagahara and K. Takeda, Phys. Rev. B **46**, 15578 (1992).
12. Y. Kanemitsu, Phys. Rev. B **48**, 12357 (1993).
13. K. Hattori, T. Mori, H. Okamoto, and Y. Hamakawa, in *Amorphous Silicon and Related Materials*, edited by H. Fritzsche (World Scientific, Singapore, 1988), pp. 957
14. M. A. Neifeld, in Spatial Light Modulators and Applications **6**, March 15-17, 1993, 1993, Palm Springs, CA, pp. 44.
15. T. Tiedje, B. Abeles, and B. G. Brooks, Phys. Rev. Lett. **54**, 2545 (1985).

APPENDIX E

FREQUENCY-DEPENDENT AC ETCHING OF POROUS SILICON

On a whim, we tried alternating current (AC) etching to produce porous silicon. To our great surprise, we found a strong frequency dependence to the PL of the resulting porous layers. Figure E.1 illustrates the effect. We etched these samples for 10 min in 25% HF solutions with alternating positive and negative constant currents, which were set at ± 10 mA/cm². The substrates were (111)-oriented, 1-20 Ω cm p-type silicon. Higher etching frequency appears to yield layers with higher PL intensity and emission energy. The current for the 50 Hz sample in Figure E.1 was voltage limited (maximum absolute voltage = ± 105 V) to ~ 3.1 mA/cm², so it is even more peculiar that this sample gave the brightest PL. The dramatic change in PL over fairly low etching frequencies would seem to indicate that the effect is due to ionic processes in the electrolyte and not electronic processes in the silicon; however, one possibility is that holes are injected into the highly resistive porous silicon walls during the cathodic cycle by bonding H⁺ ions to the surface. These holes could then combine with F⁻ ions during the anodic cycle to initiate the removal of silicon atoms. At very low frequencies, etching would essentially take place only at the bottoms of the pores as in DC anodic etching. As the etching frequency gets higher, however, the remaining porous walls also begin to etch due to the AC injection of holes, which results in thinner walls and a more highly porous structure. Assuming that the PL is size

dependent, then the net result is higher emission energy, which we indeed observe.

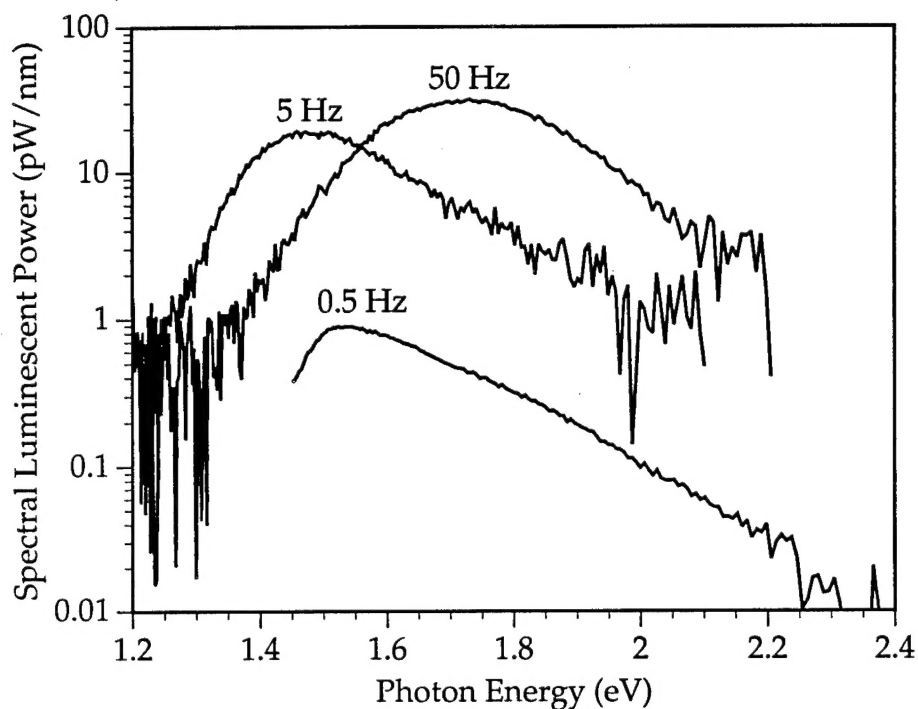


Figure E.1. Photoluminescence of porous silicon layers formed by AC etching in 25% HF solution. The etching currents were set at $\pm 10 \text{ mA/cm}^2$ and alternated at the frequencies shown above each spectrum.